

http://researchcommons.waikato.ac.nz/

Research Commons at the University of Waikato

Copyright Statement:

The digital copy of this thesis is protected by the Copyright Act 1994 (New Zealand).

The thesis may be consulted by you, provided you comply with the provisions of the Act and the following conditions of use:

- Any use you make of these documents or images must be for research or private study purposes only, and you may not make them available to any other person.
- Authors control the copyright of their thesis. You will recognise the author's right to be identified as the author of the thesis, and due acknowledgement will be made to the author where appropriate.
- You will obtain the author's permission before publishing any material from the thesis.

Magnetic Reconnection in Astrophysical Plasmas

A thesis presented to the
University of Waikato
in fulfilment of the thesis requirement
for the degree of

Doctor of Philosophy

by

Stefan Morris Henton



University of Waikato
1996

ABSTRACT

This thesis addresses the problem of understanding magnetic reconnection in astrophysical plasmas. After reviewing earlier work, we present results from the numerical simulation of two periodic reconnection models. Our simulations show that reconnection stalls as the magnetic field at the onset of the current sheet cannot exceed the background magnetic field.

Our numerical results imply that analytical solutions are required for gaining a better understanding of reconnection. First we address the steady-state problem by making a sub-Alfvénic approximation but, unlike previous approaches, we do not linearise the resulting equations. Our solutions show that magnetic field lines can only be annihilated under the sub-Alfvénic approximation – reconnection cannot take place.

Next we derive exact solutions of steady-state reconnection by combining our sub-Alfvénic findings with solutions for the annihilation of anti-parallel magnetic fields. The key point of this approach was to relax the traditional inner symmetries for the magnetic field and plasma flow. Our solutions strongly suggest that steady-state reconnection requires a lack of topological symmetry.

Finally our exact steady-state solutions are extended to include time-dependency. Here the current density at the neutral point attains two maximums and we demonstrate that only one maximum gives a significant energy release. It is also outlined how our exact steady-state and time-dependent solutions can be extended to three dimensions.

ACKNOWLEDGEMENTS

I would like to thank my supervisors – Dr. Ian Craig and Dr. Alfred Sneyd. Their enlightened guidance and continual support during the course of my D.Phil. was greatly appreciated. The assistance given by Dr. Graham Rickard, Dr. Paul Watson, Richard Shepherd and Shane Smith must also be acknowledged. Their suggestions and thoughtful contributions proved to be extremely helpful. I also wish to thank Pam Keall as her efforts played an important role in my secondary school education.

Also I would like to acknowledge the various resources supplied by Department of Mathematics and particularly the computational assistance provided by Craig Lynch-Blosse. Without these essential services, a substantial portion of my thesis would not have been possible. Finally I wish to recognise the financial support provided by the University of Waikato postgraduate scholarship.

CONTENTS

Abstract ii

Acknowledgements iii

Contents iv

Chapter 1 Introduction 1

1.1 Solar Flares 1

1.2 Magnetic Reconnection 1

1.3 Tackling the Reconnection Problem 2

1.4 Outline of Thesis 3

Chapter 2 Mathematical Framework 4

2.1 Introduction 4

2.2 The Mathematical Formulation 4

2.2.1 The MHD Equations 4

2.2.2 Normalisation of MHD Equations 6

2.3 Customary Simplifications 7

2.3.1 The Steady-State Assumption 7

2.3.2 The Incompressibility Assumption 7

2.4 Magnetic Reconnection Mechanisms 8

2.4.1 The Current Sheet Theory 8

2.4.2 Quasi One-Dimensional Reconnection 9

2.4.3 Two-Dimensional Reconnection 13

2.5 Measuring the Energy Release 14

2.6 Computer Simulations 16

Chapter 3 Literature Review 18

3.1 Introduction 18

3.2 Steady-State Models 18

3.2.1 The Sweet-Parker Model 18

3.2.2 The Petschek Model 19
3.2.3 The Forbes & Priest Analysis 20
3.3 Time-Dependent Models 22
3.3.1 The Craig & McClymont Analysis 22
3.3.2 The Craig & Watson Analysis 25
3.3.3 The Biskamp & Welter Simulations 26
3.4 Summary 28

Chapter 4 A Numerical Study 29
4.1 Introduction 29
4.2 Numerical Formulation 29
4.2.1 Governing Equations 29
4.2.2 The Models 30
4.2.3 Our Numerical Approach 33
4.2.4 Reduction of Domain 34
4.3 A Sample Simulation 34
4.4 Results 40
4.4.1 Diagnostics 40
4.4.2 Magnetic Reconnection Rates 46
4.5 Stalling of Reconnection 46
4.5.1 A Sample Simulation 46
4.5.2 The Stalling Mechanism 52
4.6 Summary 57

Chapter 5 Sub-Alfvénic Steady-State Solutions 58
5.1 Introduction 58
5.2 Preliminaries 58
5.2.1 Formulating the Equations 58
5.2.2 The Bracket Notation 60
5.3 Linear Solutions 61
5.3.1 Derivation 61
5.3.2 A Particular Solution 63
5.4 Non-Linear Solutions 67

5.4.1 Derivation 67
5.4.2 A Particular Solution 69
5.5 Discussion 74
5.6 Summary 75

Chapter 6 Exact Steady – State Solutions 76
6.1 Introduction 76
6.2 One-Dimensional Solutions 76
6.2.1 Derivation 76
6.2.2 A Particular Solution 82
6.2.3 Diagnostics 82
6.2.4 Magnetic Reconnection Rates 83
6.3 Two-Dimensional Solutions 84
6.3.1 Derivation 84
6.3.2 Parameter Choices 86
6.3.3 A Particular Solution 87
6.3.4 Interpretation 87
6.3.5 The Separatrices 90
6.3.6 Diagnostics 91
6.3.7 Magnetic Reconnection Rates 91
6.4 Discussion 92
6.5 Extending to Three Dimensions 92
6.6 Summary 94

Chapter 7 Exact Time – Dependent Solutions 96
7.1 Introduction 96
7.2 Governing Equations 96
7.3 The $\beta = 0$ Case 98
7.3.1 Derivation 98
7.3.2 A Particular Solution 99
7.3.3 Discussion 102
7.4 The $|\alpha| = |\beta|$ Case 102
7.4.1 The Outer Solution 102

7.4.2 Diagnostics 103
7.4.3 Magnetic Reconnection Rates 105
7.5 The $|\alpha| \neq |\beta|$ Case 105
7.5.1 The Outer Solution 105
7.5.2 A Numerical Approach 107
7.5.3 Diagnostics 107
7.5.4 Magnetic Reconnection Rates 121
7.6 Discussion 122
7.7 Extending to Three Dimensions 122
7.8 Summary 124

Chapter 8 Conclusions 125
8.1 Opening Remarks 125
8.2 Discussion of Presented Work 125
8.3 Suggestions for Further Work 128

References 130

CHAPTER 1

Introduction

1.1 Solar Flares

A solar flare is a tremendous release of stored energy from within the solar atmosphere. The energy liberated is of order 10^{25} Joules with a duration time of approximately 10^2 seconds – see reviews by Parker (1979), Priest (1981). Dramatic increases in radiation emissions across the electromagnetic spectrum occur and plasma discharges are readily observed.

Early investigations into solar flares were restricted to crude and infrequent observations taken from primitive, Earth-bound apparatus. However recent advances in technology have enabled more highly resolved examinations of the solar atmosphere to be conducted (Zirin 1966, Svestka 1976, Priest 1981). It is now recognised that flares originate within the outermost layers of the solar atmosphere, namely the corona, and result in changes in the plasma density and temperature.

Solar flares can nowadays be monitored with satellite-borne instrumentation (Sturrock 1980, Culhane & Jordan 1991). By avoiding interference from the Earth's atmosphere, more elaborate observations of flare phenomena are possible. For example, highly resolved images of X-ray or γ-ray emissions can be made over entire flare durations. Recent satellite data indicates that variations in plasma temperature are intrinsically linked to solar flare dynamics.

1.2 Magnetic Reconnection

Physical observations suggest that solar flares simplify the magnetic field in the corona. This simplifying tendency implies that 'magnetic reconnection' must play an important role in the flare mechanism. Magnetic reconnection is loosely defined as the 'breaking then rejoining' of topologically-dissimilar field lines across a null in the magnetic field.

Two fundamental reasons behind the reconnection hypothesis are (*i*) only reconnection can change the topology of a magnetic field and (*ii*) the corona contains a very strong magnetic field. Order of magnitude calculations (Priest 1981) show that the magnetic energy in the coronal field is sufficient to produce a solar flare. Hence magnetic reconnection is the leading contender for a solar flare mechanism.

The study of magnetic reconnection has applications to other areas of scientific research. It is believed, for instance, to occur in the interaction between the solar wind and Earth's magnetosphere. This encounter also releases energy which appears attributable to magnetic reconnection.

The corona consists of a magnetic field within a compressible plasma so a magnetohydrodynamical (MHD) approximation is commonly adopted. Hence the over-riding aim is to derive solutions from the classical MHD equations. Analytical (or numerical) solutions would then illustrate how magnetic reconnection takes place and the conditions conducive to solar flares. However it should be appreciated that the extreme nature of solar flares might violate an MHD approximation. High temperatures and the presence of small length-scales may lead to non-classical effects playing an essential role in the energy release.

An important parameter in the study of solar flares is the plasma resistivity η. Reconnection is not possible with zero resistivity! From theoretical calculations of η (Spitzer 1962) one can estimate the magnetic Reynolds number R_m for coronal plasmas. We have that

$$R_m = \frac{L_o v_o}{\eta},$$

where L_o and v_o denote a characteristic length-scale and plasma velocity respectively. For the typical values $L_o = O(10^7)$ m, $v_o = O(10^4)$ m/s and $\eta = O(10^{-1})$ m^2/s, we estimate that R_m is $O(10^{12})$ in the corona.

This enormous value of R_m implies that, to liberate vast quantities of energy in small time period, one requires a localised distribution of current – traditionally referred to as a 'current sheet'. Only a current distribution of this nature could reduce R_m to a level that might explain a solar flare.

1.3 Tackling the Reconnection Problem

The MHD equations are coupled, non-linear and three-dimensional so only simplified cases can be treated analytically. However it must be appreciated that the understanding of reconnection is more likely with simplified models. Typical assumptions that are often adopted include (*i*) assuming an incompressible plasma, (*ii*) assigning a high degree of symmetry to the magnetic field and plasma flow, and (*iii*) assuming an ignorable third co-ordinate.

Magnetic reconnection can be addressed from either a time-dependent or steady-state point of view. Adopting a steady-state approximation simplifies the MHD equations substantially thereby allowing a more analytically-based treatment. Hence this approximation promotes a greater understanding of the reconnection mechanism. Here we mention that a steady-state

idealisation provided the first steps toward constructing a solar flare model (Sweet 1958, Parker 1957, 1963).

The 'number-crunching' capabilities of modern computers have made time-dependent simulations of magnetic reconnection possible. With suitable initial conditions and boundary conditions, a reconnection process can now be simulated on computer – some examples are Biskamp & Welter (1980) and DeLuca & Craig (1992). However, although valuable insight can be gained with numerical simulations, it must be stressed that *major* drawbacks do arise.

The mathematical models found in the scientific literature only provide us with a limited understanding of reconnection. Analytical approaches require important terms in the MHD equations to be discarded or questionable assumptions to be made. Meanwhile numerical approaches are severely restricted by resolution constraints and uncertainties over determining suitable boundary conditions arise. One must therefore conclude that the reconnection problem is *far* from being solved.

1.4 Outline of Thesis

This thesis addresses the problem of developing an improved reconnection model and the layout of the material is as follows. In Chapter 2 we present the mathematical framework for approaching the reconnection problem. Here we introduce the governing MHD equations then outline various strategies for constructing solutions. Chapter 3 reviews the traditional models of magnetic reconnection. Only with an understanding of earlier work can an improved model of magnetic reconnection be established. These two chapters provide the necessary foundations for the following chapters.

In Chapters 4, 5, 6 and 7 we present our original work. The aim here is to advance the current understanding of magnetic reconnection. Two numerical models of a time-dependent reconnection are studied in Chapter 4. Both models consist of a compressible MHD plasma in a fully periodic geometry. Next Chapters 5 and 6 investigate the steady-state problem. Now the plasma is assumed to be incompressible and the governing equations are treated analytically. The more complicated issue of time-dependent reconnection is then revisited in Chapter 7. This work extends our steady-state findings in Chapter 6 to incorporate time-dependency.

The conclusions of our research are contained in Chapter 8. Here we summarise the findings of Chapters 4 to 7 then indicate how our reconnection solutions compare with the traditional models reviewed in Chapter 3. Our discussion then focuses on how, based on our results, magnetic reconnection relates to solar flare observations. Finally we provide suggestions for further work.

CHAPTER 2

Mathematical Framework

2.1 Introduction

This chapter lays out the mathematical framework for tackling the magnetic reconnection problem. Here the notion of reconnection is put into a mathematical context and typical simplifications are discussed. We also outline the typical approaches to solving the reconnection problem. The main objective of this chapter is to provide a clear starting point for the following chapters.

In Section 2.2 we introduce the equations of a resistive MHD plasma. and customary simplifications are detailed in Section 2.3. We discuss the notion of current sheets then outline one-dimensional and two-dimensional views of reconnection in Section 2.4. Next we introduce two diagnostics that measure the energy release in Section 2.5. Finally Section 2.6 reviews the computational approach to the reconnection problem.

2.2 The Mathematical Formulation

2.2.1 The MHD Equations

The motion of an inviscid plasma is described by

$$\rho(\frac{\partial \mathbf{v}}{\partial t} + \mathbf{v}.\nabla\mathbf{v}) = \mathbf{J} \times \mathbf{B} - \nabla p, \tag{2.1}$$

where

$$\mathbf{J} = \frac{1}{\mu_0}\nabla \times \mathbf{B}, \tag{2.2}$$

and μ_0 is the permeability of free space. The dependent variable $\mathbf{B}(\mathbf{r}, t)$ represents the magnetic field while $\rho(\mathbf{r}, t)$ and $\mathbf{v}(\mathbf{r}, t)$ denote the plasma density and velocity respectively. Plasma pressure is given by the scalar function $p(\mathbf{r}, t)$ and $\mathbf{J}(\mathbf{r}, t)$ is the current density.

Equation (2.1) is not fully specified unless a functional relationship for p is established. On physical grounds, one would expect the plasma pressure in the corona to be directly related to variations in plasma density and temperature. However, to avoid the further complication

of introducing a heat equation, it shall be assumed that astrophysical plasmas obey some gas law. We therefore adopt the polytropic gas relationship

$$p = k\rho^{\gamma},$$

where k and γ are externally prescribed constants. The multiplier k simply determines the magnitude of the plasma pressure force while the exponent γ lies in the range $1 \leq \gamma \leq \frac{5}{3}$. It is understood that temperature dependencies are accounted for implicitly within the polytropic approximation.

Throughout this thesis we shall neglect viscous forces. We take the view that complications arising from retaining viscosity hampers the mathematical analysis and therefore unduly complicate the magnetic reconnection problem. The key point here is that, since reconnection depends upon plasma resistivity, the inclusion of viscous forces seems physically unnecessary.

The magnetic field is determined by

$$\mathbf{E} + \frac{1}{c}\mathbf{v} \times \mathbf{B} = \frac{1}{\sigma}\mathbf{J}, \tag{2.3}$$

where $\mathbf{E}(\mathbf{r}, t)$ is the electric field while c and σ denote the speed of light and electrical conductivity respectively.

Taking the curl of (2.3) gives

$$\frac{\partial \mathbf{B}}{\partial t} = \nabla \times (\mathbf{v} \times \mathbf{B}) + \eta \nabla^2 \mathbf{B}, \tag{2.4}$$

since

$$\nabla \times \mathbf{E} = -\frac{1}{c}\frac{\partial \mathbf{B}}{\partial t},$$

and $\eta = c/(\mu_0 \sigma)$ is called the plasma resistivity.

The magnetic field must also satisfy

$$\nabla . \mathbf{B} = 0. \tag{2.5}$$

A consequence of this equation is that *no* monopoles can exist in the magnetic field.

From mass conservation it follows that

$$\frac{\partial \rho}{\partial t} + \nabla . (\rho \mathbf{v}) = 0. \tag{2.6}$$

We will outline how incompressibility affects this equation in the next section.

Equations (2.1) to (2.6) determine the evolution of an MHD system. One immediately recognises that these governing equations are non-linear, coupled and three-dimensional. This level of complexity already indicates that establishing solutions will be a very demanding assignment.

2.2.2 Normalisation of MHD Equations

We now proceed to non-dimensionalise the MHD equations by defining characteristic values (denoted by a c subscript) for each variable. Here we introduce

$$\rho = \rho_c \rho',$$

$$\mathbf{v} = v_c \mathbf{v}',$$

$$\mathbf{B} = B_c \mathbf{B}',$$

$$L = L_c L',$$

$$t = t_c t',$$

and define

$$t_c = t_A = \frac{L_c}{v_c},$$

$$v_c = v_A = \frac{B_c}{\sqrt{\mu_0 \rho_c}}.$$

The Alfvén time t_A and Alfvén speed v_A simply rescale our units for measuring time and velocity respectively. Typical values are $B_c = O(10^{-2})$ T, $\rho_c = O(10^{-9})$ kg/m^3 and $L_c = O(10^7)$ m so we have that $v_A = O(10^6)$ m/s and $t_A = O(10)$ s.

Substitution of the new variables and dropping the dashes gives

$$\rho\left(\frac{\partial \mathbf{v}}{\partial t} + \mathbf{v}.\nabla\mathbf{v}\right) = (\nabla \times \mathbf{B}) \times \mathbf{B} - \beta \nabla \rho^\gamma, \tag{2.7}$$

$$\frac{\partial \mathbf{B}}{\partial t} = \nabla \times (\mathbf{v} \times \mathbf{B}) + \bar{\eta} \nabla^2 \mathbf{B}, \tag{2.8}$$

$$\frac{\partial \rho}{\partial t} + \nabla.(\rho \mathbf{v}) = 0, \tag{2.9}$$

$$\nabla.\mathbf{B} = 0, \tag{2.10}$$

and

$$\mathbf{E} + \mathbf{v} \times \mathbf{B} = \bar{\eta} \mathbf{J}. \tag{2.11}$$

Here we have defined

$$\bar{\eta} = \frac{1}{R_m} = \frac{\eta}{L_c v_c}, \qquad \beta = \frac{k \rho_c^\gamma}{(B_c^2/\mu_0)},$$

where R_m is the magnetic Reynolds number.

Equations (2.7) to (2.11) are specified by the two parameters β and $\bar{\eta}$. It is recognised that β represents half the ratio of plasma pressure to magnetic pressure in our characteristic units. A coronal plasma is regarded as a low-β plasma (Craig & Watson 1992) where a

typical value is $\beta = O(10^{-2})$. Meanwhile $\bar{\eta}$ denotes the inverse magnetic Reynolds number and $\bar{\eta} = O(10^{-12})$. For the remainder of this thesis, we shall discard the superfluous bar notation on $\bar{\eta}$.

We point out that, for sufficiently large values of β, an MHD plasma must tend towards the incompressible limit. On the other hand, specifying $\beta = 0$ will correspond to a pressureless plasma. Although a pressureless plasma is physically unrealistic, specifying $\beta = 0$ simplifies (2.7) considerably and analytical process can be gained (see Hassam 1992, Craig & McClymont 1991, 1993). The work presented in this thesis, however, concentrates on $\beta \neq 0$.

2.3 Customary Simplifications

2.3.1 The Steady-State Assumption

A typical method for attacking the magnetic reconnection problem is specialising to steady-state (Sweet 1958, Parker 1957, 1963). The primary advantages of this approach are

(*i*) the MHD equations are simplified dramatically,

(*ii*) concerns about determining time-dependent boundary conditions are alleviated,

(*iii*) steady-state reconnection is easier to interpret.

In steady-state the reconnection of magnetic field lines must continue indefinitely. Thus, to maintain this on-going process, magnetic flux and plasma must be continuously injected and extracted from the MHD system. This requirement indicates that steady-state reconnection must be 'fuelled' perpetually by some external means. Hence steady-state reconnection is regarded as a dynamical process 'driven' by the outer boundary conditions.

Obvious questions now are – how does steady-state reconnection relate to time-dependent reconnection? A solar flare is a dynamical event so can steady-state results be extended to time-dependent situations? Although these questions have yet to be answered, our underlying goal is to *understand* reconnection so a steady-state approach seems the logical first step. Furthermore possible tactics for establishing time-dependent models should be highlighted by steady-state models.

2.3.2 The Incompressibility Assumption

Another simplification that is often adopted is to specialise to an incompressible plasma. Virtually all analytically-based work on steady-state reconnection assume the incompressible limit *i.e.* $\rho =$ constant. One noteworthy example is the Sweet-Parker model (Sweet 1958, Parker 1957, 1963) which is discussed in the following section.

Three important simplifications result from the incompressibility assumption. These are

(i) the term $\rho\mathbf{v}.\nabla\mathbf{v}$ can be greatly simplified,

(ii) equation (2.9) reduces to

$$\nabla.\mathbf{v} = \mathbf{0}, \tag{2.12}$$

which allows the introduction of a stream function. Points (i) and (ii) will be clearly illustrated in later chapters.

(iii) ρ =constant so the pressure force p can only be induced via 'external' quantities such as temperature. Thus p becomes an independent variable of the MHD equations so a functional relationship is no longer required.

A coronal plasma must exhibit some degree of compressibility. This property implies that incompressible findings are to be considered from a 'limiting-case' standpoint. Thus we identify solutions derived for an incompressible plasma to be approximations of solutions for a slightly incompressible plasma. In any case, one expects that the key features of the magnetic reconnection should extend to the incompressible case. This claim is supported by Chapter 4 where results from compressible simulations are consistent with previous incompressible simulations (DeLuca & Craig 1992) of the same model.

Furthermore incompressibility is an assumption that 'acts against' the reconnective mechanism. Here the plasma is allowed the maximum possible feedback on the reconnection rate. Thus demonstrating a fast energy release for an incompressible plasma could be regarded as the worst-case scenario. More discussion on the role of compressibility in magnetic reconnection can be found in Craig & McClymont (1993).

In this thesis we investigate both compressible and incompressible magnetic reconnection. Our numerical investigation in Chapter 4 simulates a compressible plasma under the polytropic approximation discussed earlier. Meanwhile an incompressible assumption is required for our analytically-based approach in Chapters 5, 6 and 7.

2.4 Magnetic Reconnection Mechanisms

2.4.1 The Current Sheet Theory

A leading question in the study of solar flares is – can reconnection release enormous amounts of energy ($O(10^{25})$ Joules) in a short time interval ($O(10^2)$ seconds)? A brief order-of-magnitude analysis indicates that an explosive energy liberation from the corona will not occur unless the conditions discussed below are met.

We demonstrated in Chapter 1 that a typical value of η is $O(10^{-12})$. This suggests that (2.8) can be approximated by

$$\frac{\partial \mathbf{B}}{\partial t} = \nabla \times (\mathbf{v} \times \mathbf{B}),$$

which implies that the magnetic field is 'frozen-in'. This means that a given plasma particle will always lie upon the same field line. However, as reconnection decouples the magnetic field from the plasma flow, the frozen-in condition cannot hold universally.

Retaining η allows an energy dissipation time τ to be estimated from (2.8). We have

$$\tau \sim \frac{l^2}{\eta},$$

where l is some characteristic length-scale for the magnetic field. A coronal value of η implies that 'global' ($l = O(1)$) energy releases take an incredibly long time ($\tau = O(10^{12})$). It is obvious that this value of τ needs to be reduced dramatically.

These two conditions can only be satisfied with a highly localised current distribution – a current sheet. Here the pivotal feature is the possible reduction in the length-scale as l need not reflect the global dimensions of the corona. Instead a far smaller value determined by the current sheet width becomes appropriate. As an example, if $l^2 = 10\eta$ then $\tau = O(10)$ which roughly matches solar flare observations.

Large currents would allow the resistive term $\eta\nabla^2\mathbf{B}$ to become comparable to the other terms in (2.8). Thus the frozen-in constraint would no longer apply and the magnetic field lines could 'slip' though the plasma. Now the reconnection of field lines can take place.

2.4.2 Quasi One-Dimensional Reconnection

The earliest models of magnetic reconnection (Sweet 1958, Parker 1957, 1963) arose from the hypothetical situation illustrated by Figure 2.1. Here magnetic fields lines (solid lines) that are approximately anti-parallel are driven together by a converging plasma flow (dotted lines). Upon reaching the neutral line, the opposing field lines are annihilated by plasma resistivity and a current sheet (shaded region) develops. Hence it has been postulated that the schematic configuration shown in Figure 2.1 may explain a solar flare.

One immediately appreciates from Figure 2.1 that the reconnection system has two extreme regions. First a current-free outer region where the role of η is negligible and the frozen-in condition applies. Second a current sheet region where plasma flows are comparatively small and η becomes important. A salient question is – how do these two contrasting regions 'fit together'?

A typical method of investigation, see Figure 2.2, is to compare the magnetic field and plasma flow entering the current sheet (u, v, B_{sheet}) and along the inflow boundary (u_0, B_0). Here we use the 0 subscript to denote values corresponding to the outer boundary. Two further measures of principal interest are the width l and length L of the current sheet. How

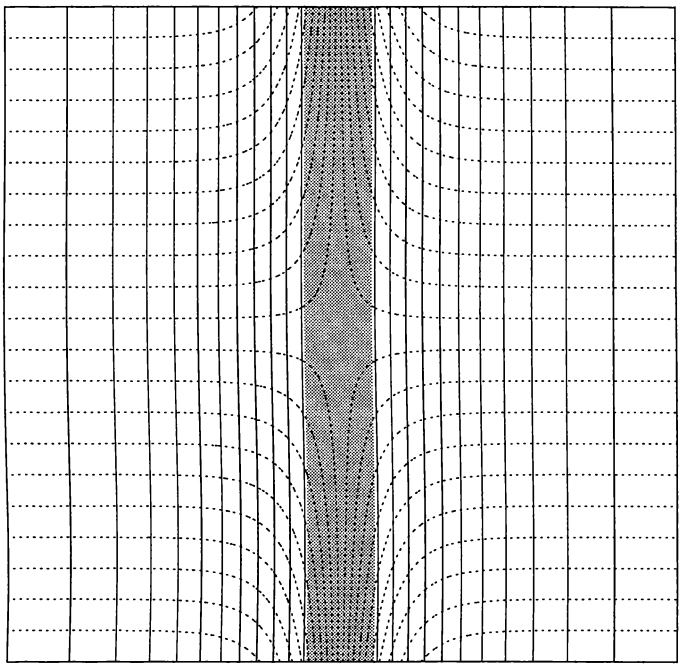


Figure 2.1. Schematic of quasi one-dimensional reconnection where solid lines are magnetic field lines and dotted lines are streamlines.

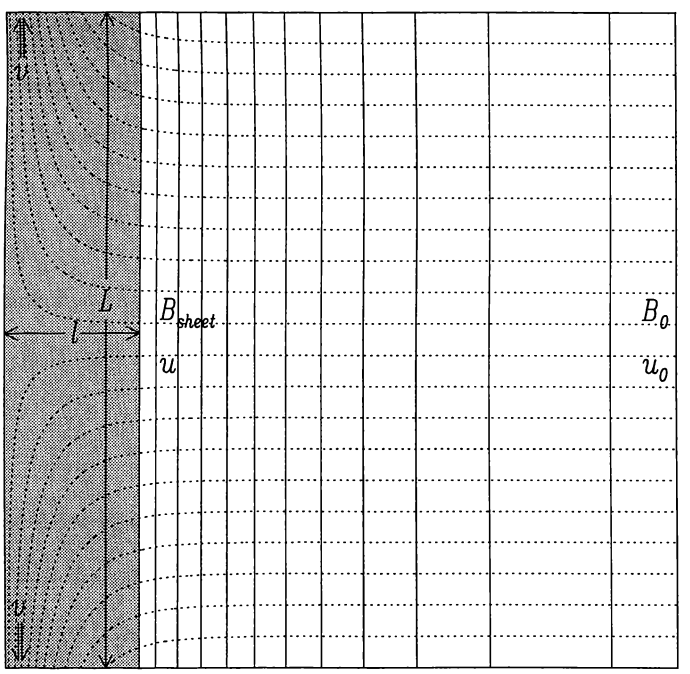


Figure 2.2. Commonly adopted diagnostics - l and L are the width and length of the current sheet, $B_{\mathbf{sheet}}$ and B_0 are the magnetic field entering the sheet and outer boundary, u, v and u_0 the plasma speeds at the sheet and outer boundary.

$u, u_0, v, B_{\text{sheet}}, B_0, l, L$ are related to each other and, in particular, η would provide valuable understanding of the reconnective mechanism.

The Sweet-Parker model of quasi one-dimensional magnetic reconnection is now discussed. Their qualitative analysis is recognised as providing the first steps toward developing a flare model.

The Sweet-Parker model considers an incompressible MHD plasma in steady-state. The appropriate equations from Section 2.2 are

$$\mathbf{E} + \mathbf{v} \times \mathbf{B} = \eta \mathbf{J}, \tag{2.13}$$

$$\mathbf{v}.\nabla\mathbf{v} = \mathbf{J} \times \mathbf{B} - \nabla p, \tag{2.14}$$

$$\nabla.\mathbf{B} = 0, \tag{2.15}$$

$$\nabla.\mathbf{v} = 0, \tag{2.16}$$

where $\rho = 1$ for simplicity.

The flow of plasma into the current sheet can be determined by (2.13). An order-of-magnitude gives

$$u \approx \frac{\eta}{l},$$

where u is the plasma speed into the current sheet and l is the sheet width – see Figure 2.2.

The plasma is incompressible so a mass-conservation law can be applied to the current sheet. Therefore it follows from (2.16) that

$$uL \approx vl,$$

where v is the plasma speed out of the current sheet.

The sheet length L simply depends upon the dimensions of modelled region. Hence

$$L = L_0,$$

where L_0 denotes a global length-scale.

The plasma flow will become small on approaching the neutral line. This implies that $\mathbf{v}.\nabla\mathbf{v}$ can be neglected so the inflow component of (2.14) becomes

$$\frac{\partial p}{\partial x} \approx -\frac{1}{2}\frac{\partial (B_{\text{sheet}})^2}{\partial x},$$

with B_{sheet} denotes the magnetic field at the onset of the current sheet. Integration yields

$$p - p_0 \approx -\frac{1}{2}(B_{\text{sheet}})^2,$$

where p_0 denotes the background plasma pressure.

Now the outflow component of (2.14) is investigated. As $\mathbf{J} \times \mathbf{B}$ vanishes in this direction, one has

$$\frac{\partial p}{\partial y} \approx -\frac{1}{2}\frac{\partial v^2}{\partial y},$$

and integrating gives

$$p - p_0 \approx -\frac{1}{2}v^2,$$

where p_0 is defined above.

Equating the two expressions for p gives

$$v \approx v_a = B_{\text{sheet}},$$

where v_a defines the local Alfvén speed.

The Sweet-Parker model now makes the identification that

$$B_{\text{sheet}} \approx B_0,$$

which subsequently yields

$$l \approx \sqrt{\frac{\eta L_0}{B_0}},$$

$$u \approx \sqrt{\frac{B_0 \eta}{L_0}},$$

and

$$J_0 \approx \frac{B_{\text{sheet}}}{l} \approx \sqrt{\frac{B_0^3}{\eta L_0}},$$

where J_0 signifies the current value at the neutral point.

The simplest interpretation of magnetic reconnection suggests that B_0 and L_0 are global quantities which are independent of plasma resistivity. Thus the Sweet-Parker model gives

$$u = O(\eta^{1/2}).$$

As η is extremely small, this scaling means that field lines on either side of the neutral line annihilate very slowly. Hence the Sweet-Parker model cannot release energy rapidly enough for a solar flare.

An obvious problem with the Sweet-Parker approach is the disjointed treatment of the current sheet and outer solution. The current sheet is treated separately and then simply 'patched' onto an outer solution – the all-important transition is virtually ignored. Previous studies (*e.g.* Biskamp & Welter 1980) clearly illustrate that the current sheet is highly sensitive to outer boundary conditions. This highlights the *global* nature of the reconnection

problem. Thus, to gain a better understanding of reconnection, a global treatment of the MHD equations will be required.

A second cause for concern with the Sweet-Parker analysis is assuming B_{sheet} to be invariant of η. Approximating B_{sheet} with B_0 seems questionable as many studies indicate that the magnetic field entering the sheet is strongly dependent on η. An increase in B_{sheet} caused by a reduction of η is often observed (*e.g.* Biskamp & Welter 1980).

We emphasise that the fundamental problem with a strictly one-dimensional model is the degenerate nature of the magnetic field. In this case only resistive annihilation of the magnetic field lines takes place – *not* reconnection. Observations show that topological simplifications of the magnetic field are an intrinsic outcome of a solar flare. This fact naturally implies that a realistic model requires, at least, a two-dimensional magnetic field.

2.4.3 Two-Dimensional Reconnection

The two-dimensional picture of magnetic reconnection, see Figure 2.3, says that a converging plasma flow (dotted lines) carries osculating field lines (solid lines) toward each other (Dungey 1953). Once opposing pairs of field lines reach the neutral point, they reconnect via plasma resistivity, then diffuse into the alternate X-type quadrants. Field lines that have undergone reconnection are carried away by the outgoing plasma flow. A current sheet (shaded region) of a somewhat singular nature is expected to straddle the neutral point.

The neutral line of quasi one-dimensional reconnection (see Figure 2.1) no longer exists. Instead a pair of magnetic field lines that intersect each other at the neutral point appear. These curves are known as the separatrices of the magnetic field. In then follows that a necessary requirement of reconnection is that plasma must flow across the separatrices.

The current view of magnetic reconnection in two dimensions implies

$$u, B_y = \text{antisymmetric},\ v = \text{symmetric} \qquad \text{across } x = 0,$$

$$v, B_x = \text{antisymmetric},\ u = \text{symmetric} \qquad \text{across } y = 0,$$

where

$$\mathbf{B} = (B_x, B_y), \qquad \mathbf{v} = (u, v).$$

We refer to these inner conditions as the 'traditional symmetries'. Specifying the traditional symmetries makes the origin a neutral point of the magnetic field and stagnation point of the plasma flow.

A major advantage of adopting the traditional symmetries is mathematical simplicity. Now only one quadrant of the MHD system need be considered and so analytical and computational

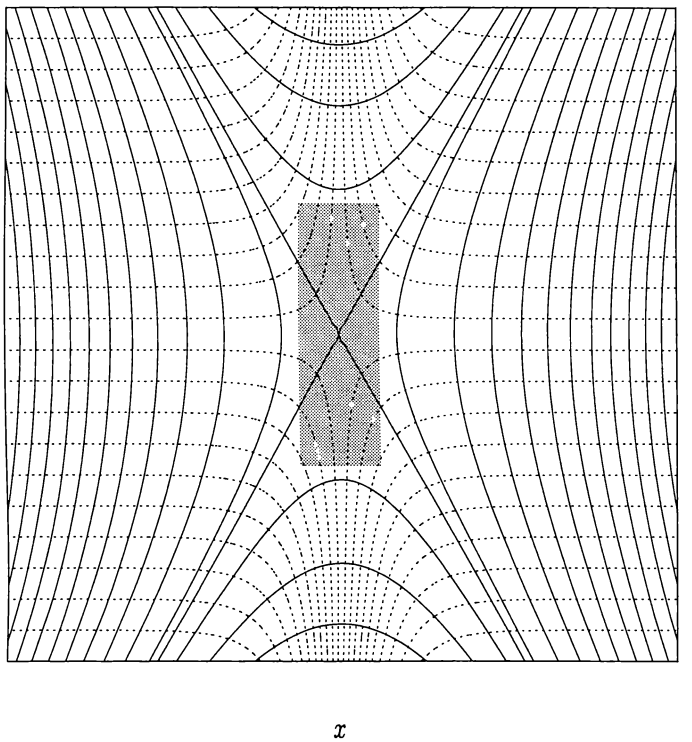


Figure 2.3. Schematic of two-dimensional reconnection where solid lines are magnetic field lines and dotted lines are streamlines.

simplifications can be made. Furthermore the interpretation of reconnection should be easier. These predefined symmetries in the magnetic field and plasma flow would seem to give the simplest geometry for two-dimensional reconnection.

It is unclear, however, whether adopting the traditional symmetries is not overly restrictive in some manner. Magnetic reconnection may depend upon a certain lack of symmetry in the magnetic field and plasma flow. Here we remark that the steady-state solutions presented in Chapters 6 and 7 do not adopt the traditional symmetries. These chapters will show that *considerable* progress can be accomplished by simply relaxing this four-fold symmetry.

2.5 Measuring the Energy Release

Two diagnostics that quantify the rate of energy release from magnetic reconnection are now discussed (see Biskamp & Welter 1980, Biskamp 1986). The first diagnostic we employ is the rate of flux annihilation at the neutral point. For two-dimensional reconnection this can be expressed as

$$\frac{\partial \psi}{\partial t} = \eta J_0, \tag{2.17}$$

with

$$\mathbf{B} = \nabla \times \psi \hat{\mathbf{z}},$$

where $\psi(x,y)$ is a flux function and J_0 is the current value at the neutral point. This diagnostic gives the rate at which magnetic field lines are being reconnected at the neutral point.

Our second measure of the magnetic reconnection rate is the Ohmic dissipation rate

$$W_\eta = \eta \int_V J^2 \mathrm{d}V,$$

where J is current and V denotes volume. The Ohmic dissipation rate describes the conversion of magnetic energy into heat via current. Further details about this diagnostic measure can be found in Cowling (1957).

Since this thesis concentrates on two-dimensional reconnection, we choose to adopt a planar version of the Ohmic dissipation. Namely

$$W_\eta = \eta \int_S J^2 \mathrm{d}S, \tag{2.18}$$

where S signifies surface.

In general we shall require numerical integration techniques to evaluate W_η accurately. However, as current distributions will be highly localised, one can use the approximation

$$W_\eta \approx \eta J_0^2 L l,$$

where l and L are the current sheet width and length respectively and J_0 is defined in (2.17). We mention that previous studies show that this estimation is quite sufficient to establish reliable scalings (Biskamp & Welter 1980, DeLuca & Craig 1992).

We now must determine conditions under which a given model can account for energy releases from solar flares. As η is $O(10^{-12})$, one immediately realises that reconnection rates cannot depend upon a positive power. Hence a plausible flare mechanism must have rates that are either invariant or depend inversely on η.

A given reconnection measure that does not scale as a positive power of η is classed as 'fast'. Similarly an 'ultra-fast' measure is defined as being inversely dependent on η. Thus a realistic flare model must have at least one 'fast' or 'ultra-fast' reconnection rate. Our goal in the following chapters, therefore, is to construct 'fast' solutions from the MHD equations.

We now briefly return to the Sweet-Parker model of magnetic reconnection. The rate of flux annihilation along the neutral line is

$$\frac{\partial \psi}{\partial t} = \eta J_0 \sim \eta^{1/2},$$

while the Ohmic dissipation rate becomes

$$W_\eta \approx \eta J_0^2 L l \sim \eta^{1/2}.$$

Both our adopted diagnostics confirm that the Sweet-Parker mechanism produces 'slow' rates of energy release. Obviously this reconnection model does not provide a satisfactory explanation of solar flares.

2.6 Computer Simulations

The number-crunching capability of modern computers allow the complicated issue of time-dependent reconnection to be addressed. By making a suitable choice of initial conditions and boundary conditions, the reconnection process can be readily simulated (*e.g.* Biskamp & Welter 1980, Strauss 1990). The diagnostics given in Figure 2.2 can be calculated and the energy release can be monitored.

A typical simulation consists of a perturbed MHD equilibrium that requires magnetic reconnection to regain an equilibrium. The magnetic disturbance mutates into a current sheet focused around the neutral point. This accumulation of current then initiates an energy release via reconnection and the perturbed system reaches an equilibrium state.

The difference between analytical and computational results must be appreciated. Any analytical solution is universally valid – it holds in all cases. On the other hand, a given simulation is 'case-wise' valid – it only holds for the prescribed initial conditions and parameter values. Hence analytical solutions would give, in general, a deeper understanding of the reconnection mechanism than a collection of numerical simulations.

A persistent nightmare with computational approaches has been the need to establish realistic boundary conditions (Forbes & Priest 1987). This problem has been an issue of great contention in the literature and a universally accepted technique has not appeared. Claims of successfully implemented boundaries (Biskamp 1986) have emerged which seemingly require awkward and cumbersome iterations. However it must be noted that several authors (Forbes & Priest 1987) strongly dispute the validity of such techniques. Here we simply take the view that specifying boundary conditions is an unsolved problem needing further investigation.

Previous numerical studies of time-dependent reconnection indicate that closed-flow boundaries cause problems (DeLuca & Craig 1992). Here plasma is 'imprisoned' within the modelled region. Substantial build-ups of mass inevitably arise which thereby induce strong pressures gradients that obstruct the circulation of plasma. Thus reconnection becomes extremely slow. A possible 'cure' for this problem is to adopt open-flow boundaries. Open boundaries

would allow plasma to pass through the reconnection model and mass accumulations can be alleviated.

Numerical approaches are further thwarted as code run-times place an upper bound on the resolution. The highly localised nature of the current sheet therefore restricts η values that can be simulated with adequate resolution. Previous studies, to the best of our knowledge, have only reached $\eta \approx 1 \times 10^{-4}$ (Biskamp & Welter 1980, DeLuca & Craig 1992, Strauss 1990) before resolution problems set in. Obviously this value is *several* orders of magnitude greater than coronal values of $\eta = O(10^{-12})$.

The key message here is that a 'number-crunching' approach will not solve the magnetic reconnection problem. On the other hand, analytical approaches are thwarted by the high complexity of the governing MHD equations. Clearly a marriage of both analytical and numerical techniques is required.

CHAPTER 3

Literature Review

3.1 Introduction

This chapter surveys a selection of reconnection models that appear in the literature. Our motivation is to develop an understanding of the solar flare problem by discussing the strengths and weaknesses of earlier work. Moreover diagnostics are evaluated to determine whether a proposed model can explain a solar flare. Deducing the limitations of previous analysis will greatly assist our construction of improved reconnection models.

It must be stressed that our literature review should not be regarded as a complete synopsis of previous work. Here we present models that are directly applicable to our investigation. Detailed reviews of magnetic reconnection have already appeared and we mention the extensive reviews by Vasyliunas (1975), Priest (1981) and Biskamp (1994). The reader is encouraged to consult these publications for a further discussion of the solar flare problem.

Steady-state models of reconnection are presented in Section 3.2. We first outline the models by Sweet-Parker and Petschek then discuss the linear analysis of Priest & Forbes. Next we present time-dependent models of reconnection in Section 3.3. The pressureless analysis of Craig & McClymont and Craig & Watson is reviewed followed by the numerical study of Biskamp & Welter. A brief summary of our literature review is given in Section 3.4.

3.2 Steady-State Models

3.2.1 The Sweet-Parker Model

We briefly return to the pioneering work of Sweet and Parker (Sweet 1958, Parker 1957, 1963) detailed in Chapter 2. Here we shall simply re-state the Sweet-Parker (now abbreviated to SP) scalings established earlier.

The SP model consists of two anti-parallel magnetic fields driven together by a converging plasma flow – see Figure 2.1. On reaching the neutral line, opposing field lines are annihilated and a current sheet is generated along the neutral line.

The scalings for the SP model are

$$l \sim \eta^{1/2}, \qquad L \sim \eta^{0},$$

$$u \sim \eta^{1/2}, \qquad v \sim \eta^{0},$$

$$B_{\text{sheet}} \sim \eta^{0}, \qquad J_0 \sim \eta^{-1/2},$$

where l and L are the current sheet width and length, u and v are the speed of plasma entering and exiting the sheet, B_{sheet} is the magnetic field at the onset of the sheet and J_0 is the current along the neutral line.

The flux annihilation rate dependency is

$$\frac{\partial \psi}{\partial t} = \eta J_0 \sim \eta^{1/2},$$

where

$$\mathbf{B} = \nabla \times \psi \hat{\mathbf{z}}.$$

Meanwhile the Ohmic dissipation rate scales as

$$W_\eta \approx \eta J_0^2 l L \sim \eta^{1/2}.$$

Both measures are slow so the SP model of magnetic reconnection cannot explain of a solar flare.

3.2.2 The Petschek Model

The two-dimensional model proposed by Petschek (1964) is regarded as the next major advance from the Sweet-Parker (Sweet 1958, Parker 1957, 1963) model. Petschek suggested that a pair of MHD shocks are attached to a tiny diffusion region. Here the current distribution is concentrated within the shocks and, primarily, around the neutral point.

We will only discuss the important features of the Petschek model but note that a more thorough investigations were given by Vasyliunas (1975) and Forbes & Priest (1987). It must also be mentioned that extensions of the Petschek model have surfaced. A notable example is the Sonnerup model of magnetic reconnection (Sonnerup 1970, Yeh & Axford 1970). Sonnerup, and others, suggested that another set of MHD shocks are attached to the current sheet.

Petschek assumes (see Biskamp 1993) that the current sheet is extremely small and

$$l \sim L \sim \eta,$$

$$u \sim v \sim \eta^0,$$

which implies that the aspect ratio L/l is independent of η.

Now Petschek adopts the Sweet-Parker assumption that

$$B_{\text{sheet}} \sim \eta^0,$$

and so

$$J_0 \approx \frac{B_{\text{sheet}}}{l} \sim \eta^{-1}.$$

Our two measures of energy release can now be evaluated. We have

$$\frac{\partial \psi}{\partial t} = \eta J_0 \sim \eta^0,$$

which is fast and

$$W_\eta \approx \eta J_0^2 l L \sim \eta^1,$$

which is defined to be slow.

It must be understood that the presence of MHD shocks and the proposed scalings for l, L, B_{sheet} are all assumptions by Petschek. As the derivation given by Petschek is also highly qualitative, the reconnection model put forward appears questionable. We simply remark here that both analytical and numerical attempts have failed to confirm the Petschek assumptions (see Biskamp 1986).

3.2.3 The Forbes & Priest Analysis

A family of steady-state models were published by Forbes and Priest (Priest & Forbes 1986, Forbes & Priest 1987). Forbes and Priest (now abbreviated to FP) constructed two-dimensional linear solutions for an ideal MHD plasma. We remark that the derivation given below slightly differs from FP as their analysis can be generalised.

The steady-state MHD equations are given in Chapter 2. Taking $\eta = 0$ and specialising to an incompressible plasma gives

$$\mathbf{v}.\nabla\mathbf{v} = -\nabla^2\psi\nabla\psi - \nabla p, \tag{3.1}$$

$$E + \mathbf{v}.\nabla\psi = 0, \tag{3.2}$$

$$\nabla.\mathbf{v} = 0, \tag{3.3}$$

where $\rho = 1$ for simplicity.

Equations (3.1) to (3.3) are now linearised about the zeroth-order solution

$$E_0 = 0,$$

$$p_0 = \text{constant},$$

$$\psi_0 = +B_0 y \qquad y > 0,$$

$$\psi_0 = -B_0 y \qquad y < 0,$$

$$\mathbf{v}_0 = (0, 0).$$

Clearly the singularity in the magnetic field along $y = 0$ is a major concern. We point out that FP 'elude' this problem by regarding the discontinuity as a current sheet of negligible width.

The first-order equations can be expressed as

$$p_1 = B_0 P_1(y), \tag{3.4}$$

$$\nabla^2 \psi_1 = -\frac{\partial P_1}{\partial y}, \tag{3.5}$$

$$\mathbf{v}_1 = \frac{1}{B_0}(0, -E_1), \tag{3.6}$$

where P_1 is an *arbitrary* function and the subscript 1 signifies first-order terms. We remark that the P_1 chosen by FP reduces to a series of adjustable parameters – labelled b_n.

A boundary condition for ψ_1 now needs to be prescribed along the line of discontinuity. To meet this requirement, FP introduce a piecewise-linear function that contains another singularity. The location of this singularity determines the sheet length and occurs at a presupposed distance from the neutral point.

The second-order equations can be expressed as

$$p_2 = \frac{\partial P_1}{\partial y}\psi_1 + P_2(y), \tag{3.7}$$

$$\nabla^2 \psi_2 = -\frac{1}{B_0}\left(\frac{\partial^2 P_1}{\partial y^2}\psi_1 + \frac{\partial P_2}{\partial y}\right), \tag{3.8}$$

$$\mathbf{v}_2 = \frac{E_1}{B_0^2}\left(\frac{\partial \psi_1}{\partial x} + x\frac{\partial P_1}{\partial y}, \frac{\partial \psi_1}{\partial y} - \frac{B_0 E_2}{E_1}\right), \tag{3.9}$$

where P_2 is another *arbitrary* function and the subscript 2 denotes second-order terms.

Obviously the linear solutions of FP now depend on the arbitrary functions P_1 and P_2. How these functions are prescribed will determine the structure of the magnetic field and plasma flow. Here we simply state that linearised solutions which different flow topologies can be readily established.

The main problem with the FP approach is the ideal nature of the plasma. By setting $\eta = 0$, a singularity in the magnetic field becomes inevitable. Whether this continuity can be treated as a current sheet of adjustable width and length is uncertain.

Our two measures of the reconnection rate can only be evaluated once l, L and $B_{\mathbf{sheet}}$ have been specified. However these diagnostics must be established via external arguments. Again it is apparent that global solutions that treat the current sheet in a self-consistent fashion are required. Only then can reconnection rates be determined convincingly.

3.3 Time-Dependent Models

3.3.1 The Craig & McClymont Analysis

The approximate solutions of Craig & McClymont (1991,1993) are now established. The authors linearise the MHD equations after specialising to $\beta = 0$ *i.e.* a pressureless plasma.

The pressureless MHD equations are

$$\rho(\frac{\partial \mathbf{v}}{\partial t} + \mathbf{v}.\nabla\mathbf{v}) = -\nabla^2\psi\nabla\psi, \tag{3.10}$$

$$\frac{\partial \psi}{\partial t} + \mathbf{v}.\nabla\psi = \eta\nabla^2\psi, \tag{3.11}$$

$$\frac{\partial \rho}{\partial t} + \nabla.(\rho\mathbf{v}) = 0. \tag{3.12}$$

Equations (3.10) and (3.12) are now linearised about the zeroth-order solution

$$\rho_0 = 1,$$

$$\psi_0 = \frac{1}{2}(y^2 - x^2),$$

$$\mathbf{v}_0 = (0,0).$$

This gives

$$\frac{\partial \mathbf{v}_1}{\partial t} = -\nabla^2\psi_1\nabla\psi_0, \tag{3.13}$$

$$\frac{\partial \psi_1}{\partial t} + \mathbf{v}_1.\nabla\psi_0 = \eta\nabla^2\psi_1, \tag{3.14}$$

$$\frac{\partial \rho_1}{\partial t} + \nabla.\mathbf{v}_1 = 0, \tag{3.15}$$

where the subscript 1 signifies a first-order perturbation. It can been seen from (3.13) that $\mathbf{v}_1$ is be directed perpendicular to contours of ψ_0.

Combining (3.13) and (3.14) gives

$$\ddot{\psi} = r^2\nabla^2\psi + \eta\nabla^2\dot{\psi}, \tag{3.16}$$

in polar co-ordinates. Here the redundant 1 subscript has been dropped and dots signify time-derivatives.

Equation (3.16) governs the evolution of the first-order magnetic field. Solutions of (3.16) can be determined when the initial distribution and boundary conditions are specified. On the outer boundary (at $r = 1$ say) we demand that ψ remain constant in time. This constraint means that the magnetic field is 'line-tied' to the outer boundary. Meanwhile the inner condition is simply determined by the symmetry of the magnetic field.

It is a straight forward exercise to model (3.16) on computer. However an approximate theory that provides diagnostic scalings is now given. We note that the following scalings were indeed confirmed by numerical simulation.

The reconnection system consists of two fundamental regions. In the neighbourhood of the neutral point, equation (3.16) reduces to

$$\dot{\psi} = \eta \nabla^2 \psi, \tag{3.17}$$

which is a standard diffusion equation.

Far from the neutral point one has

$$\ddot{\psi} = r^2 \nabla^2 \psi, \tag{3.18}$$

which is wave equation and the wave speed is given by r.

The radius of the diffusion region can be estimated from (3.16). One has

$$r_c \sim \eta^{1/2},$$

where r_c denotes the critical radius.

A separation of variables technique allows solutions of (3.17) to be written as

$$\psi(r, \theta, t) = \sum_m J_m \left[\left(\frac{\lambda}{\eta} \right)^{1/2} r \right] \, \mathrm{e}^{\mathrm{i}m\theta} \mathrm{e}^{\lambda t},$$

where J_m represents a Bessel function and λ is some constant. Hence the current distribution at the neutral point is

$$\nabla^2 \psi = \left(\frac{\lambda}{\eta} \right) \psi.$$

The only Bessel function which is finite at the neutral point is J_0 so only the $m = 0$ mode has the 'ability' to reconnect field lines.

Concentrating on the $m = 0$ mode allows (3.18) to be reduced to

$$\ddot{\psi} = r \frac{\partial}{\partial r} (r \frac{\partial \psi}{\partial r}),$$

which has the solution

$$\psi(r,t) = \frac{1}{2}\left[\psi^{\mathrm{IN}}(re^{-t}) + \psi^{\mathrm{OUT}}(re^{+t})\right],$$

where ψ^{IN} and ψ^{OUT} are determined by the initial conditions. This solution implies that the perturbation field splits into an inward ψ^{IN} pulse and an outward ψ^{OUT} travelling pulse. However, once the outgoing pulse is reflected at the outer boundary, both pulses travel inward.

We now qualitatively interpret the Craig & McClymont solutions. An initial disturbance of the equilibrium magnetic field will propagate toward the neutral point in a wave-like fashion. During this implosion, the perturbation energy gets focussed into a narrow annulus. Once the the critical radius r_c is reached, the plasma resistivity becomes important. The incoming disturbance diffuses inward and reconnection is initiated at the neutral point.

Our attention now focuses on the energy liberation. The magnetic energy within the incoming annulus can be approximated by

$$E_{\mathrm{mag}} = \frac{1}{2}\int_S B^2 dS \approx \frac{1}{2}(B_{\mathrm{sheet}})^2 A, \tag{3.19}$$

which must be invariant with respect to η. Meanwhile the area A of the region encompassing this energy is given by

$$A = \pi r_c^2 \sim \eta.$$

Substituting this expression into (3.19) gives

$$B_{\mathrm{sheet}} \sim \eta^{-1/2},$$

and so

$$J_0 \approx \frac{B_{\mathrm{sheet}}}{r_c} \sim \eta^{-1}.$$

The scaling of B_{sheet} indicates that the magnetic field along the diffusive boundary will build-up as η is reduced. This result contrasts the Sweet-Parker and Petschek models where B_{sheet} is assumed to be independent of η.

The flux annihilation rate scales as

$$\frac{\partial \psi}{\partial t} = \eta J_0 \sim \eta^0,$$

and the Ohmic dissipation rate scales as

$$W_\eta \approx \eta J_0^2 A \sim \eta^0.$$

Hence both measures of energy release are fast.

Obviously problems with the Craig & McClymont analysis will arise when the linearisation of the MHD equations breaks down. To retain validity, one must have

$$|\nabla\psi| \ll |\nabla\psi_0| = r.$$

At the critical radius r_c we then have

$$|\nabla\psi| \ll \eta^{1/2},$$

which is a severe restriction.

Another point of concern is the pressureless assumption – taking $\beta = 0$. As discussed in Chapter 2, the plasma pressure is expected to play a crucial role in magnetic reconnection. Thus solutions retaining the pressure term are now required.

3.3.2 The Craig & Watson Analysis

A non-linear extension of the Craig & McClymont (1991, 1993) analysis was given by Craig & Watson (1992). It can be expected that the first-order disturbance of the zeroth-order magnetic field in the Craig & McClymont solutions does not remain small. As the imploding annulus approaches the neutral point, the non-linearity in the MHD equations becomes important. Non-linear effects subsequently overwhelm the linearised solution and the circular perturbation will collapse toward a one-dimensional current sheet. Clearly, if this degeneration becomes substantial, the linear solutions established by Craig & McClymont will not be acceptable.

A simple description of the non-linear collapse is given by the one-dimensional equivalent of (3.16). This would be

$$\ddot{\psi} = x^2 \frac{\partial^2 \psi}{\partial x^2} + \eta \frac{\partial^2 \dot{\psi}}{\partial x^2}, \tag{3.20}$$

which implies that

$$l \sim \eta^{1/2},$$

$$L \sim \eta^0,$$

where l and L are the sheet width and length respectively.

Equation (3.19) can now be expressed as

$$E_{\mathrm{mag}} \sim (B_{\mathrm{sheet}})^2 l \sim \eta^0.$$

On combining these expressions we find

$$B_{\mathrm{sheet}} \sim \eta^{-1/4},$$

$$J_0 \approx \frac{B_{\text{sheet}}}{l} \sim \eta^{-3/4}.$$

Our measures of energy release can now be determined. Hence

$$\frac{\partial \psi}{\partial t} = \eta J_0 \sim \eta^{1/4},$$

which is slow while

$$W_\eta \approx \eta J_0^2 A \sim \eta^0,$$

which is fast.

This non-linear analysis has clearly advanced upon the linear analysis of Craig & McClymont. Now we no longer have a severe restriction upon the magnitude of the perturbed magnetic field. Also the Craig & Watson analysis now takes into account the non-linearity of the problem. However the plasma is still pressureless ($\beta = 0$) and the non-linear 'modification' is somewhat qualitative.

3.3.3 The Biskamp & Welter Simulations

The resistive coalescence of two-dimensional magnetic islands provides one mechanism for magnetic reconnection. A paper by Biskamp & Welter (1980) studied the interaction of two adjacent magnetic islands in an incompressible plasma. Here we shall summarise the results of Biskamp & Welter (now abbreviated to BW) then determine scalings via the energy argument in the Craig & McClymont (1992) analysis. It is also noted that similar diagnostic scalings were observed in the compressible simulations by Rickard & Craig (1993).

The BW simulations indicated that

$$l \sim \eta^{2/3}, \qquad L \sim \eta^0,$$

along with

$$B_{\text{sheet}} \sim \eta^{-1/3},$$

and so

$$J_0 \approx \frac{B_{\text{sheet}}}{l} \sim \eta^{-1}.$$

The inflow and outflow scaled as

$$u \sim \eta^{1/3}, \qquad v \sim \eta^{-1/3}.$$

It should be mentioned that no graphical evidence for these proposed scalings was given.

As demonstrated by Rickard & Craig (1993), the BW scalings can be established via the energy argument introduced by Craig & Watson (1992). The non-linear arguments give

$$L \sim \eta^0,$$

and so (3.19) implies

$$B_{\text{sheet}}^2 l \sim \eta^0. \tag{3.21}$$

The following relationships from our Sweet-Parker analysis in Chapter 2 can be retrieved: (*i*) conservation-of-mass within the current sheet

$$uL \approx vl,$$

(*ii*) the diffusion relation at the current sheet onset

$$u \approx \frac{\eta}{l},$$

(*iii*) the speed that plasma is ejected from the current sheet

$$v \approx v_a = B_{\text{sheet}},$$

where v_a is the local Alfvén speed.

Combining (*i*) to (*iii*) and (3.21) gives

$$u \sim \eta^{1/3}, \qquad v \sim \eta^{-1/3},$$

$$l \sim \eta^{2/3}, \qquad L \sim \eta^0,$$

$$B_{\text{sheet}} \sim \eta^{-1/3}, \qquad J_0 \sim \eta^{-1},$$

which are the BW scalings.

Our measures of energy release can now be determined. The rate of flux annihilation is

$$\frac{\partial \psi}{\partial t} = \eta J_0 \sim \eta^0,$$

which is fast and the Ohmic dissipation rate scales as

$$W_\eta \approx \eta J_0^2 l L \sim \eta^{-1/3},$$

and is regarded as ultra-fast.

An independent study by Strauss (1990) gave identical scalings for l and J_0. Here the author simulated a three-dimensional magnetic flux tube driven by an applied plasma flow. However it must be emphasised that only a modest range of η was simulated by Strauss – $(2.4 \times 10^{-3} \leq \eta \leq 3 \times 10^{-4})$. Moreover the graphs of l and J_0 in the Strauss paper indicate that the proposed scalings breakdown for the small values of η.

The simulations of BW are not conclusive. The range of η simulated by BW, namely $(2 \times 10^{-3} \leq \eta \leq 1 \times 10^{-4})$, is still many orders of magnitude greater than the coronal values of $\eta = O(10^{-12})$. Of even greater concern is that no justification of the proposed scalings was presented. Results from the Strauss paper discussed above suggests that the BW scalings are not valid as η approaches coronal values.

3.4 Summary

The weaknesses of the Sweet-Parker, Petschek and Forbes & Priest models are readily apparent. Firstly it is assumed that the current sheet is effectively insensitive to the outer environment. Next the current sheet is simply 'patched' onto an outer solution with the transition region being neglected. Numerical simulations (*e.g.* the Biskamp & Welter simulations) and semi-analytic solutions (*e.g.* the Craig & McClymont analysis) show that the current sheet and outer solution cannot be treated separately. Obviously a more global treatment of the reconnection problem is needed.

The linear analysis of Section 3.5 and the non-linear extension in Section 3.6 also contain shortcomings. Discarding the plasma pressure by setting $\beta = 0$ and linearising the governing equations are significant simplifications. Numerical simulations (*e.g.* DeLuca & Craig 1992) of the exact MHD equations show that both non-linearity and plasma pressure play important roles in reconnection process.

Numerical attempts at solving the reconnection problem have been largely unsuccessful. This lack of success can be mainly attributed to the extremely small value of η for coronal plasmas. The intense localisation of the current sheet means that resolution limitations prevent the simulation of realistic η values. This problem is clearly illustrated by the simulations conducted by Biskamp & Welter and Strauss. Here it became apparent that trends holding for large η values *may* breakdown for more realistic values.

CHAPTER 4

A Numerical Study

4.1 Introduction

A dynamical model of magnetic reconnection was proposed by DeLuca & Craig (1992). This compressible model was independent of one co-ordinate and was periodic in the other dimensions. Numerical simulations by DeLuca & Craig (now abbreviated to DC) hinted that reconnection *may* stall (saturate) for small values of plasma resistivity. However, due to resolution constraints, the reality of stalling was not confirmed.

The primary objective of this chapter is to determine whether reconnection stalls in the DC model. By employing different numerical methods to solve the MHD equations, the resolution difficulties encountered by DC are considerably eased. Far smaller values of η are simulated and so the stalling question is answered. A preliminary summary of some results presented here have been published in Henton (1993) and Craig, Henton & Rickard (1993). Here we give a more detailed examination of the stalling mechanism.

In Section 4.2 we formulate the original DC model and a two-dimensional variant. Section 4.3 describes the evolution of the planar magnetic field and plasma velocities for both models. Section 4.4 gives various diagnostics relating to the current sheet and demonstrates that reconnection does indeed stall. A detailed study of the stalling mechanism then follows in Section 4.5. Finally a summary of our findings is given in Section 4.6.

4.2 Numerical Formulation

4.2.1 Governing Equations

The time-dependent MHD equations were given in Chapter 2. With a polytropic approximation for the plasma pressure these equations become

$$\rho(\frac{\partial \mathbf{v}}{\partial t} + \mathbf{v}.\nabla\mathbf{v}) = (\nabla \times \mathbf{B}) \times \mathbf{B} - \beta\nabla\rho^{\gamma}, \tag{4.1}$$

$$\frac{\partial \mathbf{B}}{\partial t} = \nabla \times (\mathbf{v} \times \mathbf{B}) + \eta\nabla^2\mathbf{B}, \tag{4.2}$$

$$\frac{\partial \rho}{\partial t} + \nabla.(\rho\mathbf{v}) = 0, \tag{4.3}$$

with the constraint

$$\nabla.\mathbf{B} = 0. \tag{4.4}$$

Clearly γ, β and η are external parameters which govern the time-dependent system. We set $\gamma = \frac{5}{3}$ which corresponds to an adiabatic gas law. However we remark that our particular choice for γ should not be a critical issue.

The DC model is independent of the $\hat{\mathbf{z}}$ co-ordinate. Hence we now express

$$\mathbf{v}(x, y, t) = (\mathbf{u}, w),$$

$$\mathbf{B}(x, y, t) = (\psi_y, -\psi_x, b).$$

Here $\mathbf{u}(x, y, t)$ and $w(x, y, t)$ denote the planar component and z-component of the plasma flow respectively. Meanwhile $\psi(x, y, t)$ is a planar magnetic flux function while $b(x, y, t)$ represents the z-component of the magnetic field.

Introduction of $\psi, b, \mathbf{u}, w$ allows us to rewrite (4.1) to (4.3) as

$$\frac{\partial \rho}{\partial t} + \nabla.(\rho \mathbf{u}) = 0, \tag{4.5}$$

$$\rho(\frac{\partial \mathbf{u}}{\partial t} + \mathbf{u}.\nabla \mathbf{u}) = -\nabla^2 \psi \nabla \psi - \frac{1}{2}\nabla b^2 - \beta \nabla \rho^\gamma, \tag{4.6}$$

$$\rho(\frac{\partial w}{\partial t} + \mathbf{u}.\nabla w) = (\nabla \psi \times \hat{\mathbf{z}}).\nabla b, \tag{4.7}$$

$$\frac{\partial \psi}{\partial t} + \mathbf{u}.\nabla \psi = \eta \nabla^2 \psi, \tag{4.8}$$

$$\frac{\partial b}{\partial t} + \nabla.[\mathbf{u}b - (\nabla \psi \times \hat{\mathbf{z}})w] = \eta \nabla^2 b. \tag{4.9}$$

Our numerical codes are constructed from this set of '$2\frac{1}{2}$-dimensional' equations.

4.2.2 The Models

We now describe our two reconnection models. The first is the original DC model (Model A) while the second is a two-dimensional variation (Model B).

(i) Model A comprises an equilibrium

$$\rho^E = 1,$$

$$\mathbf{u}^E = \mathbf{0},$$

$$w^E = 0,$$

$$\psi^E = \sin(x)\sin(y),$$

$$b^E = \sqrt{2}\psi^E,$$

and a perturbation

$$\psi^P = \cos^2(x).$$

(*ii*) Model B comprises an equilibrium

$$\rho^E = [1 + \frac{1}{\beta}(\psi^E)^2]^{1/\gamma},$$

$$\mathbf{u}^E = \mathbf{0},$$

$$\psi^E = \sin(x)\sin(y),$$

with w and b always being zero. The perturbation of Model A is then added to this equilibrium.

The difference between the equilibriums for each model is clear. Model A requires a z-component in the magnetic field, namely b, to balance the equilibrium Lorentz force. On the other hand, this force is compensated by a background plasma pressure in Model B. Therefore Model B is entirely two-dimensional.

A great advantage of both models is that the specification of outer boundary conditions is *not* required. Since the dependent variables are periodic in both dimensions, the MHD system is already fully specified. We note the problems arising from determining suitable boundary conditions were discussed in Chapter 2.

It must be appreciated that ψ^E provides an equilibrium solution only when $\eta = 0$. As ψ_E contains finite current structures

$$\mathbf{J}^E = -\nabla^2(\psi^E)\hat{\mathbf{z}} = 2\sin(x)\sin(y)\hat{\mathbf{z}},$$

plasma resistivity must continually dissipate magnetic energy from the equilibrium solution. However the energy released via $\mathbf{J}^E$ will not be significant for small enough values of η. Hence, to all intents and purposes, ψ^E can be regarded as an equilibrium.

The equilibrium magnetic field for the range $(-\pi : \pi, -\pi : \pi)$ is shown in Figure 4.1a. Here four O-type neutral points centred at $(\pm\frac{\pi}{2}, \pm\frac{\pi}{2})$ and $(\pm\frac{\pi}{2}, \mp\frac{\pi}{2})$ are seen. Adding the perturbation, as illustrated by Figure 4.1b, transforms the top-right and bottom-left O-type points into X-type neutral points that separate pairs of magnetic islands. These X-type points are centred at $(\frac{\pi}{2}, \frac{\pi}{2})$ and $(-\frac{\pi}{2}, -\frac{\pi}{2})$ respectively and define the boundary for each island pair. Meanwhile the top-left and bottom-right O-type points expand to 'replenish' the newly vacated regions of magnetic field and so become roughly elliptical.

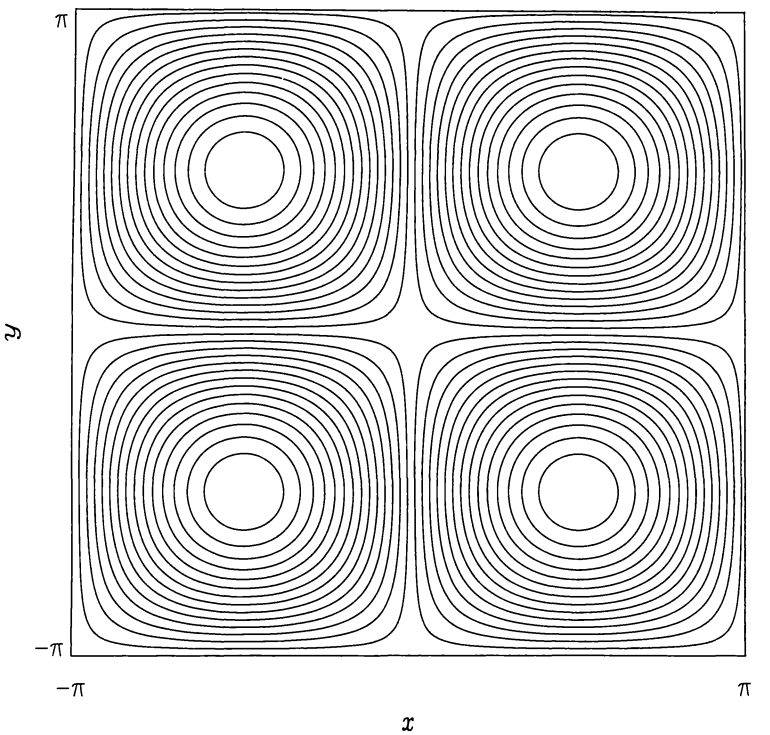


Figure 4.1a. Contour plot of ψ^E.

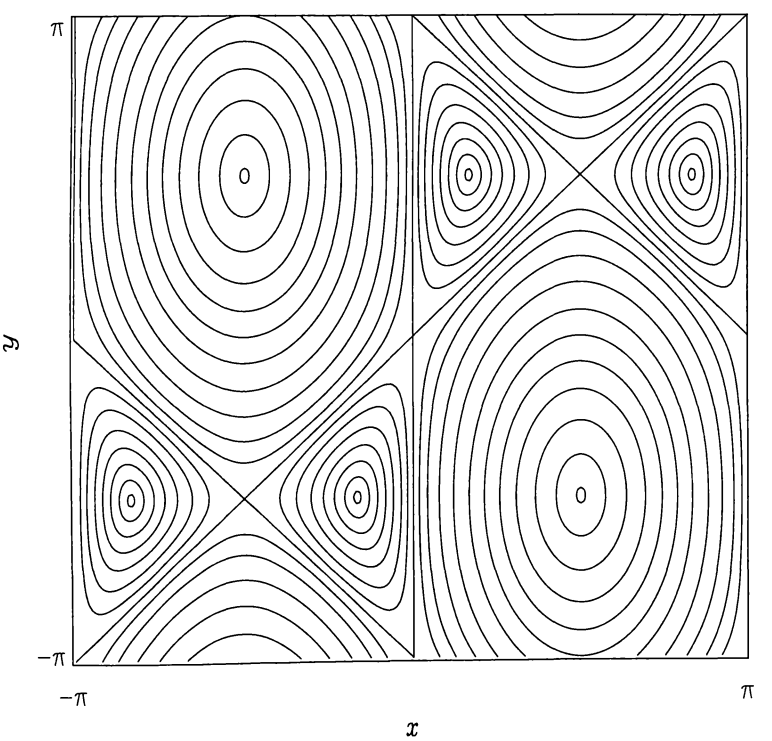


Figure 4.1b. Contour plot of $\psi^E + \psi^P$.

We point out that in the top-left and bottom-right quadrants, no topological difference exists between the perturbed field of Figure 4.1b and the equilibrium field in Figure 4.1a. Thus no reconnection needs to occur here. However the remaining two quadrants have become X-type neutral points and *must* reconnect to regain their O-type status.

4.2.3 Our Numerical Approach

The numerical code used in this study was adapted from the Rickard & Craig (1993) code which had been based on Craig & Watson (1992). A two-step finite-difference scheme is employed to solve (4.5) to (4.9). An implicit Lax-Wendroff step is first used to update $\rho, \mathbf{u}$ and w. This is followed by an Alternating Direction Implicit (ADI) step to update the remaining variables ψ and b. The ADI scheme uses time-averaged values for the $\rho, \mathbf{u}, w$ while the implicitness parameter $\theta = \frac{1}{2}$ (see DC). A more detailed description of the numerical code can be found in Henton (1993).

Our simulations use a uniformly spaced grid ($\Delta x = \Delta y = \Delta$). Naturally a non-uniform grid is another possibility. This option can help overcome the resolution difficulties encountered by most numerical approaches but, as illustrated in the following analysis, an increase in resolution will not be necessary here.

A current sheet contains very steep gradients and occurs over a small length-scale. Therefore only a minute portion of the mesh shall resolve this all-important structure. Different choices of resolution will therefore result in sheet profiles varying markedly. To handle this problem self-consistently, we resolve each current sheet equally by demanding

$$\frac{l}{\Delta} \approx 5,$$

where l is the sheet width and Δ is the mesh spacing. This obviously implies that 5 grid points will be located inside the current sheet. We remark that simulations with greater resolution only altered our numerical results by a few percent.

We first perform a set of simulations with different resolutions for a given value of η. After calculating the above ratio for each run, an improved level of resolution is determined. We continue this iterative procedure until our demand on resolution is met and then proceed onto another value of η. As a point of note, the ratios calculated from the DC diagnostics were around unity so the current sheet was being poorly resolved.

DC used a pseudo-spectral collocation method to solve the MHD equations. A major drawback with this numerical approach is that the choices of grid resolution are limited. In particular, the number of grid points in a given direction could only be 2^n where n is an

integer. Thus the DC code could not resolve each current sheet equally. We re-iterate that our finite-difference approach overcomes this problem.

4.2.4 Reduction of Domain

A primary advantage of our finite-difference approach is the reduction of the computational domain. By exploiting the periodicity of the dependent variables, the domain is decreased from $(-\pi,\pi;-\pi,\pi)$ (D_0 say) to $(-\frac{\pi}{2},\frac{\pi}{2};0,\frac{\pi}{2})$ (D_2 say). This can be most easily described in two steps with the aid of Figure 4.1b.

Step one reduces D_0 to $(-\frac{\pi}{2},\frac{\pi}{2};-\frac{\pi}{2},\frac{\pi}{2})$ (D_1 say) by invoking the symmetries (s) and anti-symmetries (a) as listed in Table 4.1.

	$x=-\frac{\pi}{2}$	$x=\frac{\pi}{2}$	$y=-\frac{\pi}{2}$	$y=\frac{\pi}{2}$
ρ	s	s	s	s
u	a	a	s	s
v	s	s	a	a
w	a	a	a	a
ψ	s	s	s	s
b	s	s	s	s

Table 4.1. Symmetries (s) and anti-symmetries (a) of the dependent variables.

Step two reduces D_1 to D_2 after recognising that D_1 can be regained by rotating D_2 through 180^o about the point (0,0). Thus all the necessary 'information' for simulating D_1 is contained in D_2.

By implementing both steps, run time is reduced by more than a factor of eight. Obviously this gain will allow significantly smaller values of η to be simulated. We emphasise that the pseudo-spectral collocation method forced DC to model the entire domain.

4.3 A Sample Simulation

With the aid of the sample simulation in Figure 4.2, we now discuss the evolution of Model A – Model B is somewhat similar. We have focussed our attention on the planar magnetic field ψ (top panel) and planar velocities $\mathbf{u}$ (bottom panel) for the case $\eta = 5 \times 10^{-2}$ and $\beta = 10$. How these evolve will illustrate the important features of the reconnection process.

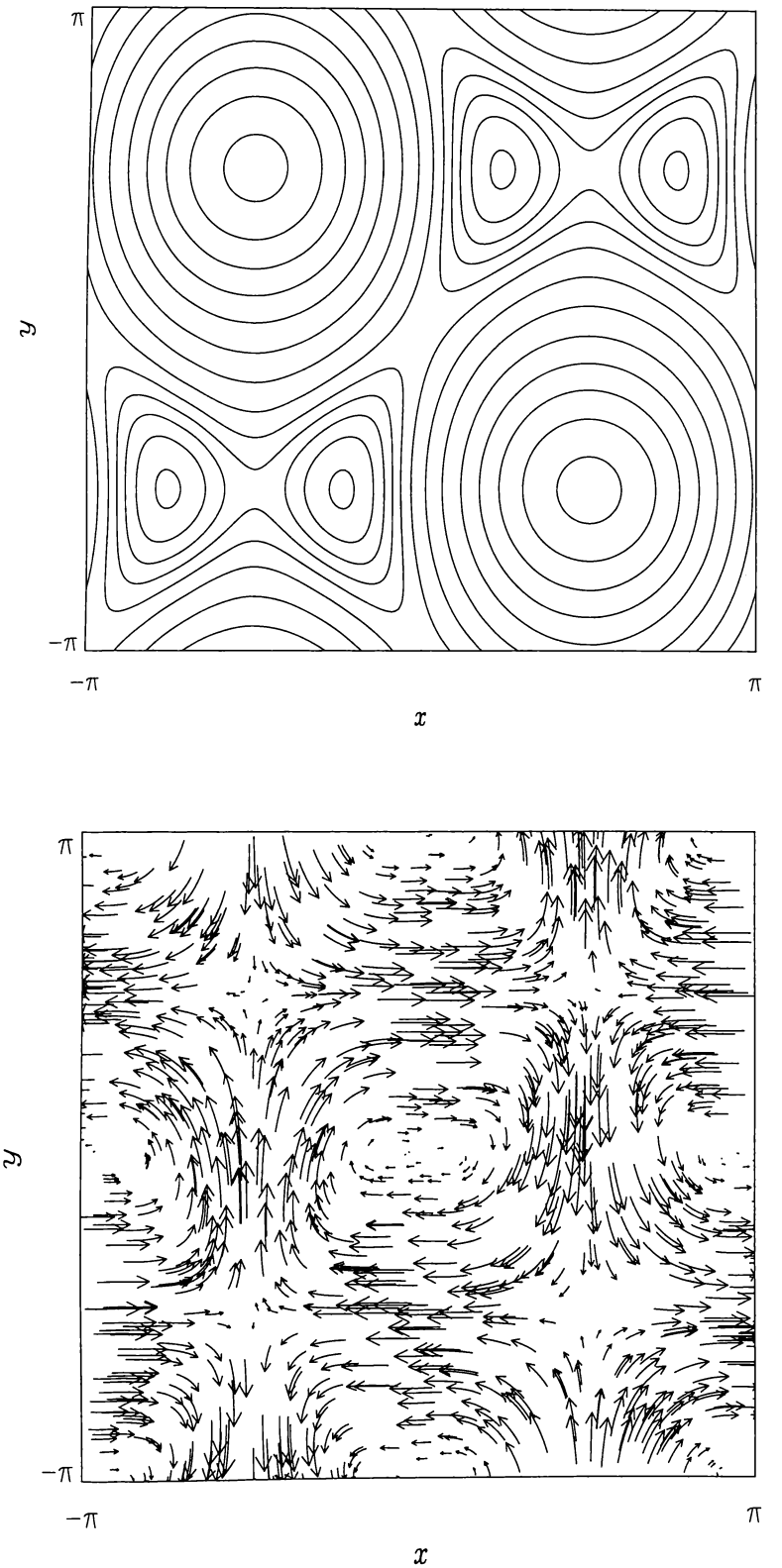


Figure 4.2a. Contour plot of ψ (top) and vector plot of $\mathbf{u}$ (bottom) for $\eta = 5 \times 10^{-2}, \beta = 10$ at $t = 1.0$ for Model A.

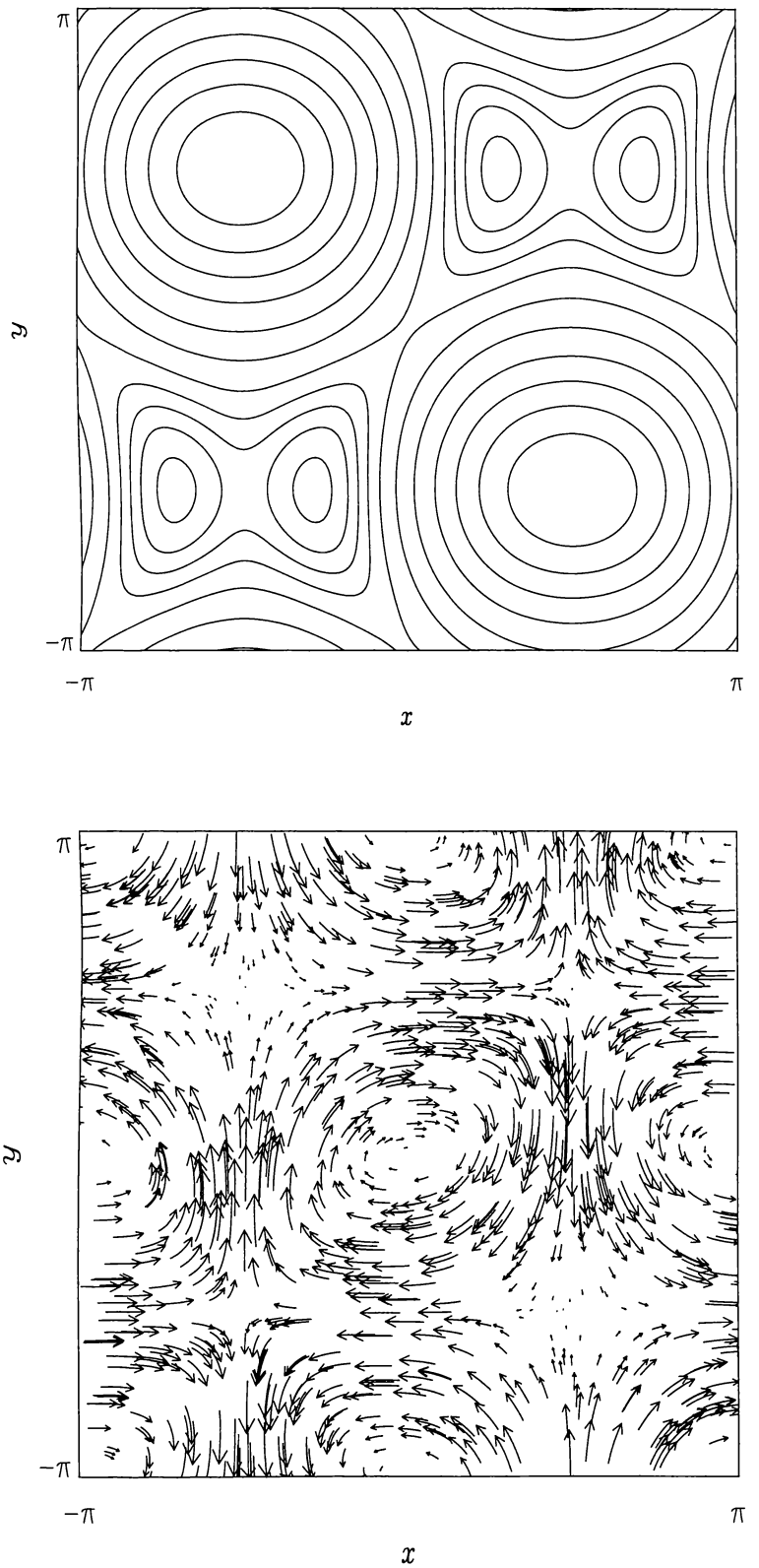


Figure 4.2b. Contour plot of ψ (top) and vector plot of $\mathbf{u}$ (bottom) for $\eta = 5 \times 10^{-2}, \beta = 10$ at $t = 1.5$ for Model A.

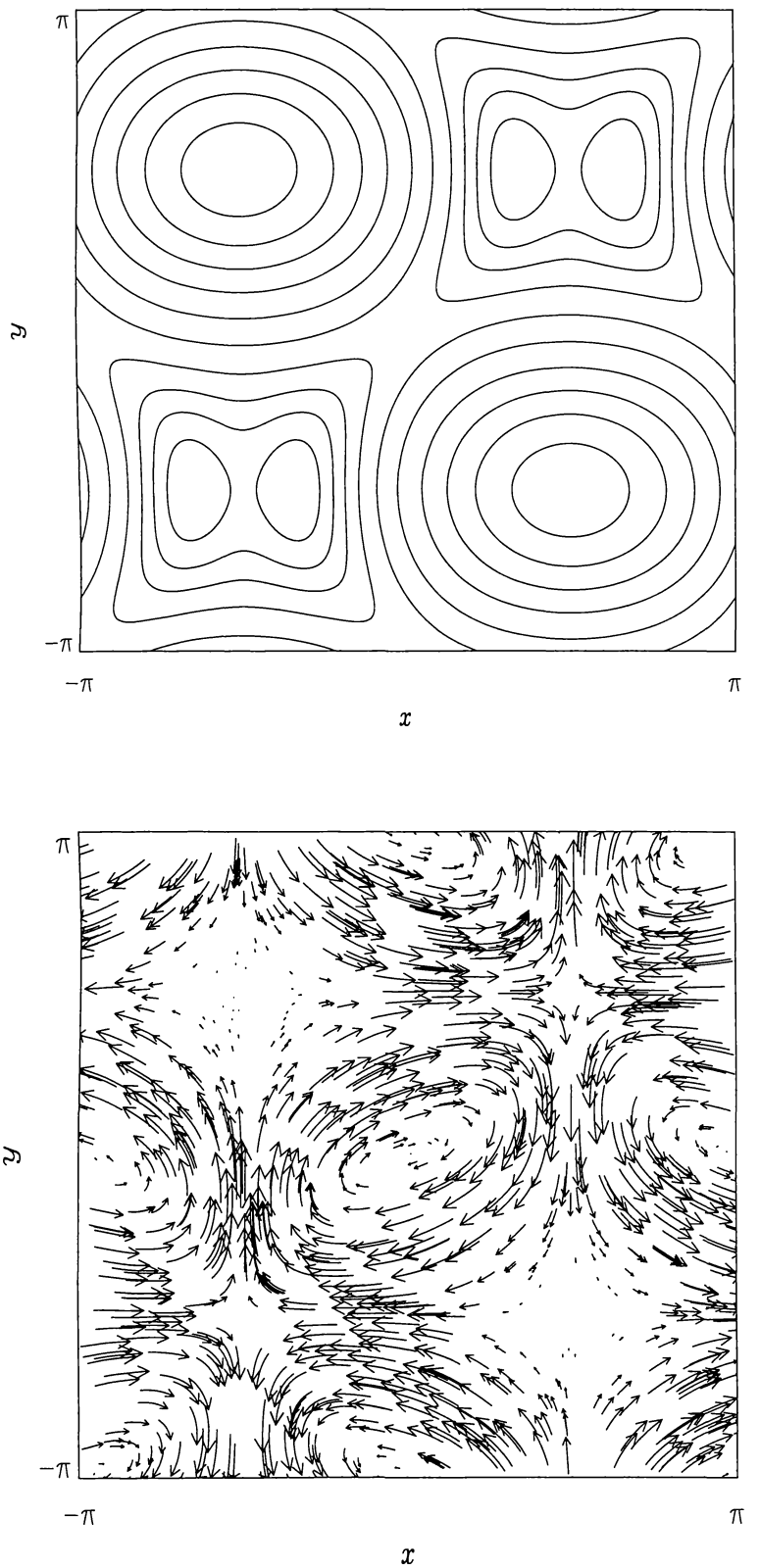


Figure 4.2c. Contour plot of ψ (top) and vector plot of $\mathbf{u}$ (bottom) for $\eta = 5 \times 10^{-2}, \beta = 10$ at $t = 2.0$ for Model A.

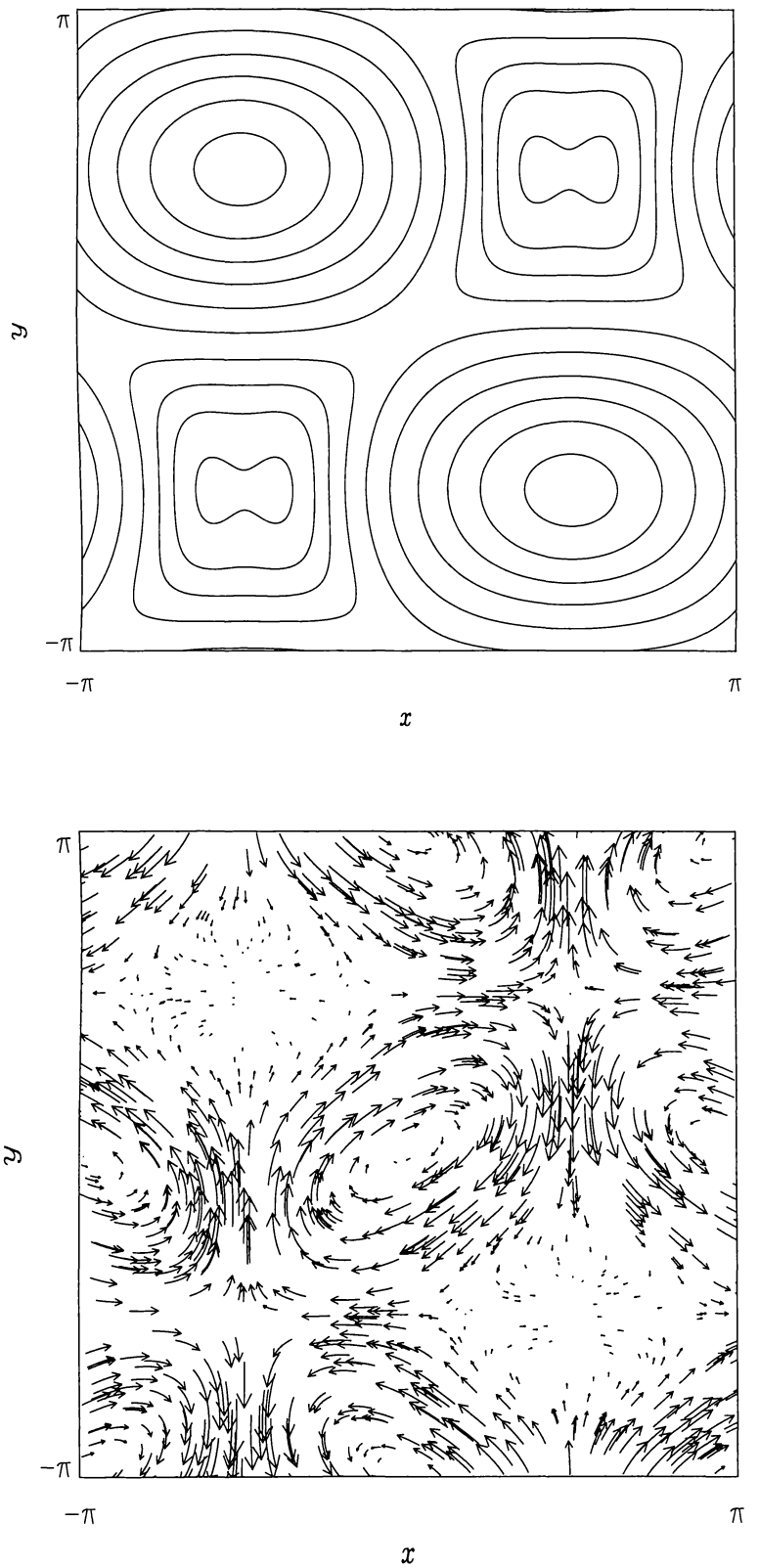


Figure 4.2d. Contour plot of ψ (top) and vector plot of $\mathbf{u}$ (bottom) for $\eta = 5 \times 10^{-2}, \beta = 10$ at $t = 2.5$ for Model A.

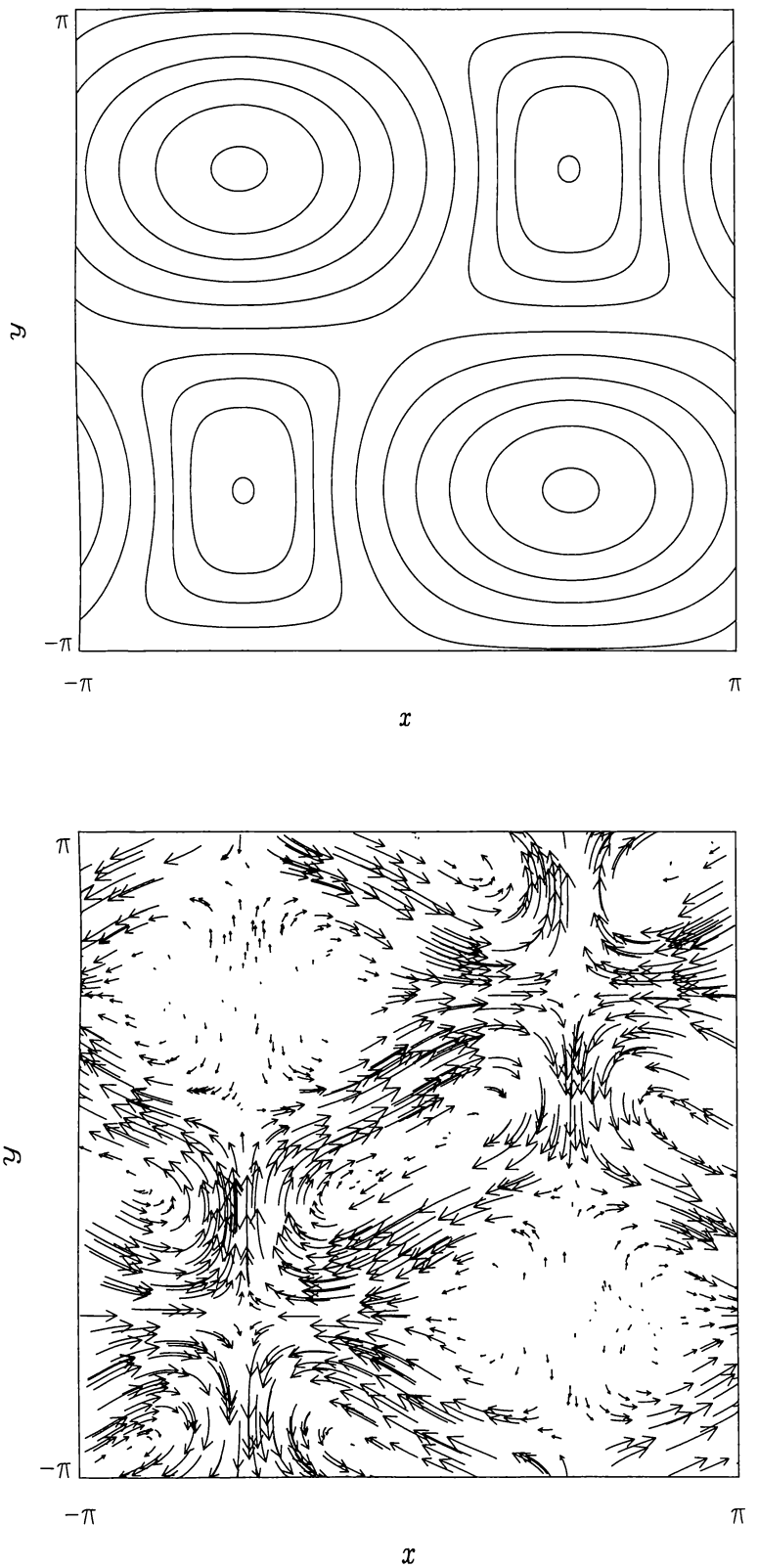


Figure 4.2e. Contour plot of ψ (top) and vector plot of $\mathbf{u}$ (bottom) for $\eta = 5 \times 10^{-2}, \beta = 10$ at $t = 3.0$ for Model A.

Figure 4.2a shows the system after 1.0 Alfvén-times with each successive plot being evaluated after a further 0.5 Alfvén-times have elapsed. Note that the numerical routine plotting $\mathbf{u}$ normalises arrows with respect to the maximum velocity. Hence arrows that are similar in size but in different diagrams are not likely to indicate identical speeds.

Two consecutive processes characterise the evolution of ψ and $\mathbf{u}$. First the elliptical magnetic field formations in the top-left and bottom-right quadrants 'pull in' plasma along their major axes and 'push out' plasma along their minor axes. Second the magnetic islands converge and undergo reconnection as they coalesce into a single O-type point. These coupled processes cause the global 'swirling' motions observed in Figure 4.2.

As illustrated in Figure 4.2c, the top-left and bottom-right quadrants reach a near equilibrium much earlier than the remaining two quadrants. Now plasma is refused entry into these quasi O-type points and an eddy coupling the plasma flows from each X-type point begins to emerge. Meanwhile the magnetic field depicted in Figure 4.2c indicates that most field lines have reconnected. Thus our MHD model has liberated most of the perturbation energy.

In Figure 4.2d we recognise that all topologically-altered magnetic field lines have reconnected. Thus the X-type neutral points seen in Figure 4.1b have undergone magnetic reconnection and become quasi O-type neutral points. Now, to fully regain the equilibrium status of Figure 4.1a, only plasma motions are required. As virtually all the perturbation energy has been released, we need not investigate the evolution any further.

4.4 Results

4.4.1 Diagnostics

An important issue that arises with time-dependent simulations is how to compare energy releases for different simulations. A fixed time for all simulations is not suitable because evolutions differ as η is varied. Obviously a characteristic event of the evolution is needed. The maximum current is a suitable event that also, by way of the symmetry, occurs at a fixed point in space – the neutral point. We therefore calculate the diagnostics introduced in Chapter 2 at the time of maximum current.

At the time of maximum current a considerable amount of energy has been focussed into a current sheet. Hence the MHD system must eradicate this accumulation of energy in a relatively short period of time. This energy loss could be identified with a solar flare.

The level of resolution needed to simulate a typical value of η is far beyond reach. Thus to determine how our models behave for realistic values, a technique that avoids such constraints is necessary. The customary procedure (see DC, Biskamp & Welter 1980), as detailed below, is to deduce asymptotic scalings from larger η.

We first assemble a compendium of runs by systematically reducing η while satisfying the resolution demand introduced earlier. This process continues until the run-time becomes too excessive. Next diagnostics for each run are evaluated numerically. Finally we calculate an η-dependency for each diagnostic which can be extrapolated down to astrophysical values.

Our diagnostics relating to the current sheet (see Chapter 2) are now presented. Here the top diagram corresponds to Model A and the bottom diagram is Model B while "*" signifies a $\beta = 1$ run and "$\times$" is a $\beta = 10$ run. It is noted that our results are consistent with DC for their range of η. However, once the smaller values of η have been incorporated, the scalings proposed by DC longer hold.

Figure 4.3 plots sheet width l versus η. Here we take l as distance from the neutral point to the location where current has dropped to zero. For large values of η we find that

$$l \sim \eta^{1/2},$$

which is indicated by the dashed line. As η declines we find

$$l \sim \eta^{0}.$$

We also note that l tends toward a lower value when β is reduced.

The sheet length L is plotted against η in Figure 4.4. Again we take L as the distance from the neutral point to where current reaches zero. This graph, where the vertical axis has standard units, clearly shows that

$$L \approx 1.2 \sim \eta^{0},$$

which is the same value quoted by DC.

Figure 4.5 plots B_{sheet} as a function of η. We take B_{sheet} as the peak value of the magnetic field approaching the neutral point. For large values of η we observe

$$B_{\text{sheet}} \sim \eta^{-1/2},$$

which is indicated by the dashed line. After further reduction of η we find

$$B_{\text{sheet}} \sim \eta^{0}.$$

Of interest here is that, unlike l, the saturation is relatively independent of β.

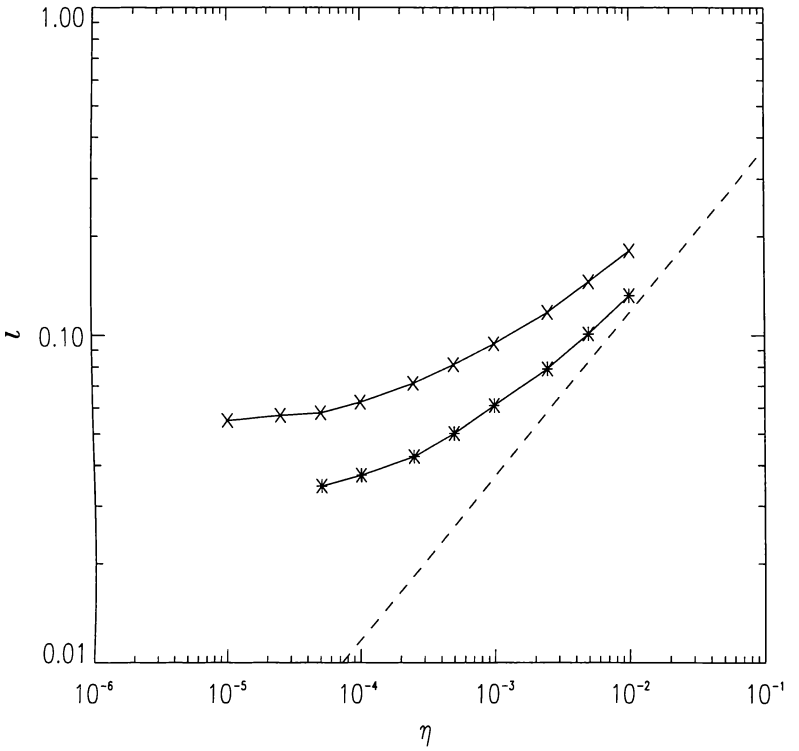


Figure 4.3a. Graph of l versus η where $\beta = 1$ (*) and $\beta = 10$ ($\times$) for Model A.

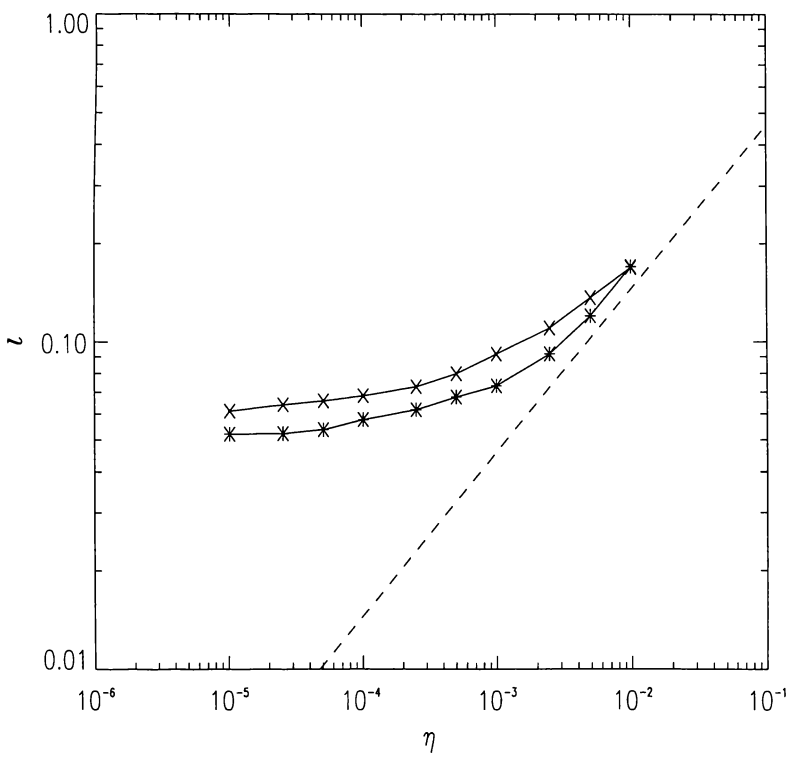


Figure 4.3b. Graph of l versus η where $\beta = 1$ (*) and $\beta = 10$ ($\times$) for Model B.

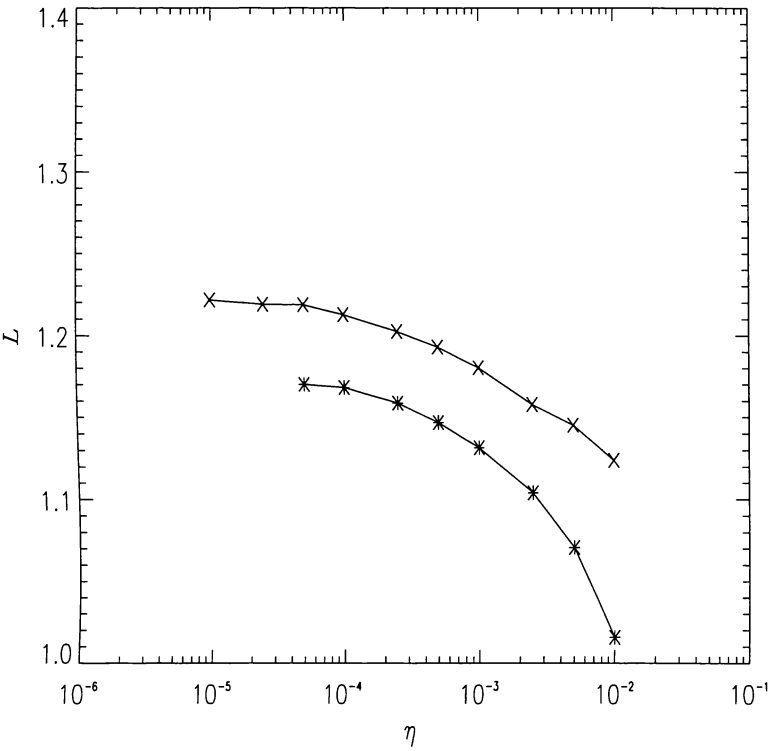


Figure 4.4a. Graph of L versus η where $\beta = 1$ (*) and $\beta = 10$ ($\times$) for Model A.

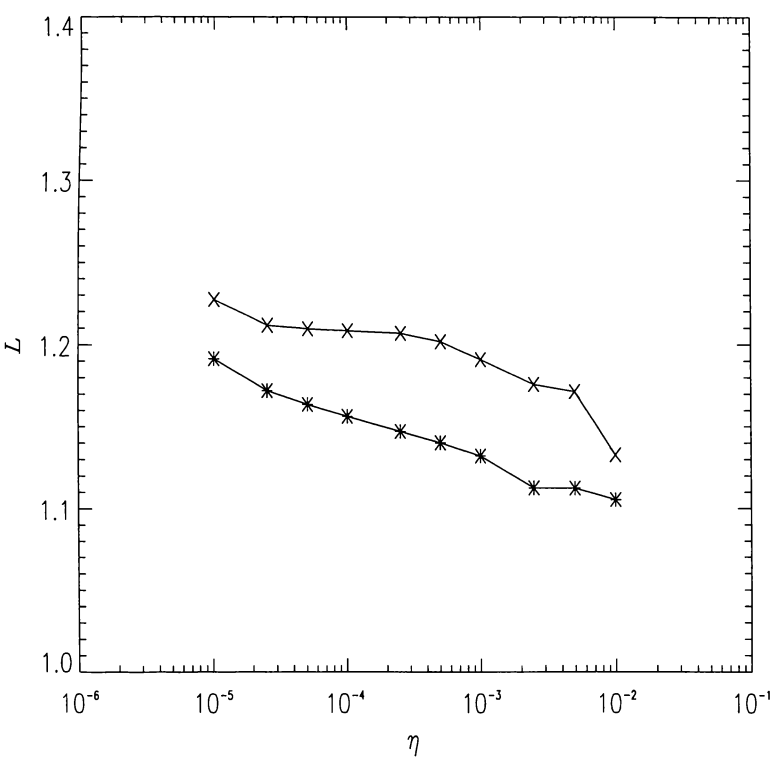


Figure 4.4b. Graph of L versus η where $\beta = 1$ (*) and $\beta = 10$ ($\times$) for Model B.

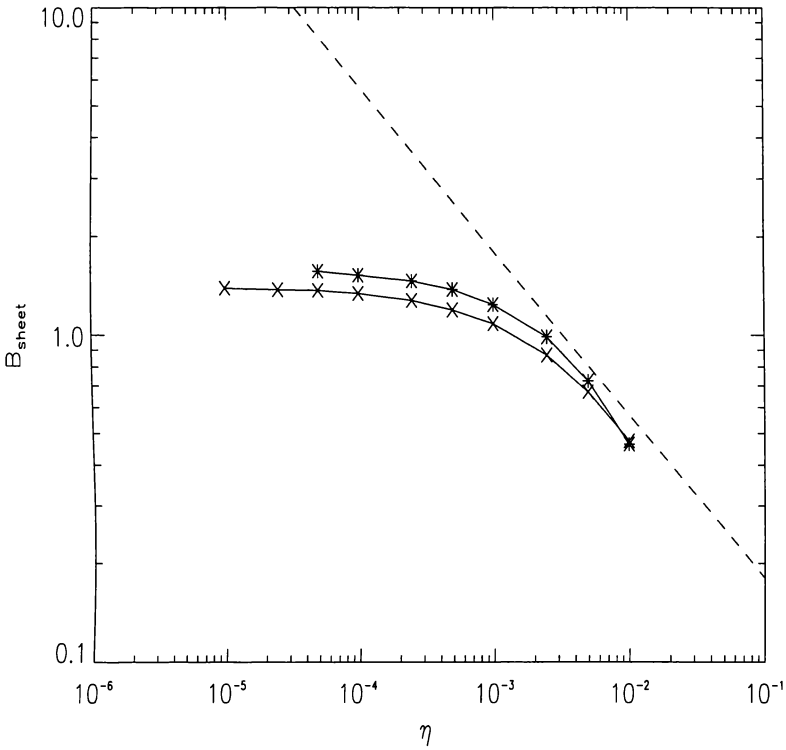


Figure 4.5a. Graph of B_{sheet} versus η where $\beta = 1$ (*) and $\beta = 10$ ($\times$) for Model A.

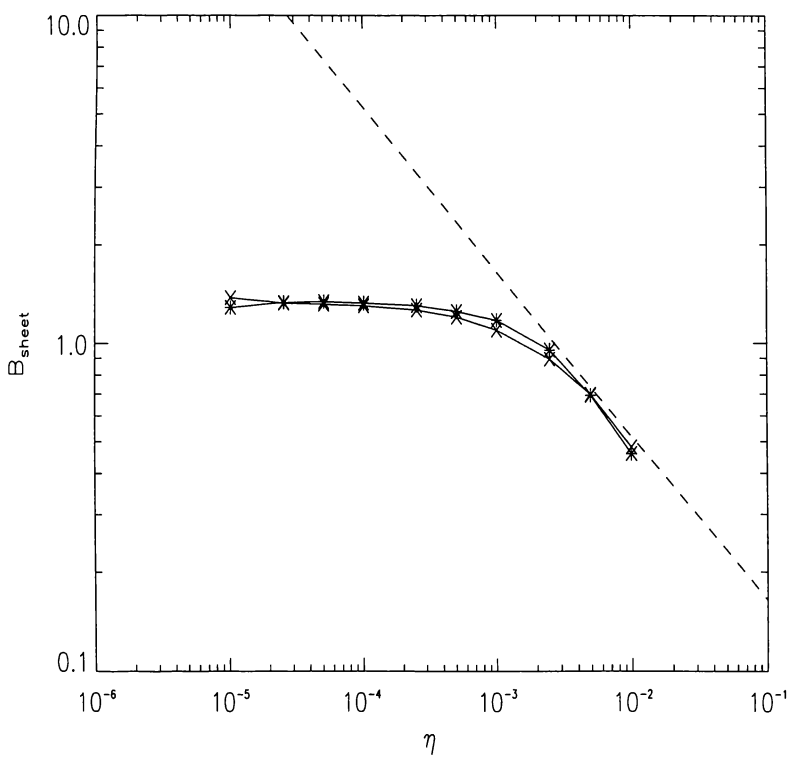


Figure 4.5b. Graph of B_{sheet} versus η where $\beta = 1$ (*) and $\beta = 10$ ($\times$) for Model B.

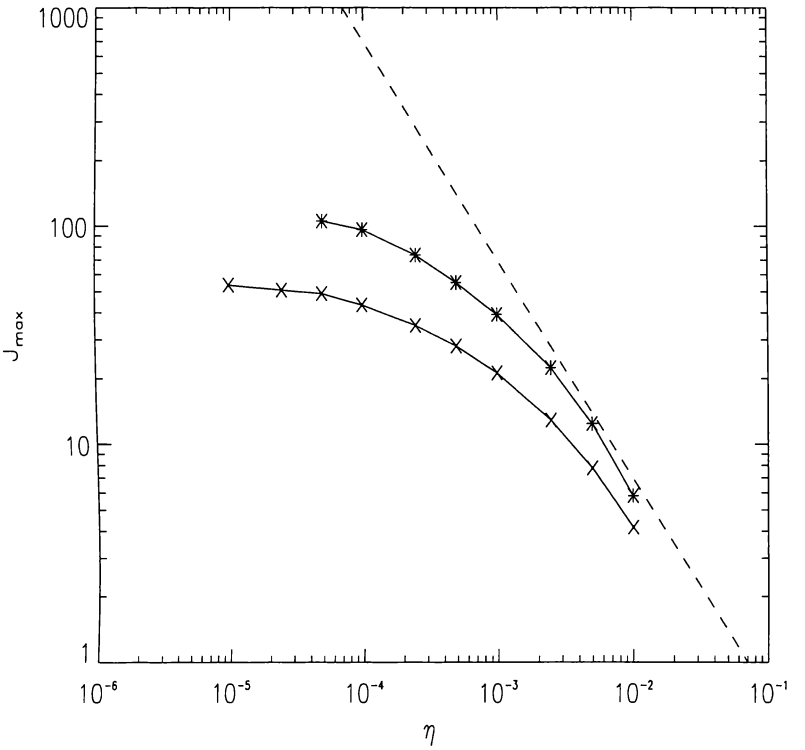


Figure 4.6a. Graph of J_0 versus η where $\beta = 1$ (*) and $\beta = 10$ ($\times$) for Model A.

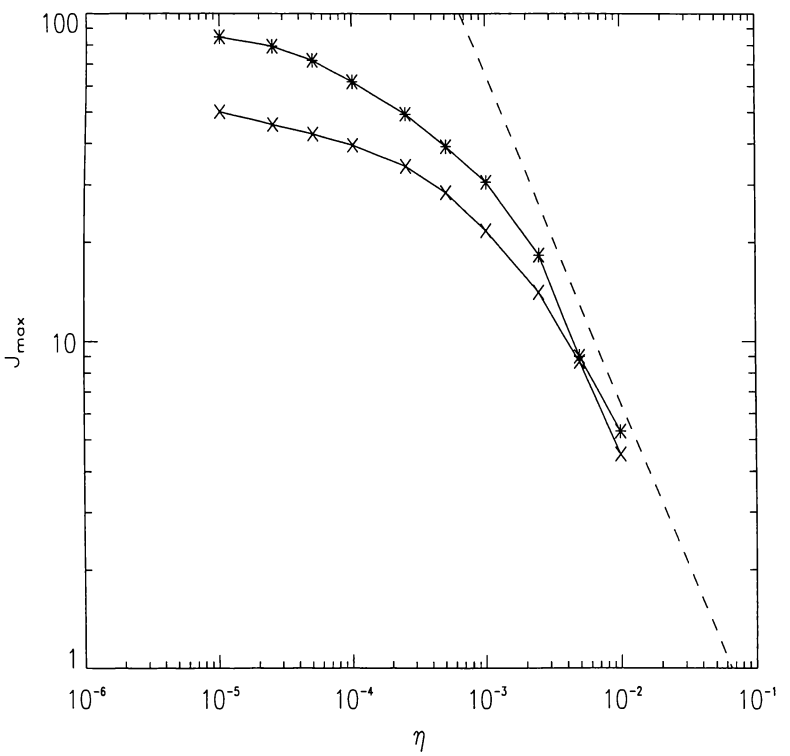


Figure 4.6b. Graph of J_0 versus η where $\beta = 1$ (*) and $\beta = 10$ ($\times$) for Model B.

The maximum current J_0 is plotted against η in Figure 4.6. When η is large we have

$$J_0 \sim \eta^{-1},$$

which is illustrated by a dashed line. As η is reduced

$$J_0 \sim \eta^0.$$

4.4.2 Magnetic Reconnection Rates

We now evaluate our two measures of energy release. The rate of flux annihilation at the neutral point is

$$\frac{\partial \psi}{\partial t} = \eta J_0 \sim \eta,$$

while the Ohmic dissipation rate scales as

$$W_\eta = \eta \int_S J^2 \mathrm{d}S \approx \eta J_0^2 L l \sim \eta.$$

Obviously the stalling tendency makes both measures slow.

4.5 Stalling of Reconnection

4.5.1 A Sample Simulation

With another sample run, the stalling phenomenon is now examined more closely. Figure 4.7 presents successive plots of ψ (top panel) and $\mathbf{u}$ (bottom panel) in Model A for $\eta = 1 \times 10^{-4}$ and $\beta = 10$ which is already known to stall. Figure 4.7a shows the system at 1.0 Alfvén-times while each successive plot is evaluated after a further 1.0 Alfvén-times have elapsed. The 'stalling' graphs of Figure 4.7 are now compared with the 'non-stalling' graphs of Figure 4.2.

One immediately recognises that the evolution of the magnetic field shown in Figure 4.7 differs markedly from that depicted in Figure 4.2. Instead of freely coalescing, the magnetic island pairings become highly compressed together. Therefore magnetic field lines reaching the neutral point are not being reconnected rapidly enough. It is clear that the localisation of the magnetic field is being obstructed.

The latter figures show that plasma is being prevented from approaching the neutral point. Here the 'unwanted' plasma forms two reversed eddies which eventually supersede the initial eddy. Our magnetic island pairings then start moving apart *before* all the field lines have reconnected. Hence the reconnection process has not succeeded in liberating the bulk of the perturbation energy.

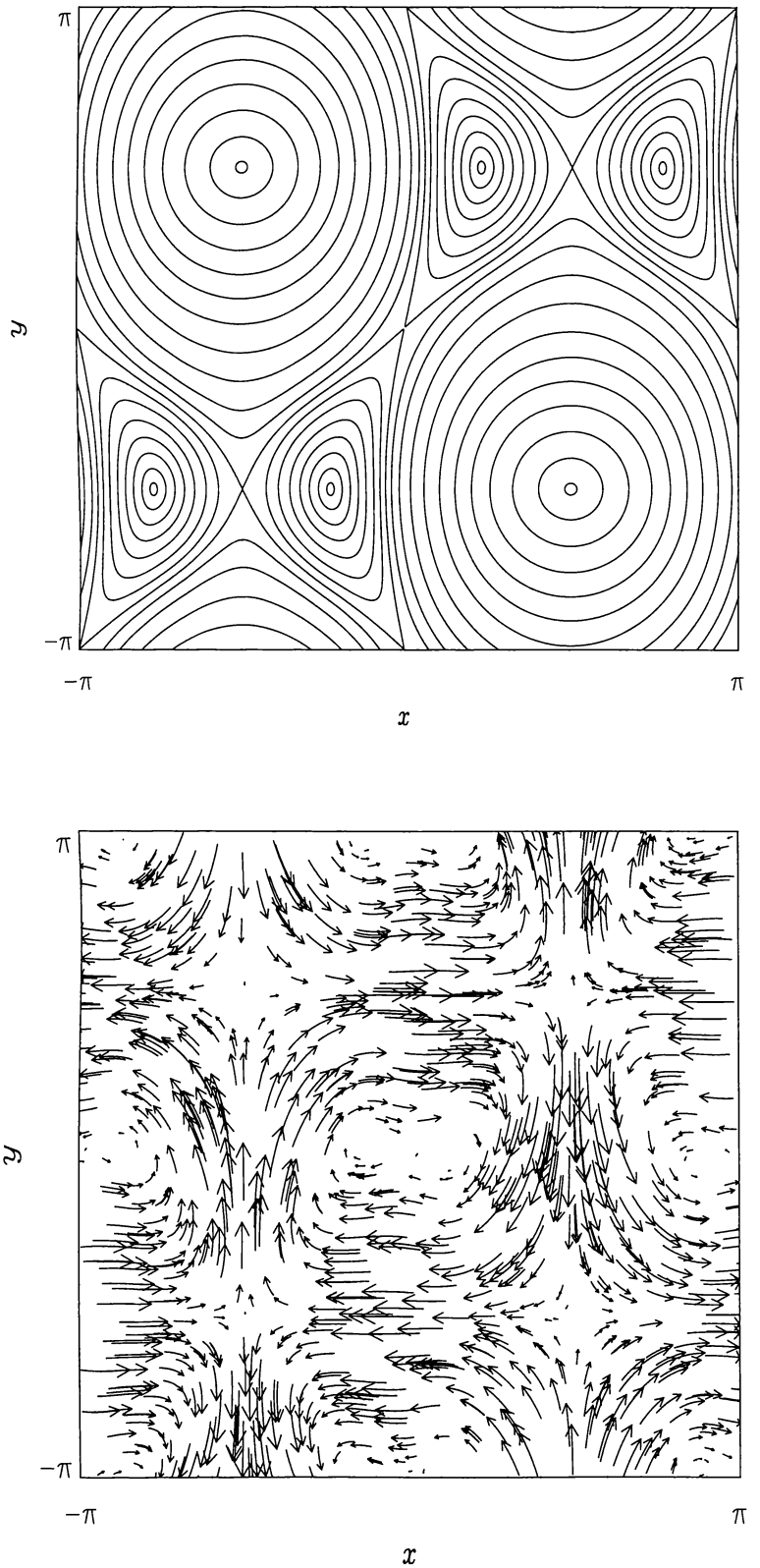


Figure 4.7a. Contour plot of ψ (top) and vector plot of $\mathbf{u}$ (bottom) for $\eta = 5 \times 10^{-4}, \beta = 10$ at $t = 1.0$ for Model A.

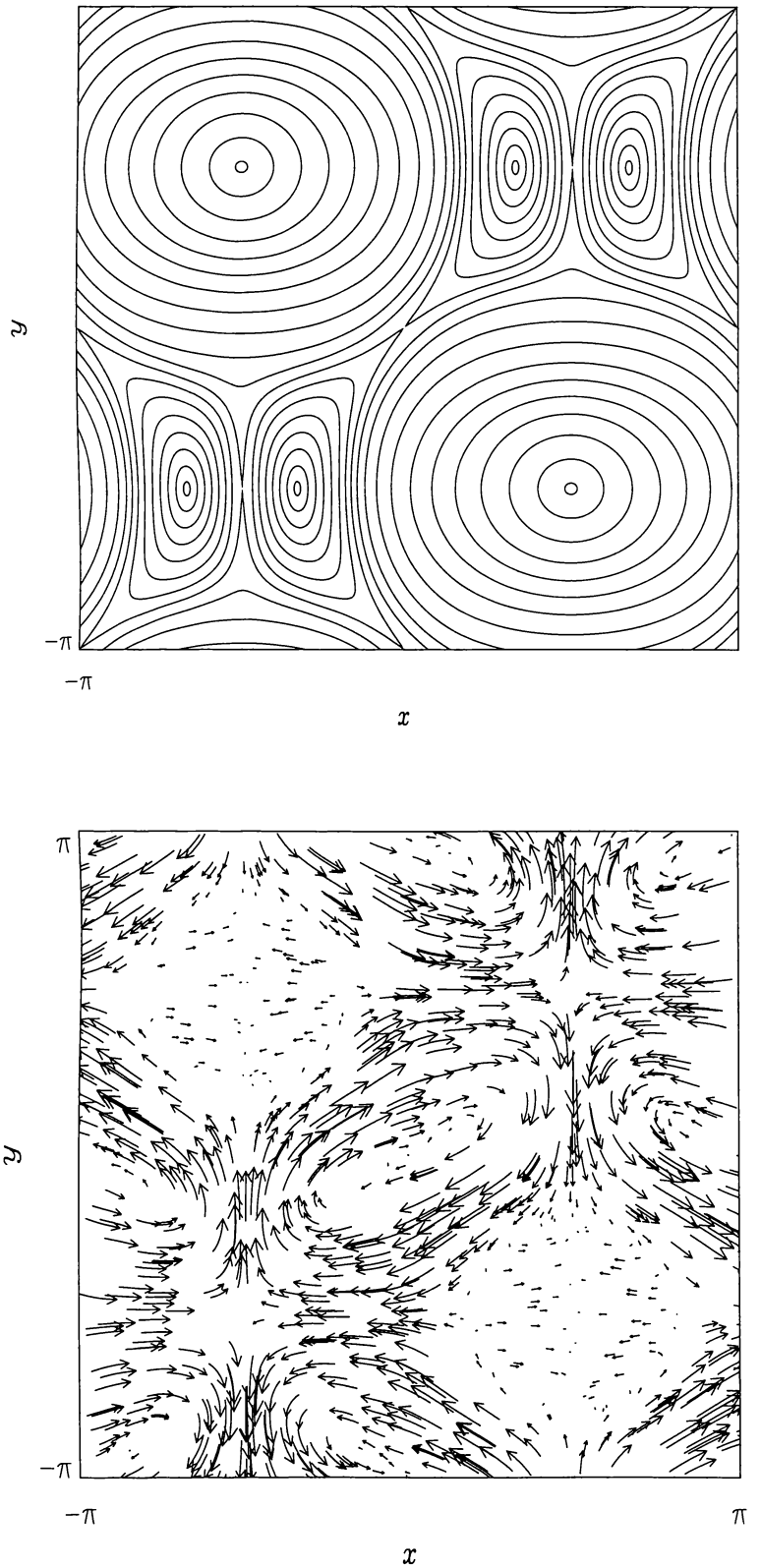


Figure 4.7b. Contour plot of ψ (top) and vector plot of $\mathbf{u}$ (bottom) for $\eta = 5 \times 10^{-4}, \beta = 10$ at $t = 2.0$ for Model A.

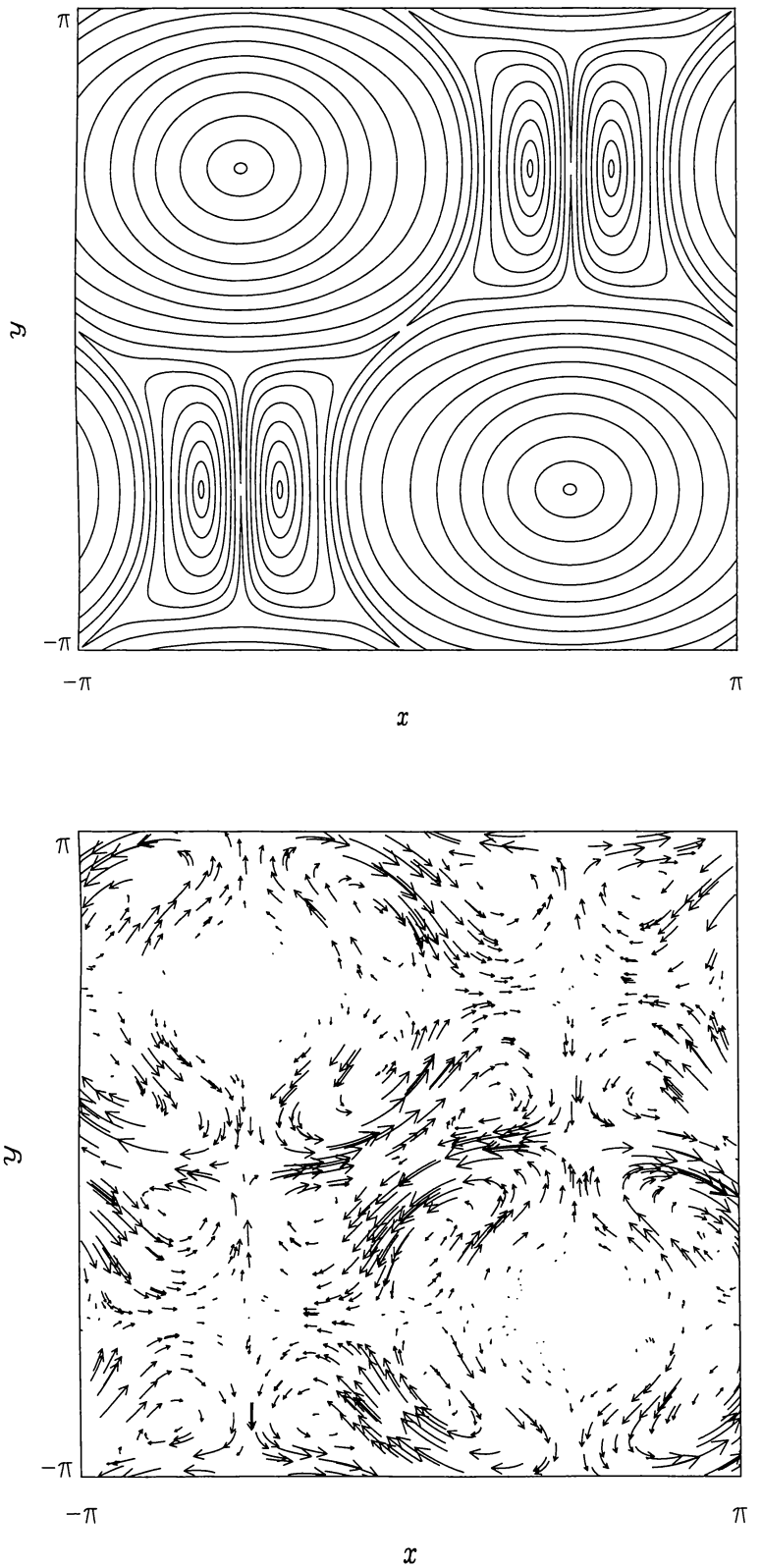


Figure 4.7c. Contour plot of ψ (top) and vector plot of $\mathbf{u}$ (bottom) for $\eta = 5 \times 10^{-4}, \beta = 10$ at $t = 3.0$ for Model A.

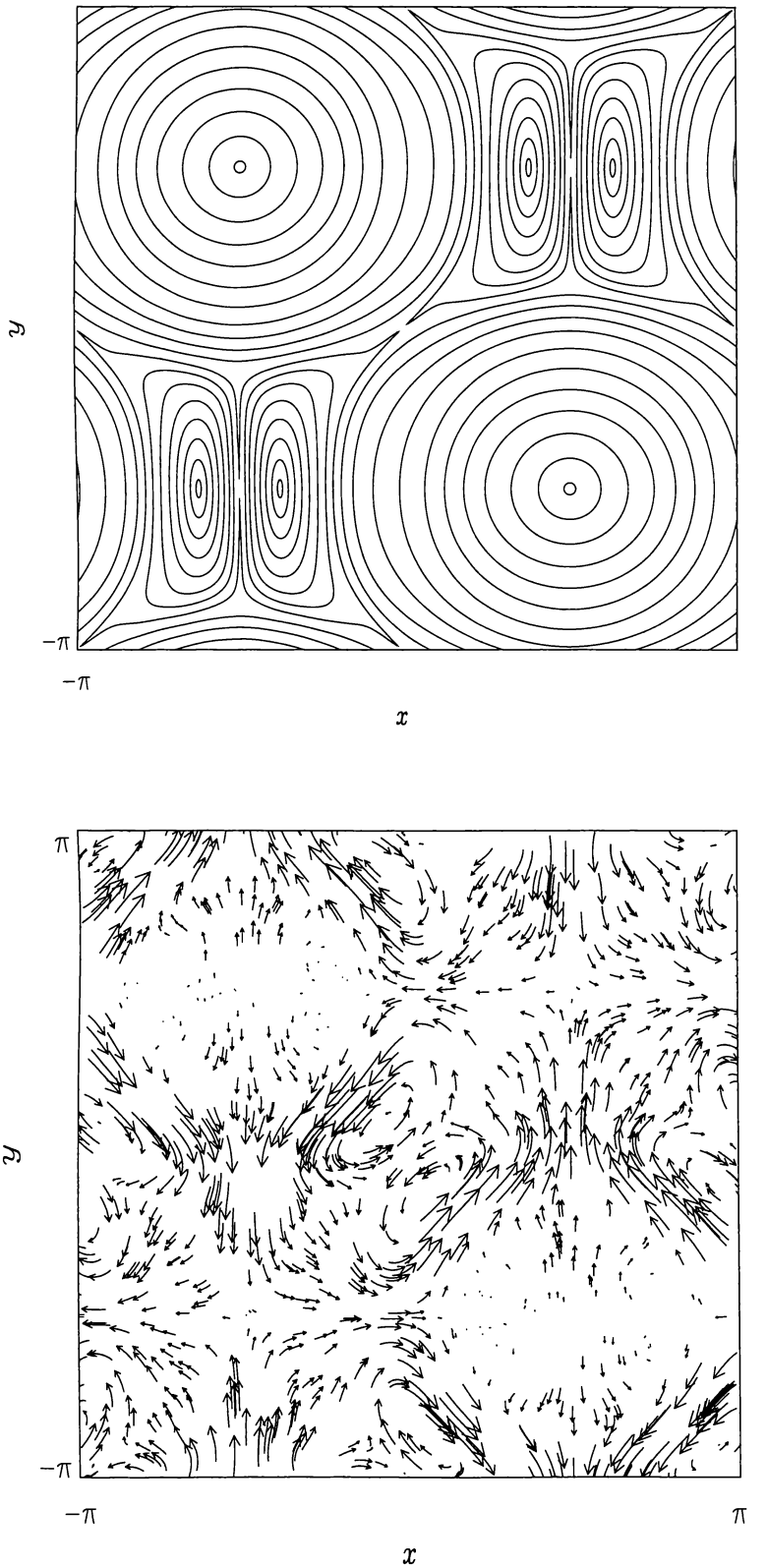


Figure 4.7d. Contour plot of ψ (top) and vector plot of $\mathbf{u}$ (bottom) for $\eta = 5 \times 10^{-4}, \beta = 10$ at $t = 4.0$ for Model A.

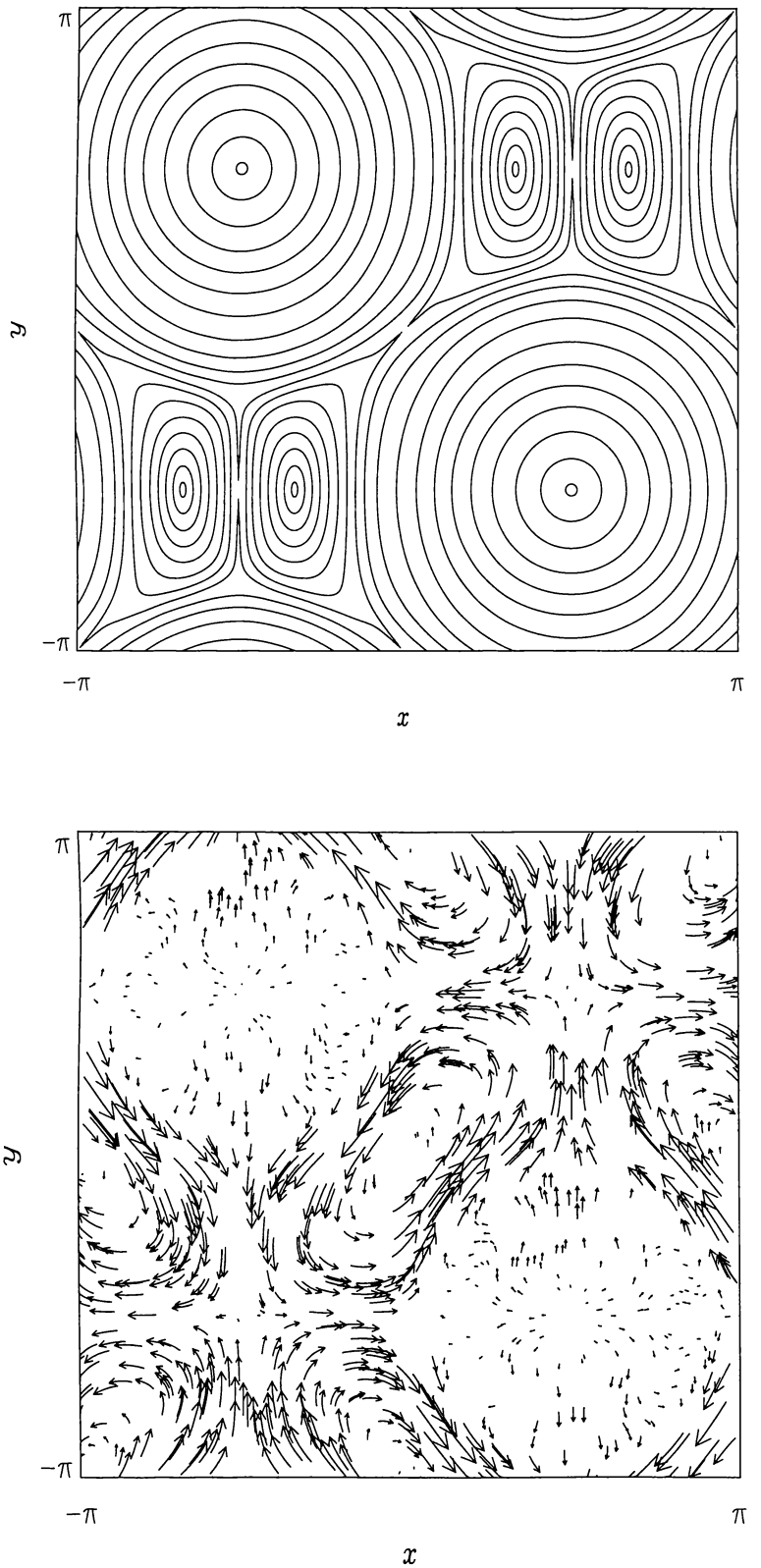


Figure 4.7e. Contour plot of ψ (top) and vector plot of $\mathbf{u}$ (bottom) for $\eta = 1 \times 10^{-4}, \beta = 10$ at $t = 5.0$ for Model A.

4.5.2 The Stalling Mechanism

We first note that our diagnostic scalings show that the stalling of B_{sheet} is insensitive to β. This naturally suggests that the maximum value that B_{sheet} can attain is 'predetermined' each model. We point out that Biskamp & Welter (1980) anticipated this saturation but could not demonstrate it from their simulations.

Now we examine the individual terms on the right-hand side of (4.6). These terms obviously dictate the motion of plasma approaching the neutral point. Thus we can establish why the localisation of the magnetic field saturates. Here we focus our attention on Model A with $\beta = 10$ but mention that similar trends held for Model B and also $\beta = 1$.

Three forcing terms are now of interest, namely

(i) the planar Lorentz force : $-\nabla^2\psi\,\psi_x$,

(ii) the force due to b : $-bb_x$,

(iii) the plasma pressure force : $-\beta\gamma\rho^{\gamma-1}\rho_x$.

We return to our two sample simulations (see Figures 4.2 and 4.7) and proceed to evaluate these forces. Again the horizontal axes have been translated so that the neutral point coincides with $x = 0$. A dotted line has been used to illustrate the edge of the current sheet and a negative value of a given term implies that force is directed inward. It is also noted that the 'spikiness' of these graphs simply reflects the coarse resolution.

We mention here that the evolution of each forcing term was also examined. However this analysis simply reaffirmed the findings presented below and has therefore been omitted.

The planar Lorentz force is plotted in Figure 4.8. We see that the Lorentz force outside the sheet acts against the localisation for both cases. This force reverses on entering the sheet and plasma is subsequently driven inward. Hence the planar Lorentz force is driving the reconnection of field lines.

The force resulting from b is depicted in Figure 4.9. Clearly the perpendicular component acts against the plasma inflow so therefore opposes the localisation. However, as both graphs are qualitatively similar, this force does not cause the localisation to stall. This must be true as reconnection also stalls in Model B which has no b.

The plasma pressure force is shown in Figure 4.10. Plasma outside the current sheet is being driven inward in both cases. Meanwhile the plasma pressure inside the sheet acts against the plasma flow for $\eta = 1 \times 10^{-4}$ but not for $\eta = 5 \times 10^{-2}$. It is obvious that the pressure force stalls the localisation of the magnetic field as η is reduced.

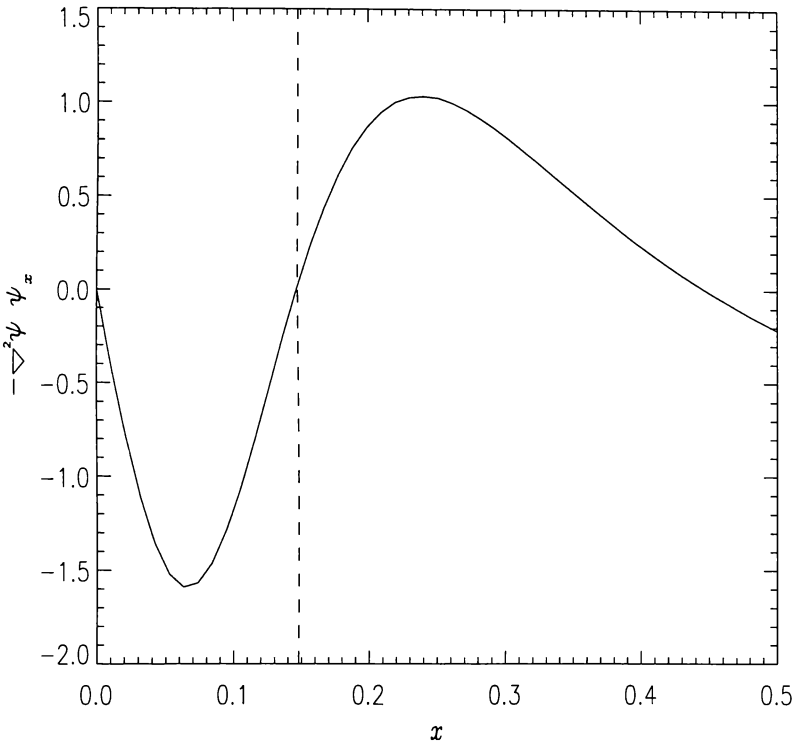


Figure 4.8a. Profile of $-\nabla^2\psi\,\psi_x$ versus x where $\eta = 5 \times 10^{-2}, \beta = 10$ for Model A. Positive values imply that the force is directed to the right.

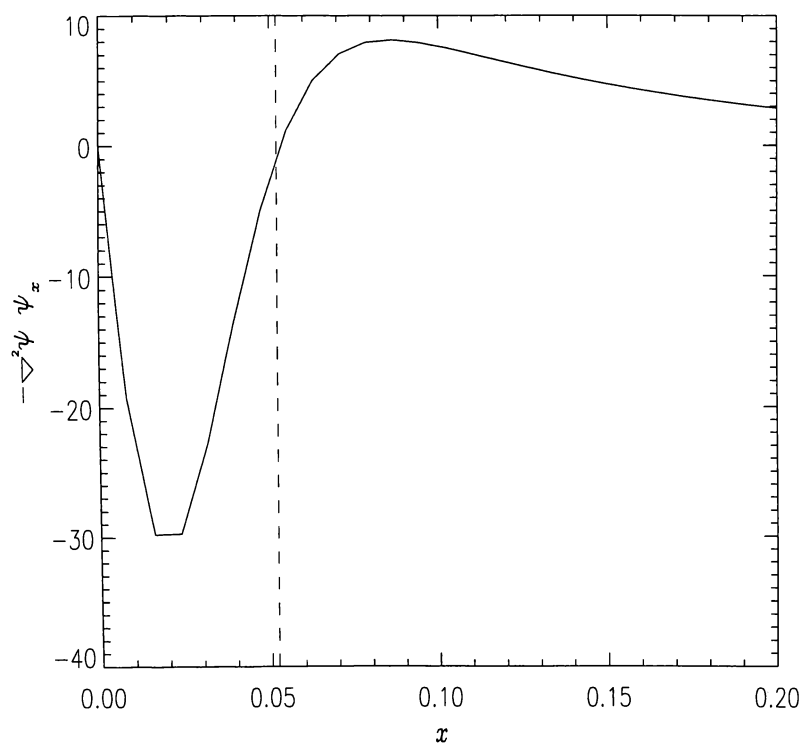


Figure 4.8b. Profile of $-\nabla^2\psi\,\psi_x$ versus x where $\eta = 1 \times 10^{-4}, \beta = 10$ for Model A. Positive values imply that the force is directed to the right.

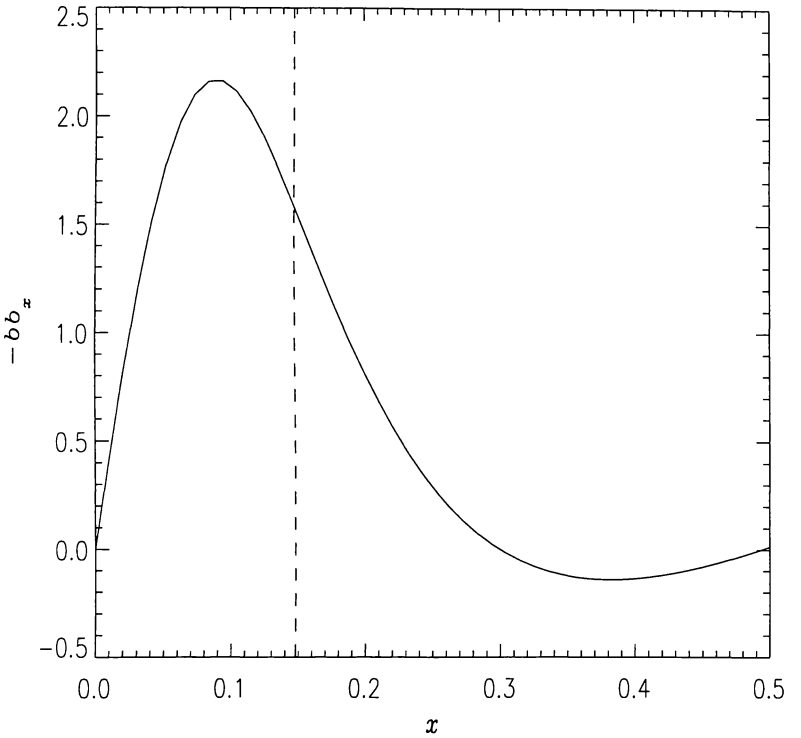


Figure 4.9a. Profile of $-bb_x$ versus x where $\eta = 5 \times 10^{-2}, \beta = 10$ for Model A. Positive values imply that the force is directed to the right.

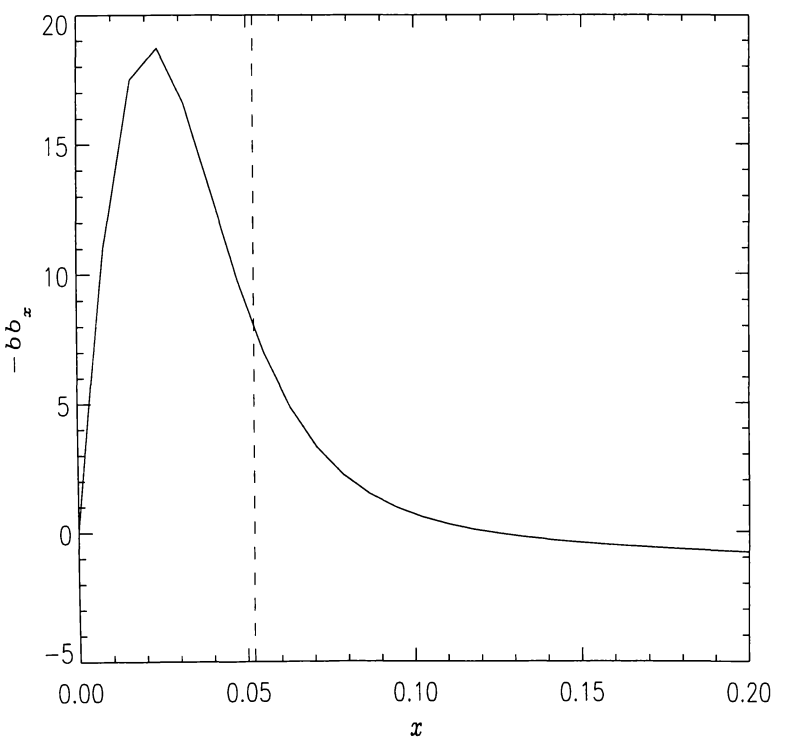


Figure 4.9b. Profile of $-bb_x$ versus x where $\eta = 1 \times 10^{-4}, \beta = 10$ for Model A. Positive values imply that the force is directed to the right.

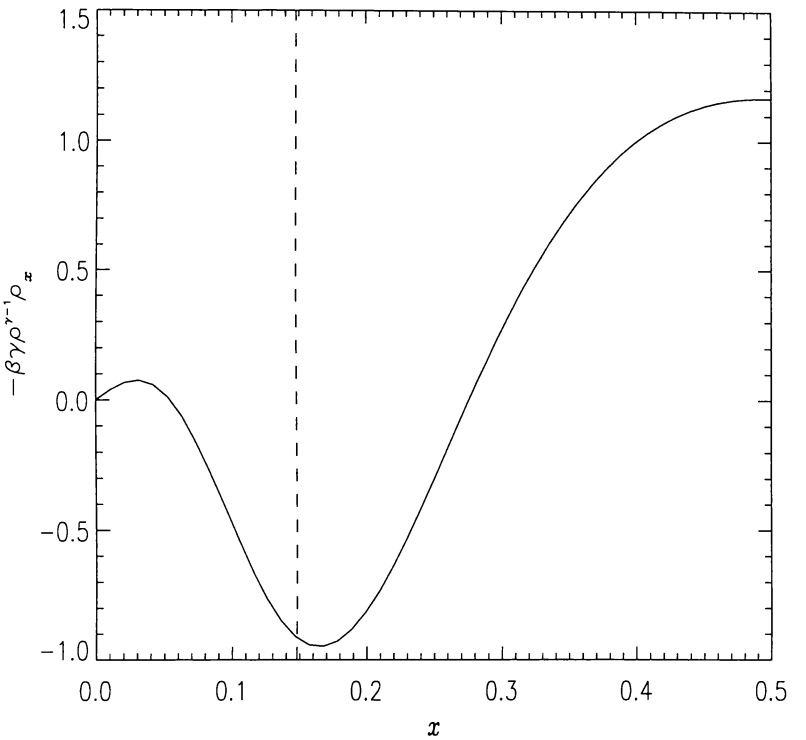


Figure 4.10a. Profile of $-\beta\gamma\rho^{\gamma-1}\rho_x$ versus x where $\eta = 5 \times 10^{-2}, \beta = 10$ for Model A. Positive values imply that the force is directed to the right.

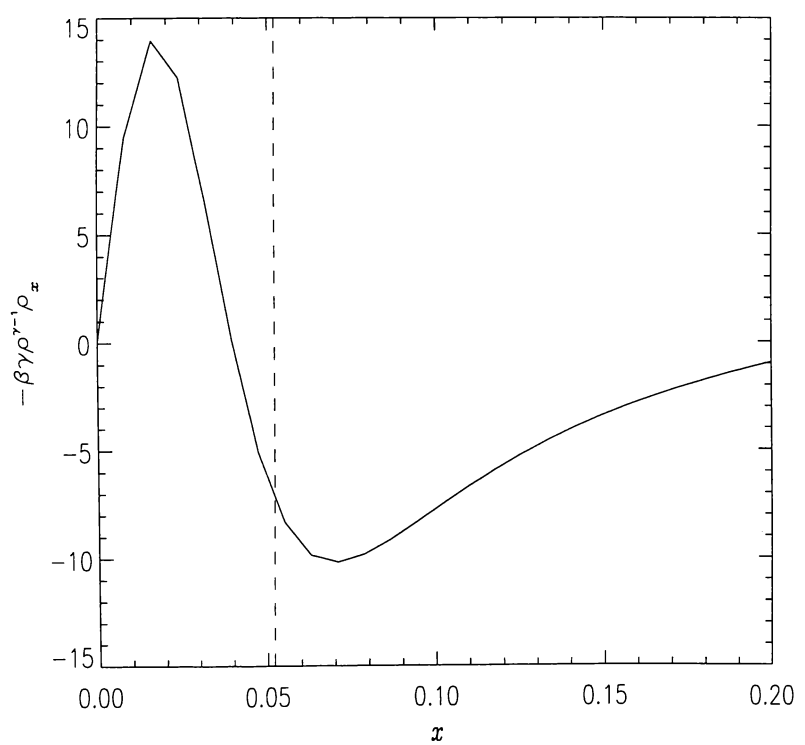


Figure 4.10b. Profile of $-\beta\gamma\rho^{\gamma-1}\rho_x$ versus x where $\eta = 1 \times 10^{-4}, \beta = 10$ for Model A. Positive values imply that the force is directed to the right.

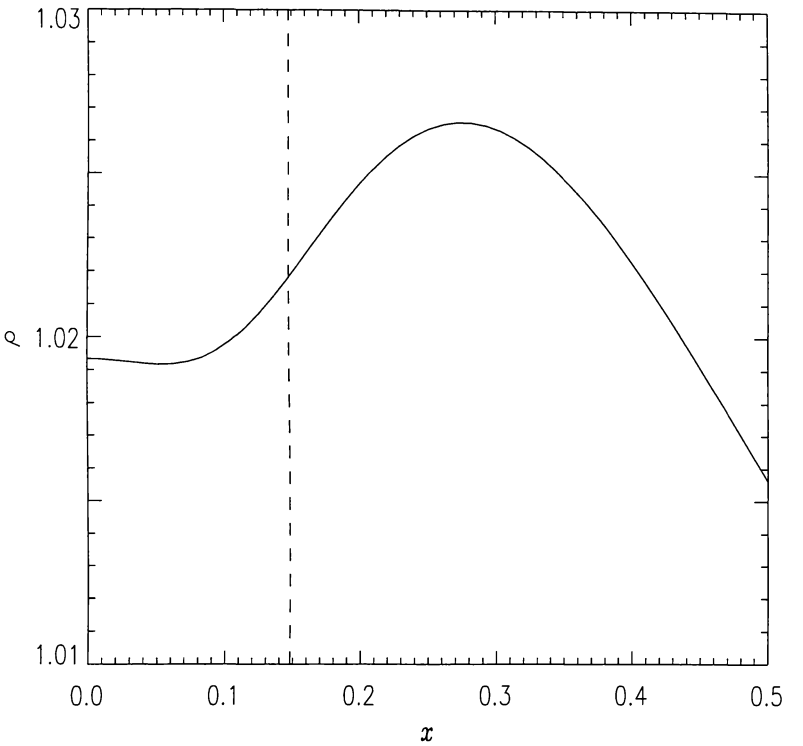


Figure 4.11a. Profile of ρ versus x where $\eta = 5 \times 10^{-2}, \beta = 10$ for Model A. Positive values imply that the force is directed to the right.

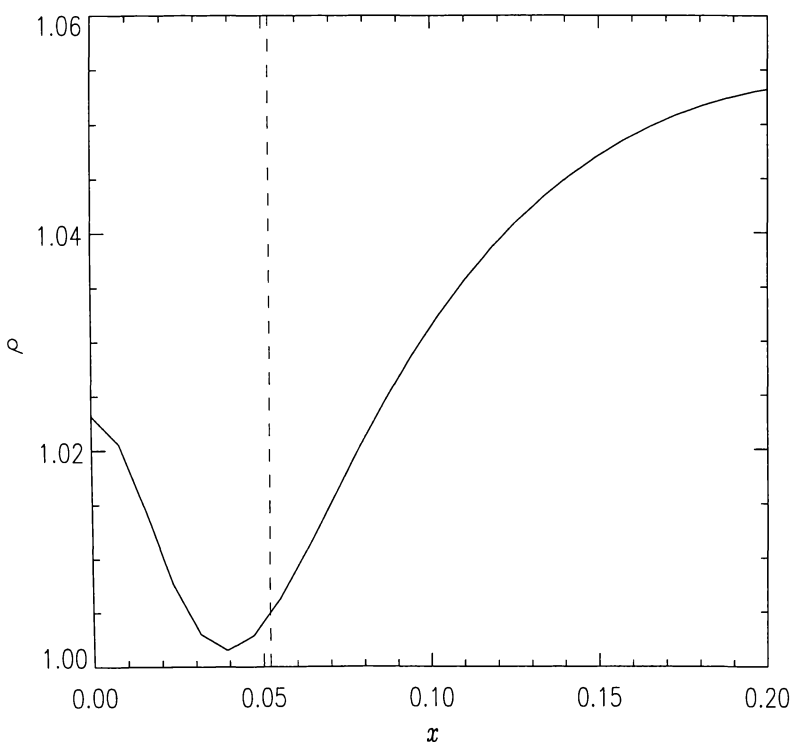


Figure 4.11b. Profile of ρ versus x where $\eta = 1 \times 10^{-4}, \beta = 10$ for Model A. Positive values imply that the force is directed to the right.

Figure 4.11 plots the plasma density. This graph shows that the 'back-pressure' observed in Figure 4.10 is due to a build-up in ρ at the neutral point. Another interesting feature is the density trough in front of the current sheet for the $\eta = 1 \times 10^{-4}$ case.

We now propose a qualitative theory to explain the stalling of reconnection. The governing equations are highly non-linear so isolating the actual cause of stalling from its consequences is not a straight forward exercise.

Our results show that the plasma pressure acts against the localisation of the magnetic field as η declines. However we also found that the pile-up of the magnetic field entering the sheet saturates. Therefore the Lorentz force that drives reconnection reaches a fixed value while the plasma pressure inside the sheet still increases as η is reduced. We can therefore conclude that reconnection stalls as the magnetic field entering the sheet, B_{sheet}, cannot surpass the background field, B_0 say, which is order unity.

An important point is that a back-pressure should not be regarded as a necessary condition for stalling. Our exact solutions in Chapters 6 and 7 will demonstrate that reconnection need not stall if plasma pressures are building up inside the current sheet.

4.6 Summary

Two models of magnetic reconnection have been studied. Both models are periodic so the problematic task of prescribing boundary conditions has been alleviated. The periodicity also allows the computational domain to be reduced considerably which thereby allows the simulation of extremely small η. Our results clearly show that reconnection stalls for sufficiently small values of η. Hence we confirmed the possibility of stalling suggested by the DeLuca & Craig (1992) simulations.

We demonstrated that a build-up of plasma pressure inside the current sheet occurred. Here this force was induced by a density accumulation at the neutral point. We also found that the pile-up of the magnetic field saturated (seemingly independent of β) as plasma resistivity was reduced. This saturation is consistent with the 'prediction' of stalling by Biskamp & Welter (1980) and the hint of stalling perceived by DeLuca & Craig (1992).

Our numerical results show that the Lorentz force driving the localisation of the magnetic field was eventually overwhelmed by the plasma pressure within the current sheet. We therefore conclude that saturation of the magnetic field entering the sheet, B_{sheet}, caused the reconnection rate to stall.

CHAPTER 5

Sub-Alfvénic Steady-State Solutions

5.1 Introduction

This chapter tackles the problem of steady-state magnetic reconnection assuming an incompressible plasma. Analytical progress is gained by making the further approximation that plasma velocities are sub-Alfvénic. Namely we assume that $|v| \ll |v_A|$ where v is the plasma speed and v_A is a characteristic Alfvén speed for the corona. Since typical values of v_A are $O(10^6)$ m/s, we emphasise that flow speeds can still be large with respect to the sound speed.

A strength of our sub-Alfvénic approach is that it advances the Forbes & Priest (1986) analysis discussed in Chapter 3. The resistive term in the governing equations is retained which allows the reconnection system to be treated more self-consistently. We also remark that Petschek (1964) also assumes a sub-Alfvénic flow in the outer regions. Work presented in this chapter is published in Craig & Henton (1994).

In Section 5.2 we simplify the steady-state MHD equations for an incompressible plasma into a compact form. Section 5.3 derives linear solutions and then a particular solution is presented. Next we derive non-linear solutions in Section 5.4 and another particular solution is given. Section 5.5 then gives a discussion of our findings. We give a summary of this chapter in Section 5.6.

5.2 Preliminaries

5.2.1 Formulating the Equations

The steady-state MHD equations were given in Chapter 2. For an incompressible plasma the equations are

$$\mathbf{v}.\nabla\mathbf{v} = (\nabla \times \mathbf{B}) \times \mathbf{B} - \nabla p, \tag{5.1}$$

$$\mathbf{E} + \mathbf{v} \times \mathbf{B} = \eta(\nabla \times \mathbf{B}), \tag{5.2}$$

$$\nabla.\mathbf{B} = 0, \tag{5.3}$$

$$\nabla.\mathbf{v} = 0, \tag{5.4}$$

where we have set $\rho = 1$ and

$$\frac{\partial \mathbf{B}}{\partial t} = -\nabla \times \mathbf{E}, \tag{5.5}$$

gives the relationship between the magnetic field and electric field.

We let the governing equations be two-dimensional and take x and y as the independent variables. It is now possible to make further simplifications of (5.1) to (5.4).

In steady-state it then follows from (5.5) that

$$\mathbf{E} = (0, 0, E),$$

where E is a constant.

Equation (5.3) allows the introduction of a flux function $\psi(x, y)$ for the magnetic field

$$\mathbf{B} = \nabla \times \psi \hat{\mathbf{z}} = (\psi_y, -\psi_x).$$

Curves given by ψ =constant are magnetic field lines and a field line passing through the neutral point is called a separatrix.

Equation (5.4) allows a stream function $\phi(x, y)$ to be introduced for the velocity field

$$\mathbf{v} = \nabla \times \phi \hat{\mathbf{z}} = (\phi_y, -\phi_x).$$

The curves given by ϕ =constant define the streamlines of the plasma flow.

We also have that

$$\mathbf{J} = \nabla \times \mathbf{B} = -\nabla^2 \psi \hat{\mathbf{z}},$$

and

$$\omega = \nabla \times \mathbf{v} = -\nabla^2 \phi \hat{\mathbf{z}},$$

where $\mathbf{J}$ is current density and ω is vorticity.

Taking the curl of (5.1) gives

$$(\nabla^2 \phi)_x \phi_y - (\nabla^2 \phi)_y \phi_x = (\nabla^2 \psi)_x \psi_y - (\nabla^2 \psi)_y \psi_x, \tag{5.6}$$

while (5.2) reduces to

$$E + \psi_x \phi_y - \psi_y \phi_x = \eta \nabla^2 \psi. \tag{5.7}$$

We point out that the vector equations (5.1) and (5.2) have now been reduced to scalar equations.

On adopting the notation

$$[f, g] = f_x g_y - f_y g_x, \tag{5.8}$$

we can express (5.6) and (5.7) as

$$[\nabla^2\phi, \phi] = [\nabla^2\psi, \psi], \tag{5.9}$$

$$E + [\psi, \phi] = \eta\nabla^2\psi, \tag{5.10}$$

and restate that E is constant.

The traditional symmetries detailed in Chapter 2 now become

$$\psi_x = 0, \qquad \phi_y = 0, \qquad \text{along } x = 0,$$

$$\psi_y = 0, \qquad \phi_x = 0, \qquad \text{along } y = 0,$$

and we note that the neutral point is both a null in the magnetic field and a stagnation-point of the plasma flow.

Exact solutions of two-dimensional reconnection have not appeared in the literature. In our view, the non-linear combination of high-order derivatives in (5.9) has been the major obstacle. Hence we shall introduce an approximation to simplify this troublesome equation.

5.2.2 The Bracket Notation

The bracketed representation of the two-dimensional MHD equations will be our launching point for establishing solutions. By taking suitable trial forms for ϕ and ψ, equations (5.9) and (5.10) can be simplified by exploiting algebraic properties listed below.

It follows from (5.8) that if u, v and w are any functions then

$$[u, v] = -[v, u],$$

$$[u + v, w] = [u, w] + [v, w],$$

$$[uv, w] = u[v, w] + v[u, w],$$

$$[u(p), v(q)] = u'(p)v'(q)\,[p, q],$$

where dashes signify derivatives with respect to the stated variable.

One also has that

$$[u, v] = 0 \quad \Leftrightarrow \quad u = f(v),$$

where f is an arbitrary function. This result means that u is constant along the contours of v and vice versa. We point out that f can be constant or even zero.

5.3 Linear Solutions

5.3.1 Derivation

We now derive linear solutions from the incompressible MHD equations. The analysis presented here first appeared in Craig & Rickard (1994) for the linearised case. In the next section we shall extend this study into a non-linear regime. Much of the analysis presented here can be carried over into the next section.

We now linearise (5.9) and (5.10) then examine first-order perturbations (ϕ_1, ψ_1) about a known equilibrium solution (ϕ_0, ψ_0). One could imagine this situation results from slightly disturbing the zeroth-order solution then allowing a new steady-state configuration to be attained. If the perturbation terms remain acceptably small, linear solutions should then provide reliable approximations of the exact solution.

A suitable zeroth-order solution is given by

$$E_0 = 0,$$

$$p_0 = \text{constant},$$

$$\phi_0 = 0,$$

$$\psi_0 = h_0(x, y),$$

where h_0 is any potential function that satisfies the traditional symmetries in Chapter 2. This equilibrium solution corresponds to a current-free magnetic field in a stationary plasma. Obviously the vorticity and current distributions will now depend only on the perturbed variables ϕ_1 and ψ_1 respectively.

By exploiting the bracket properties listed earlier, equations (5.9) and (5.10) become

$$\nabla^2 \psi_1 = f(\psi_0), \tag{5.11}$$

$$E_1 + [\psi_0, \phi_1] = \eta \nabla^2 \psi_1, \tag{5.12}$$

where E_1 is the first-order electric field and f is an *arbitrary* function. We remark that the linearisation by Priest & Forbes (1986) (see Chapter 3) also admitted an arbitrary function.

The linearised form of (5.1) can be written as

$$\nabla^2 \psi_1 \nabla \psi_0 + \nabla p = 0,$$

which implies that

$$f(\psi_0) = -p'(\psi_0),$$

where p is the plasma pressure (first-order) while (5.12) implies that $p'(0) = -\frac{E_1}{\eta}$.

The flux function ψ_1 can be determined *entirely* from (5.11). Equation (5.11) is a Poisson equation which can be solved once p and outer boundary conditions are prescribed. In particular a linear combination of ψ_1 and its normal derivative is needed.

To determine ψ_1 we use a finite-difference scheme to model

$$\frac{\partial \psi_1}{\partial t} = p'(\psi_0) + \nabla^2 \psi_1,$$

until a steady-state is reached. This method gives us the freedom to choose any combination of ψ_1 and normal derivative of ψ_1 along the outer boundary and any form for p.

Now ϕ_1 can be evaluated via the method of characteristics. First we rewrite (5.12) as

$$(\phi_1)_x(\psi_0)_y - (\phi_1)_y(\psi_0)_x = [E_1 + \eta p'(\psi_0)],$$

which shows that the characteristics ξ are given by

$$\xi = \psi_0.$$

We therefore introduce the variables

$$\xi = \psi_0, \qquad \chi = x,$$

and express (5.12) as

$$(\phi_1)_\chi(\psi_0)_y = [E_1 + \eta p'(\psi_0)],$$

where $(\psi_0)_y$ and $[E_1 + \eta p'(\psi_0)]$ are *known* functions that must now be expressed in terms of χ and ξ.

The solution of (5.12) can be written as

$$\phi_1 = [E_1 + \eta p'(\psi_0)] \int \frac{\mathrm{d}\chi}{(\psi_0)_y} + \gamma(\xi),$$

where γ is an arbitrary function and the characteristic curves are given by ξ =constant. This integral is evaluated over χ while keeping ξ constant.

It follows that

$$\nabla \times \gamma(\xi) = \gamma'(\xi)\nabla \times \xi = \gamma'(\psi_0)\nabla \times \psi_0,$$

so the γ term gives rise to flow along the contours of ψ_0.

Plasma cannot cross the inner boundaries so we must assign $\phi_1 = 0$ on $x = 0$ and $y = 0$. As the inner boundaries are not characteristics, these boundary conditions mean that the solution for ϕ_1 is now fully determined. Thus outer boundary conditions are not required.

In general the solution for ϕ_1 cannot be calculated analytically. However a numerical solution can easily be constructed using the Wendroff's implicit method outlined in Smith (1978). This method allows ϕ_1 at any grid point to be determined (recursively) from the values of ϕ_1 along the inner boundaries.

We now point out the important properties of the linear solutions. From (5.11) we have

(i) the current and pressure are constant along the contours of ψ_0,

(ii) the ridges of peak current overlie the separatrices of ψ_0. Hence the current sheet is not a singular 'spike' but extends from the neutral point to the outer boundary.

From (5.12) we have

(iii) ϕ_1=constant along the separatrices of ψ_0. This implies that plasma cannot flow across the separatrices because they are streamlines,

(iv) ϕ_1 is even across the separatrices of ψ_0. Therefore plasma cannot flow along the separatrices.

In the vicinity of the neutral point we have

$$p \approx p_0 - \frac{E_1}{\eta}\psi_0,$$

where p_0 denotes a constant background pressure. This expression indicates that plasma pressure is a local saddle-point.

5.3.2 A Particular Solution

We now give a particular linear solution. Our objective here is to demonstrate that linear solutions giving fast energy release can be established.

Our outer boundary condition is

$$\psi_1 = 0,$$

which obviously keeps ψ_1 smaller than ψ_0 along the outer boundaries.

The potential function is

$$\psi_0 = (x^2 - y^2),$$

and is shown in Figure 5.1. This is a simple form that satisfies the inner symmetries.

We finally choose the arbitrary function p so that the current distribution is localised. For analytical convenience we take

$$p(\psi_0) = p_0 - E_1 \tanh(\frac{\psi_0}{\eta}),$$

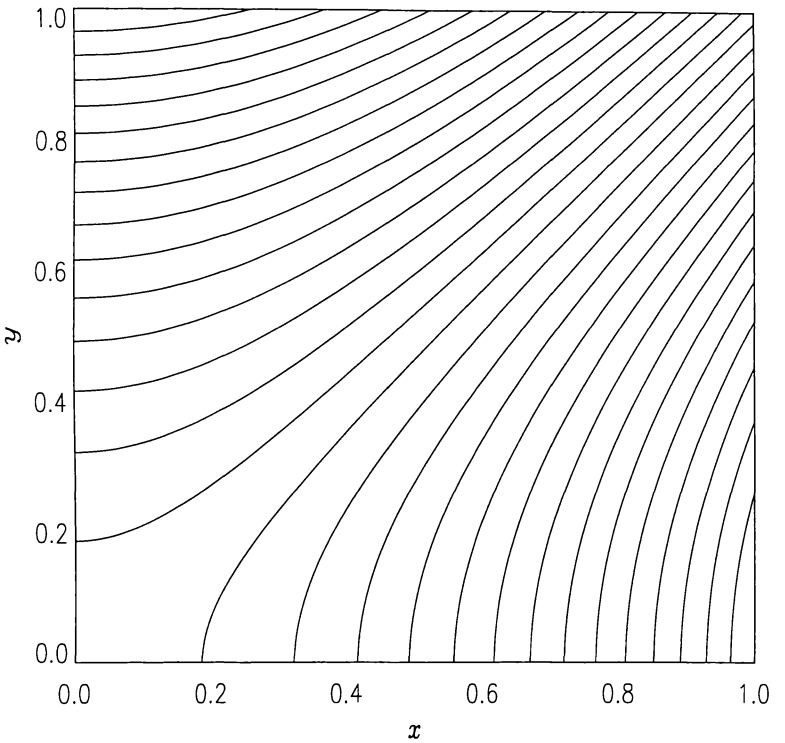


Figure 5.1. Contour plot of ψ_0.

and so we have

$$p'(\psi_0) = -\frac{E_1}{\eta}\mathrm{sech}^2(\frac{\psi_0}{\eta}),$$

where p_0 is the background pressure and $p_0 > E_1$.

This particular choice of ψ_0 allows the integral expression for ϕ_1 to be evaluated analytically. We have

$$\phi_1 = [E_1 + \eta p'(\psi_0)]\sinh^{-1}(\frac{y}{\sqrt{|\psi_0|}}) \qquad x \leq y,$$

$$\phi_1 = [E_1 + \eta p'(\psi_0)]\sinh^{-1}(\frac{x}{\sqrt{|\psi_0|}}) \qquad x \geq y,$$

with p being specified above.

Figure 5.2 presents contour plots of (a) ϕ_1 and (b) $\psi_0 + \psi_1$ and Figure 5.3 gives surface plots of (a) $\nabla^2\psi_1$ and (b) $p - p_0$ for $E_1 = 1, \eta = 0.3$. We emphasise that plasma is travelling inward along the x-axis and outward along the y-axis so there is a shear flow about the separatrices.

We now turn our attention to the energy release. If we allow the flow outside the current sheet to be independent of η then

$$E = E_1 \sim \eta^0,$$

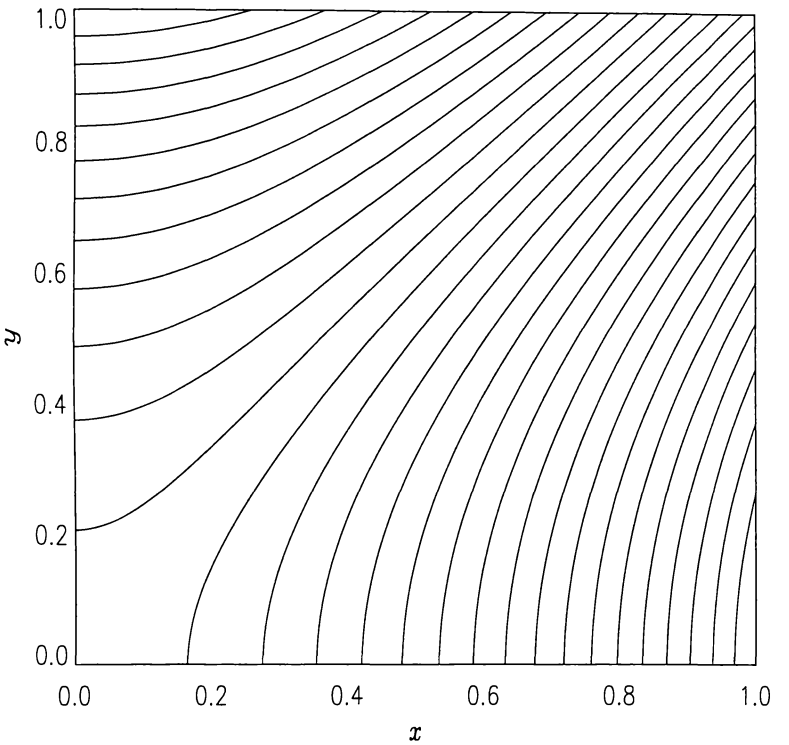


Figure 5.2a. Contour plot of $\psi_0 + \psi_1$ for $E_1 = 1, \eta = 0.3$.

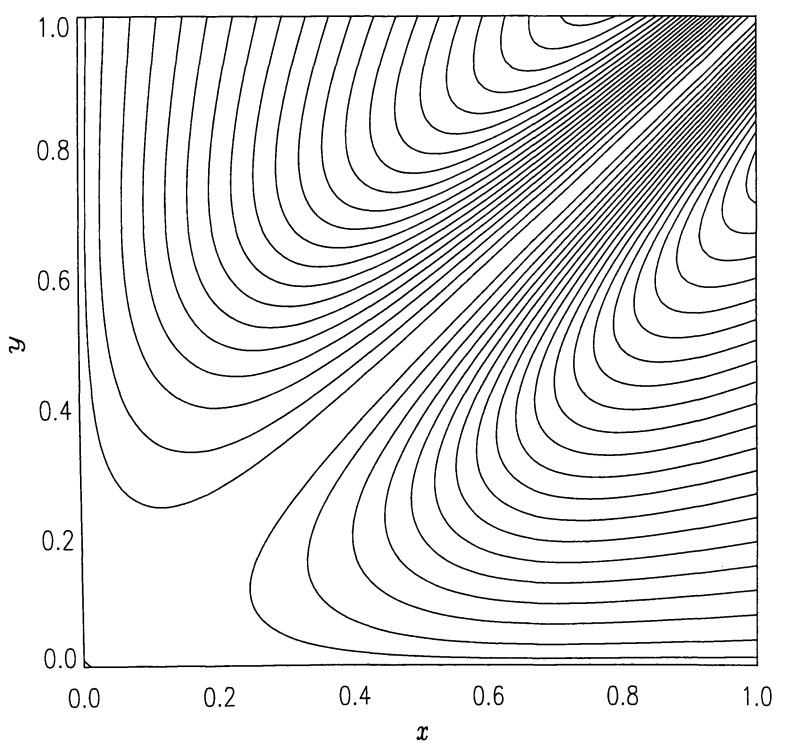


Figure 5.2b. Contour plot of ϕ_1 for $E_1 = 1, \eta = 0.3$.

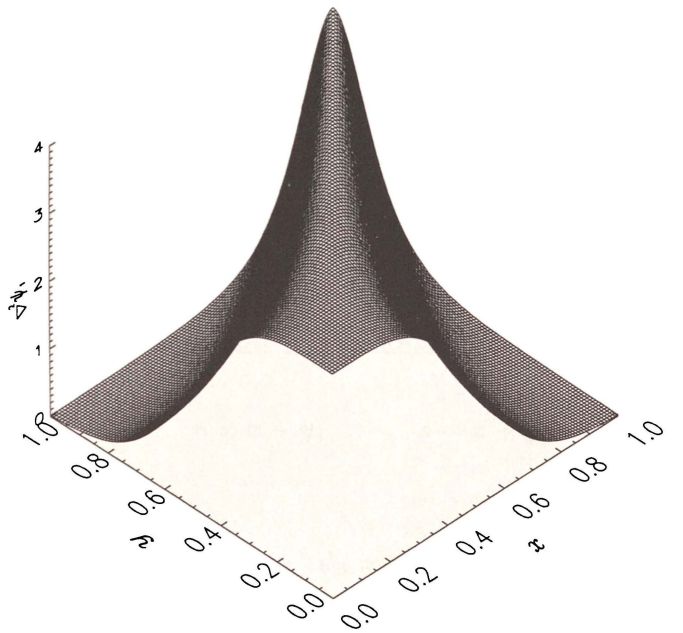


Figure 5.3a. Surface plot of $\nabla^2\psi_1$ for $E_1 = 1, \eta = 0.3$.

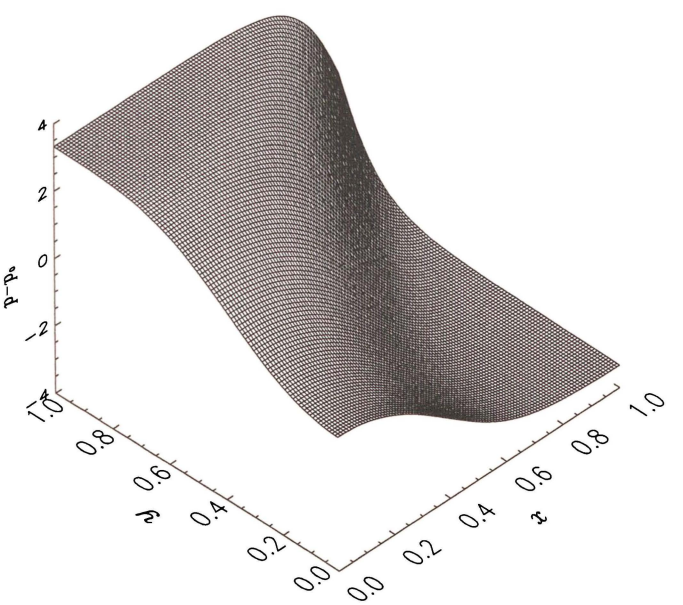


Figure 5.3b. Surface plot of $p - p_0$ for $E_1 = 1, \eta = 0.3$.

and so the rate of flux annihilation scales as

$$\frac{\partial \psi}{\partial t} = E_1 \sim \eta^0,$$

which is defined to be fast.

The Ohmic dissipation rate is

$$W_\eta = \eta \int_S (\nabla^2 \psi_1)^2 \, \mathrm{d}S.$$

To evaluate this measure we introduce the variables

$$r = x - y, \qquad s = x + y,$$

which means

$$\psi_0 = rs,$$

and so

$$W_\eta \approx \frac{(E_1)^2}{\eta} \int_0^1 \int_0^1 \mathrm{sech}^4(\frac{rs}{\eta}) \, \mathrm{d}r \, \mathrm{d}s.$$

Carrying out the first integration gives

$$W_\eta \approx (E_1)^2 \int_0^1 \frac{\tanh(\frac{s}{\eta})}{s} - \frac{\tanh^3(\frac{s}{\eta})}{3s} \, \mathrm{d}s.$$

It then follows that

$$W_\eta \approx (E_1)^2 (a + b \ln(\eta)),$$

where a and b are respective sums of Bernoulli numbers of order unity. Hence the Ohmic dissipation rate is deemed to be fast.

5.4 Non-Linear Solutions

5.4.1 Derivation

The linear solutions in the previous section can be extended by making a less stringent assumption. Namely we only set $\mathbf{v}.\nabla\mathbf{v} = 0$ but do not linearise the magnetic field. We now derive solutions based upon this approximation.

The MHD equations in (5.9) and (5.10) now become

$$\nabla^2 \psi = f(\psi), \tag{5.13}$$

$$E + [\psi, \phi] = \eta \nabla^2 \psi, \tag{5.14}$$

where f is an arbitrary function.

We remark that (5.13) and (5.14) are natural extensions of (5.11) and (5.12). However the critical differences of this approximation are

(i) most of the non-linearity has been preserved – both equations are non-linear.

(ii) more 'information' is retained in the governing equations. The terms $[\nabla^2\psi_1, \psi_1]$ and $[\psi_1, \phi_1]$ lost by linearisation are now retained – only the term $[\nabla\phi_1, \phi_1]$ is lost.

The sub-Alfvénic form of (5.1) is

$$\nabla^2\psi\nabla\psi + \nabla p = 0,$$

which implies that

$$f(\psi) = -p'(\psi),$$

where p is the plasma pressure and (5.14) implies that $p'(0) = -\frac{E}{\eta}$.

The flux function ψ can be determined uniquely from (5.13) once outer boundary conditions have been prescribed. To solve this non-linear equation we employ the finite-difference scheme in the previous section to model

$$\frac{\partial\psi}{\partial t} = p'(\psi) + \nabla^2\psi,$$

until a steady-state is attained.

Again ϕ can be determined by the method of characteristics. We write (5.14) as

$$\phi_x\psi_y - \phi_y\psi_x = [E + \eta p'(\psi)],$$

which implies that the characteristics are given by the contours of ψ. We now introduce the variables

$$\xi = \psi, \qquad \chi = x,$$

and express (5.14) as

$$\phi_\chi\psi_y = [E + \eta p'(\psi)],$$

where ψ_y and $[E + \eta p'(\psi)]$ are *known* functions that must be written in terms of χ and ξ.

We can now express the solution of (5.14) as

$$\phi = [E + \eta p'(\psi)] \int \frac{\mathrm{d}\chi}{\psi_y} + \gamma(\xi),$$

where γ is an arbitrary function and characteristics are given by ξ =constant. Here the integral is evaluated over χ while keeping ξ constant.

Again it follows from our solution for ϕ that

$$\nabla \times \gamma(\xi) = \gamma'(\psi)\nabla \times \psi,$$

so the γ term corresponds to flow along the magnetic field lines.

The traditional symmetries detailed in Chapter 2 imply that $\phi = 0$ along $x = 0$ and $y = 0$. As the inner boundaries are not characteristics, the solution for ϕ is now fully determined and outer boundary conditions are not required. We remark that the numerical method outlined in the previous section can be re-used to calculate ϕ.

The important properties of our non-linear solutions are now detailed. It is pointed out that many properties extend from the linear analysis. We have

(i) the current is constant along the contours of ψ,

(ii) the ridges of peak current overlie the separatrices of ψ,

(iii) plasma cannot flow across the separatrices of ψ because they are streamlines,

(iv) plasma cannot flow along the separatrices of ψ as ϕ is even across them.

Close to the neutral point we have

$$p \approx p_0 - \frac{E}{\eta}\psi,$$

where p_0 denotes a constant background pressure. This result implies that the plasma pressure is a local saddle-point.

A direct consequence of (iii) and (iv) is that reconnection *cannot* occur. Plasma does not cross the separatrices of ψ so magnetic field lines can only be annihilated. This fact implies that $[\psi, \phi] \neq 0$ and $[\nabla^2\psi, \psi] \neq 0$ for exact two-dimensional solutions of reconnection.

5.4.2 A Particular Solution

A particular non-linear solution is now presented. Our primary aim is to demonstrate that non-linear solutions giving fast energy releases can be constructed.

On the outer boundaries we assign

$$\psi = (x^2 - y^2).$$

We must now specify the unknown function. Here we take

$$p(\psi) = p_0 - E\tanh(\frac{\psi}{\eta}),$$

giving

$$p'(\psi) = -\frac{E}{\eta}\mathrm{sech}^2(\frac{\psi}{\eta}),$$

where p_0 is the background pressure and $p_0 > E$. Again this is a simple function that provides a localised current distribution.

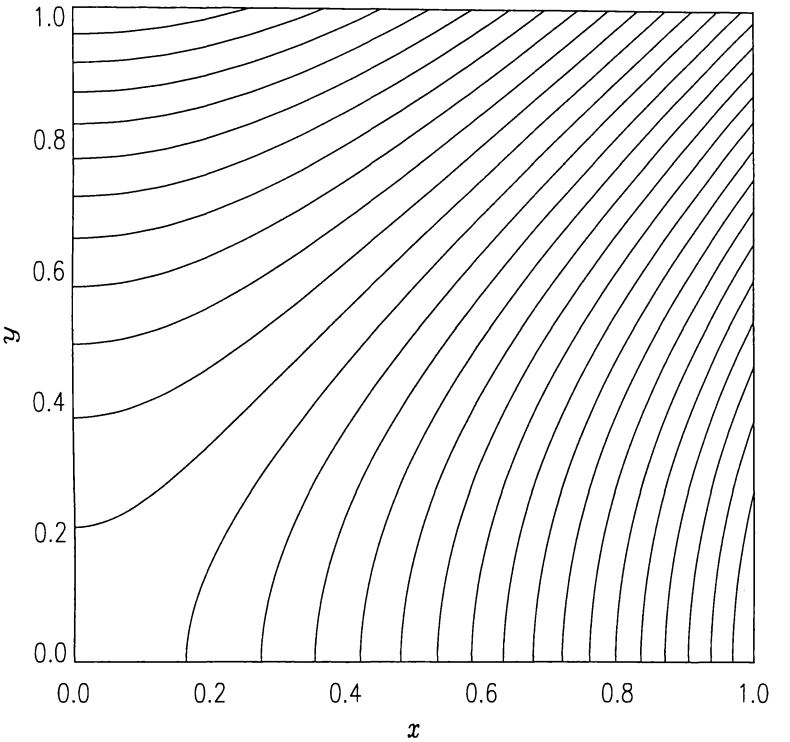


Figure 5.4a. Contour plot of ψ for $E = 0.2, \eta = 0.2$.

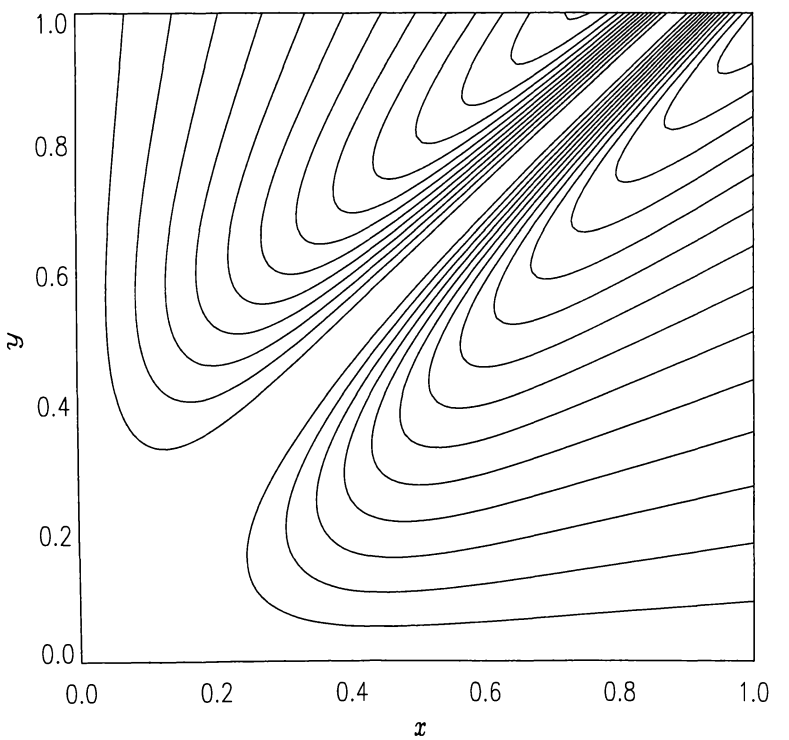


Figure 5.4b. Contour plot of ϕ for $E = 0.2, \eta = 0.2$.

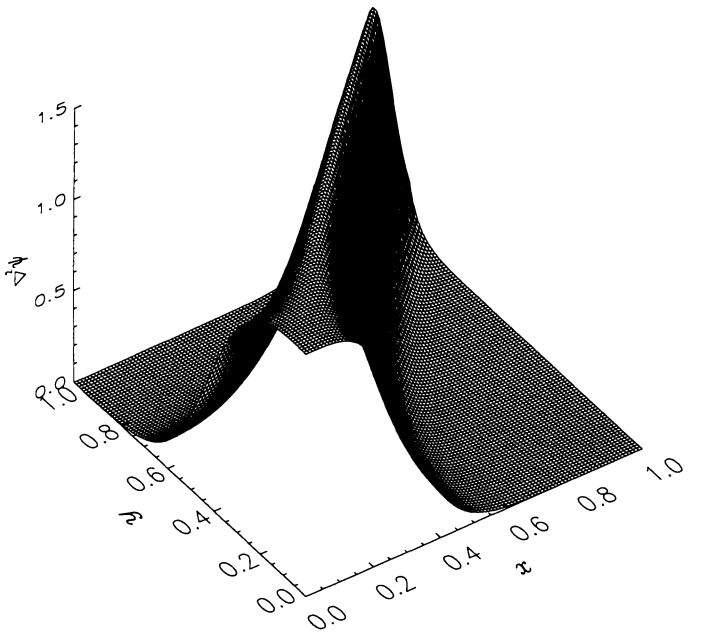


Figure 5.5a. Surface plot of $\nabla^2\psi$ for $E = 0.2, \eta = 0.2$.

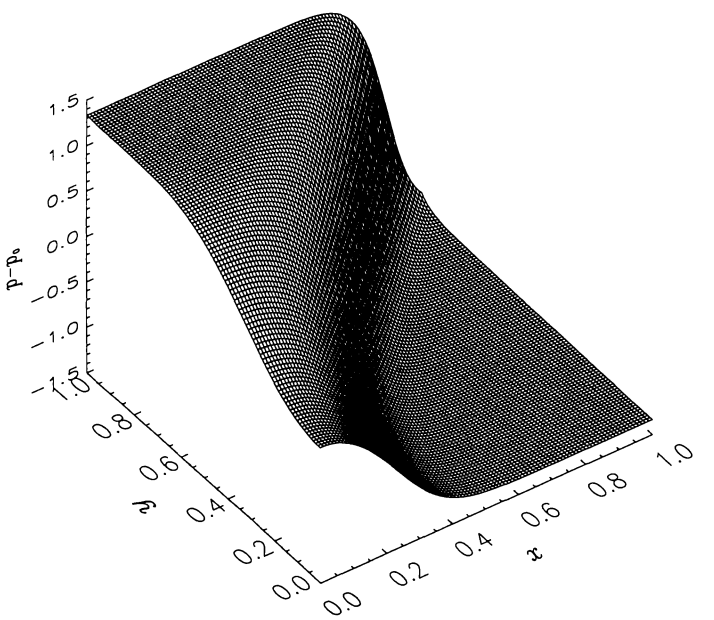


Figure 5.5b. Surface plot of $p - p_0$ for $E = 0.2, \eta = 0.2$.

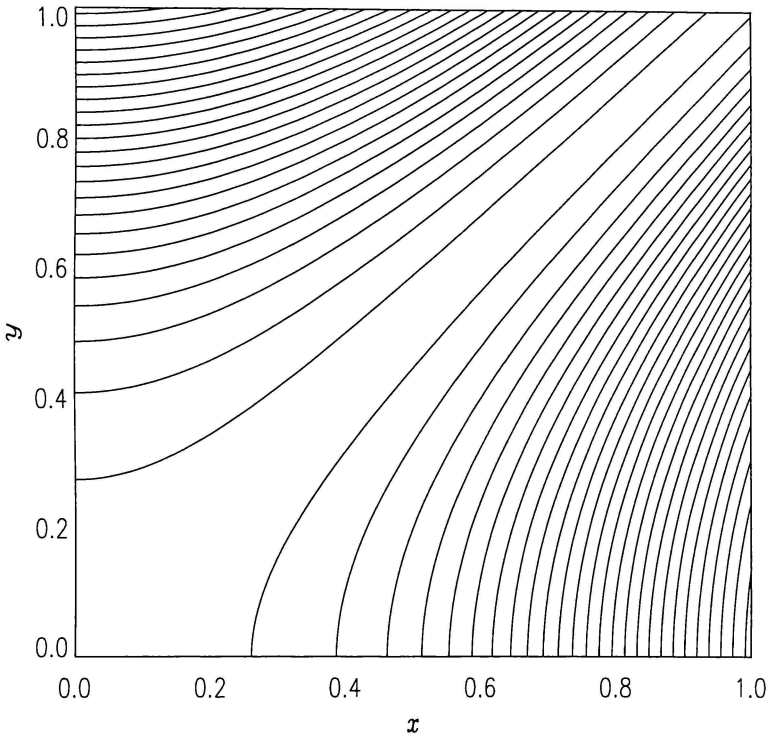


Figure 5.6a. Contour plot of $\nabla^2\psi$ for $E = 0.2, \eta = 1.0$.

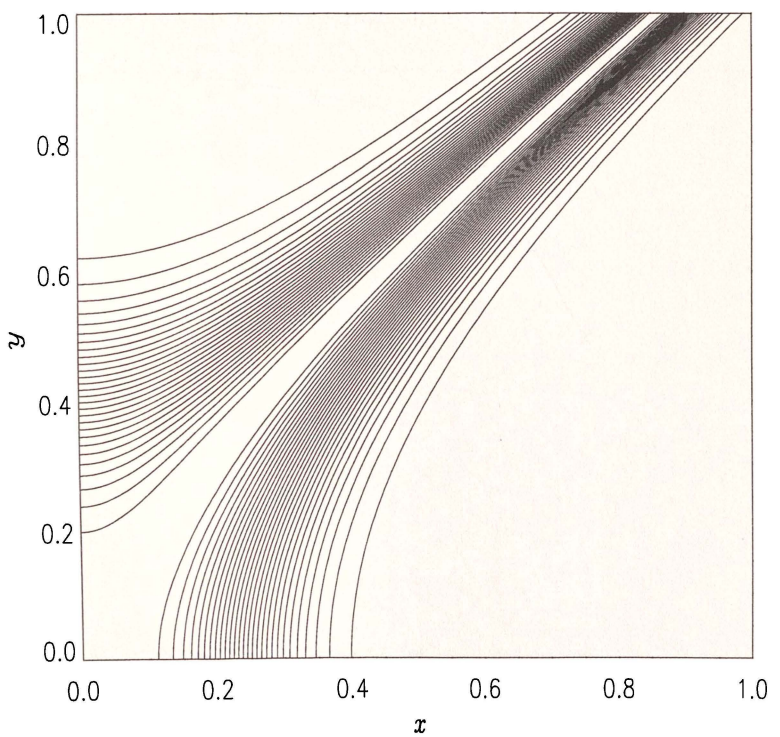


Figure 5.6b. Contour plot of $\nabla^2\psi$ for $E = 0.2, \eta = 0.1$.

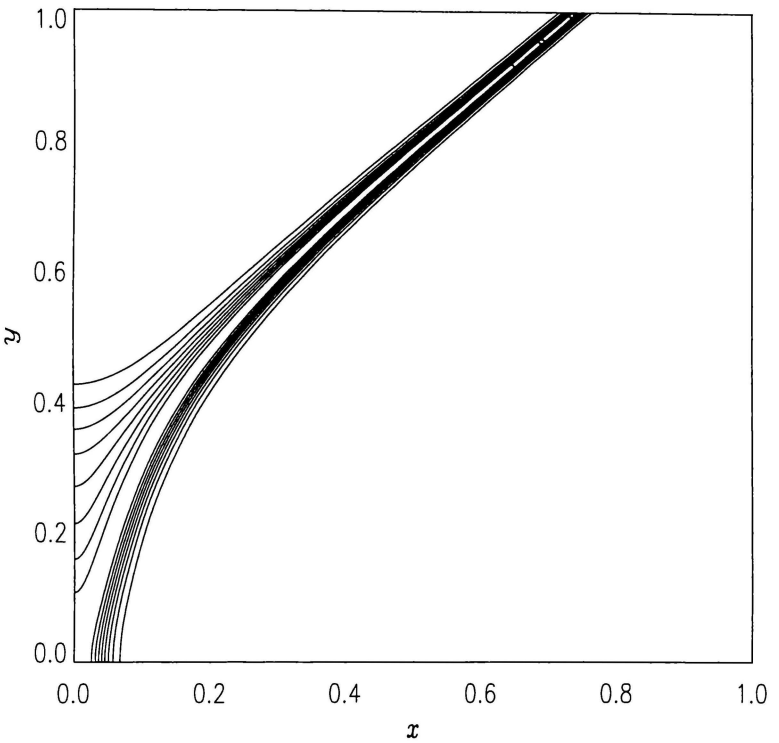


Figure 5.6c. Contour plot of $\nabla^2\psi$ for $E = 0.2, \eta = 0.01$.

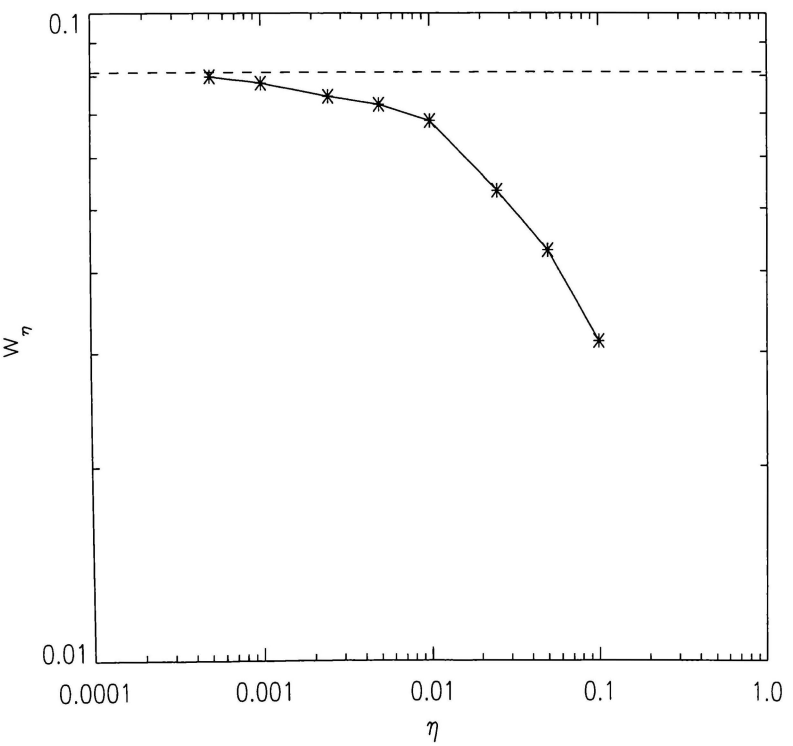


Figure 5.7. Graph of W_η versus η.

These choices allow direct comparisons to be made with our linear solution. For large values of η, a given non-linear solution must duplicate the linearised case. However as η approaches realistic values, non-linearity becomes important.

Figure 5.4 presents contour plots of (a) ϕ and (b) ψ and Figure 5.5 gives surface plots of (a) $\nabla^2\psi$ and (b) $p - p_0$ for $E = 0.2, \eta = 0.2$. The global current and strong shear flows of our linear solution have remained – see Figures 5.2 and 5.3. Again plasma is travelling inward along the x-axis and outward along the y-axis.

The effect of systematically decreasing η (while holding E fixed) is shown in Figure 5.6. We first mention that the current distribution resembles our linear solution for large values of η. However the reduction of η obviously causes the non-linearity to take presidence. The important observation here is that non-linearity 'tries' to spread the current uniformly along the separatrices. Now the distribution of current, and hence the vorticity, becomes largely one-dimensional.

We now evaluate our two reconnection measures. If we allow the flow outside the current sheet to be independent of η then

$$E \sim \eta^0,$$

and so the rate of magnetic flux annihilation scales as

$$\frac{\partial \psi}{\partial t} = E \sim \eta^0,$$

and is classed as a fast.

The rate of Ohmic dissipation was calculated numerically and the results are given in Figure 5.7. First note that W_η values for the largest η are inaccurate as the current is not sufficiently localised. Consequently a significant portion lies outside the integration range for these cases so estimating a scaling from these points is unreasonable.

As η reaches sufficiently small values we observe that

$$W_\eta = \eta \int_S (\nabla^2 \psi)^2 \, \mathrm{d}S \sim \eta^0,$$

which is indicated by the dashed line. Thus our second measure is also deemed to be fast.

5.5 Discussion

The non-linear analysis presented here naturally extends the linear analysis of Craig & Rickard (1994) and Priest & Forbes (1986). Only neglecting the flow term in (5.1) effectively retrieves much of the information lost by linearisation. Hence our findings can be regarded as the next step forward for establishing exact solutions of magnetic reconnection.

We mention that the method for calculating solutions might appear unusual. For time-dependent MHD problems, the momentmum equation (5.1) determines the flow while induction equation (5.2) usually determines the magnetic field. Here this order of evaluation is reversed because of the sub-Alfvénic approximations.

An important feature of both linear and non-linear solutions is the unambiguous nature of the outer boundaries. Imposing the traditional symmetries across the inner boundaries implies that outer boundary conditions for the plasma flow are not needed. Only conditions on the magnetic field along the outer boundaries are required. Thus concerns over determining a suitable *set* of boundary conditions have been overcome. Furthermore the outer boundaries are open-flow since plasma is continuously entering and exiting the modelled system.

Our findings seemingly suggest that exact solutions could be determined via an iterative procedure. In other words, a given approximated solution could be regarded as the initial conditions of some numerical relaxation scheme. However our attempts at this task were not successful. The non-linear combination of high-order derivatives coupled with the recurring problem of setting suitable boundary conditions resulted in our numerical codes not converging.

5.6 Summary

We have shown that non-linear solutions can be derived from the sub-Alfvénic MHD equations. An arbitrary function arises in the governing equations which can be judiciously chosen to give fast energy releases. However the energy release is *not* via reconnection – magnetic field lines are annihilated along the separatrices. This result indicates that the flow term $[\nabla^2\phi, \phi] \neq 0$ for steady-state solutions of two-dimensional reconnection.

Important features can be identified from our sub-Alfvénic analysis. We found that (i) strong shear flows about the separatrices exist, (ii) current and vorticity are global quantities and (iii) current and vorticity are highly one-dimensional. Note that none of these properties appear in the traditional picture of reconnection. What is more, these properties shall become 'building blocks' for deriving exact solutions of two dimensional reconnection in the following chapters.

CHAPTER 6

Exact Steady-State Solutions

6.1 Introduction

We now address the problem of constructing exact solutions from the steady-state MHD equations. To our knowledge no exact solutions of two-dimensional reconnection have published. Here we exploit the findings from our sub-Alfvènic analysis in Chapter 5 to establish exact solutions of two-dimensional reconnection. The material given in this chapter has also been published in Craig & Henton (1995) and Craig, Fabling, Henton & Rickard (1995).

Section 6.2 derives exact solutions for anti-parallel magnetic fields. We then derive two-dimensional solutions in Section 6.3. It shall be demonstrated that our one-dimensional solutions can be extended into two dimensions. A discussion of our findings is presented in Section 6.4. Next Section 6.5 outlines how our planar solutions can be generalised to three dimensions. A summary of this chapter is given in Section 6.6.

6.2 One-Dimensional Solutions

6.2.1 Derivation

We now derive exact solutions for the merging of anti-parallel magnetic fields. These solutions will assist our derivation of two-dimensional solutions in the next section. A significant body of research has been published on solutions for the annihilation of strictly one-dimensional magnetic fields. We mention the papers by Sonnerup & Priest (1975), Besser *et.al.* (1990, 1991) and Jardine (1992). In addition, annihilation solutions that include finite viscosity have also appeared in Gratton *et.al.* (1988, 1990), Sonnerup & Phan (1990) and Phan & Sonnerup (1990).

The steady-state MHD equations for an incompressible plasma were formulated in Chapter 5. We expressed them as

$$[\nabla^2\phi, \phi] = [\nabla^2\psi, \psi], \tag{6.1}$$

$$E + [\psi, \phi] = \eta\nabla^2\psi, \tag{6.2}$$

where $\phi(x,y)$ is a stream function and $\psi(x,y)$ is a magnetic flux function. Meanwhile E is a constant electric field and η denotes the plasma resistivity.

By taking ψ to be

$$\psi = \psi(x),$$

equations (6.1) and (6.2) reduce to

$$[\nabla^2\phi, \phi] = 0, \tag{6.3}$$

$$E + \phi_y\psi' = \eta\psi'', \tag{6.4}$$

where dashes signify x-derivatives. The line $x = 0$ is the separatrix for both the magnetic field and plasma flow.

Equation (6.4) indicates that ϕ must take the form

$$\phi = u(x)y + v(x).$$

Here u denotes the x-component of the plasma velocity and v accounts for flow of plasma across the x-axis. Note that $v = 0$ under the traditional symmetries detailed in Chapter 2.

Substituting this form for ϕ into (6.3) gives

$$u''u' - uu''' = 0,$$

$$u''v' - uv''' = 0,$$

which can be readily solved.

The traditional symmetries imply that the plasma cannot flow across $x = 0$. Thus our flow solutions are

$$\phi = \alpha xy + \frac{1}{2}\gamma x^2, \tag{6.5}$$

$$\phi = \alpha\sin(kx)y + \gamma\cos(kx), \tag{6.6}$$

$$\phi = \alpha\sinh(kx)y + \gamma\cosh(kx), \tag{6.7}$$

where α, γ and k are parameters. The last term in each expression corresponds to a one-dimensional shear of ϕ about the neutral line. We also remark that only the solution $\phi = \alpha xy$ results in an irrotational flow of plasma.

Equation (6.4) now becomes

$$E + u\psi' = \eta\psi'', \tag{6.8}$$

which can be solved once u has been specified. By introducing

$$P(r) = \exp\left(\frac{+1}{\eta}\int_0^r u(\hat{r})\,\mathrm{d}\hat{r}\right), \qquad Q(s) = \exp\left(\frac{-1}{\eta}\int_0^s u(\hat{s})\,\mathrm{d}\hat{s}\right),$$

the solution can be written as

$$\psi(x) = \frac{E}{\eta}\int_0^x P(r)\,\mathrm{d}r \int_0^r Q(s)\,\mathrm{d}s. \tag{6.9}$$

Each solution for ϕ can be approximated by (6.5) in the vicinity of the neutral line. Thus the magnetic field for all our flow solutions can be approximated by

$$B(x) = -\psi'(x) = -\frac{E}{\eta\mu}\mathrm{daw}(\mu x), \qquad \mu^2 = -\frac{\alpha}{2\eta}, \tag{6.10}$$

where

$$\mathrm{daw}(z) = \int_0^z \exp(k^2 - z^2)\mathrm{d}k,$$

represents a Dawson function (Spanier & Oldham 1987) – also see Figure 6.2a. We have

$$\mathrm{daw}(z) \approx \mu z, \qquad z \ll 0,$$

$$\mathrm{daw}(z) \approx -\frac{1}{2\mu z}, \qquad z \gg 0,$$

$$\frac{\mathrm{d}(\mathrm{daw}(z))}{\mathrm{d}z} = 0 \qquad \text{when} \qquad z \approx 0.924.$$

Our solutions will be fully specified when boundary conditions for ϕ and ψ are given. The outer region must be essentially current-free therefore η cannot influence our solutions at the outer boundary. Hence the magnetic field and plasma flow along the inflow boundary must be insensitive to η. This implies that α, γ and E are all independent of η.

We must specify $\alpha < 0$ on physical grounds. This corresponds to magnetic field lines being carried into a current sheet overlying $x = 0$. Solutions with $\alpha > 0$ describe field lines being carried away from $x = 0$ and current 'banking up' against the outer boundary. Obviously this current structure is unrealistic so solutions for $\alpha > 0$ are rejected.

We recall from Chapter 2 that

$$\mathbf{v}.\nabla\mathbf{v} = (\nabla \times \mathbf{B}) \times \mathbf{B} - \nabla p, \tag{6.11}$$

where p is the plasma pressure and remembering that we have set $\rho = 1$.

Substituting (6.5) and (6.10) into (6.11) and then integrating gives

$$p = p_0 - \frac{1}{2}(u^2 + B^2), \tag{6.12}$$

where p_0 is a constant background pressure with u and B being defined above.

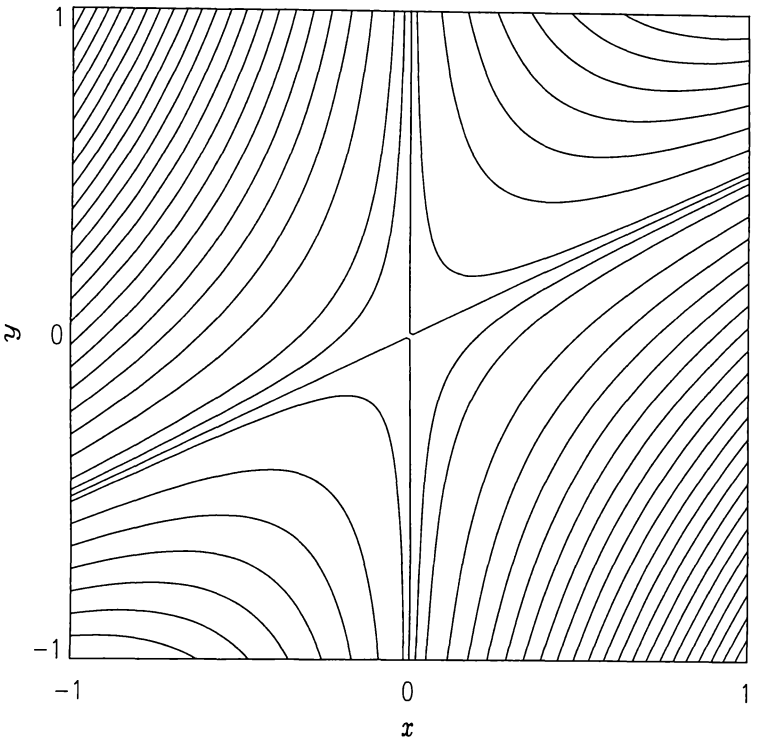


Figure 6.1a. Contour plot of ϕ for $E = 1, \eta = 1 \times 10^{-2}$ with $\alpha = -1, \gamma = 1$.

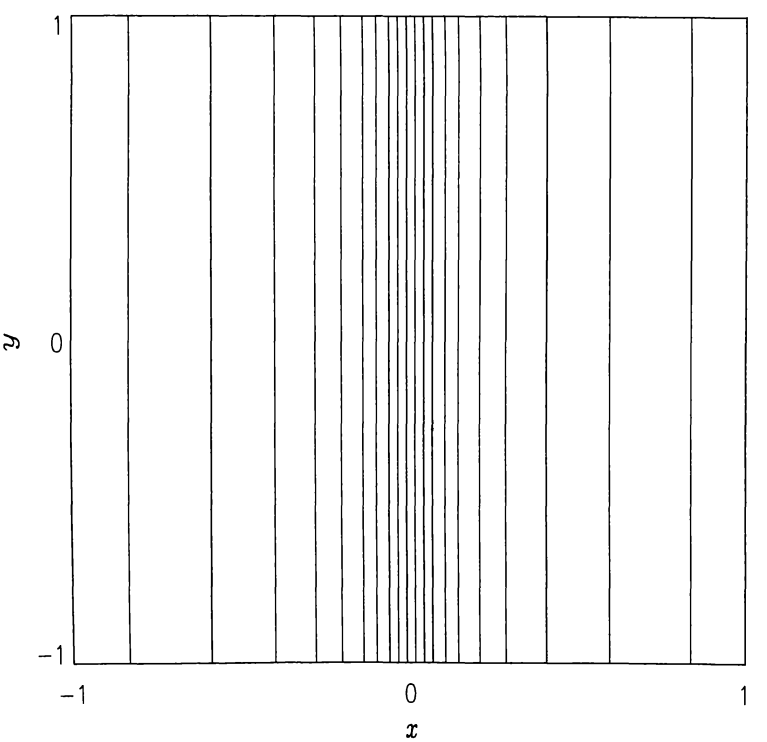


Figure 6.1b. Contour plot of ψ for $E = 1, \eta = 1 \times 10^{-2}$ with $\alpha = -1, \gamma = 1$.

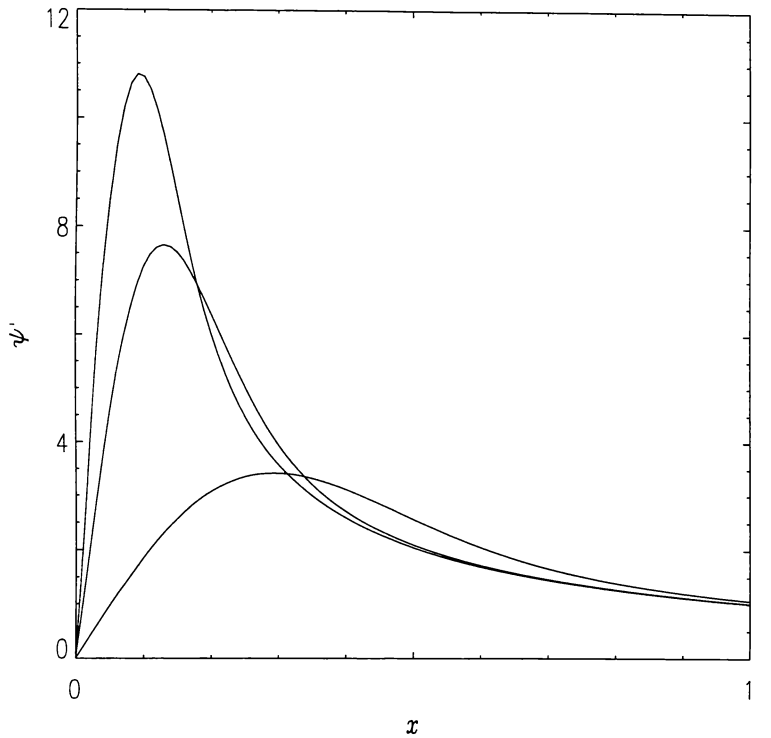


Figure 6.2a. Plot of ψ' versus x for $E = 1$ and $\eta = 5 \times 10^{-3}, 1 \times 10^{-2}, 5 \times 10^{-2}$ with $\alpha = -1, \gamma = 0$.

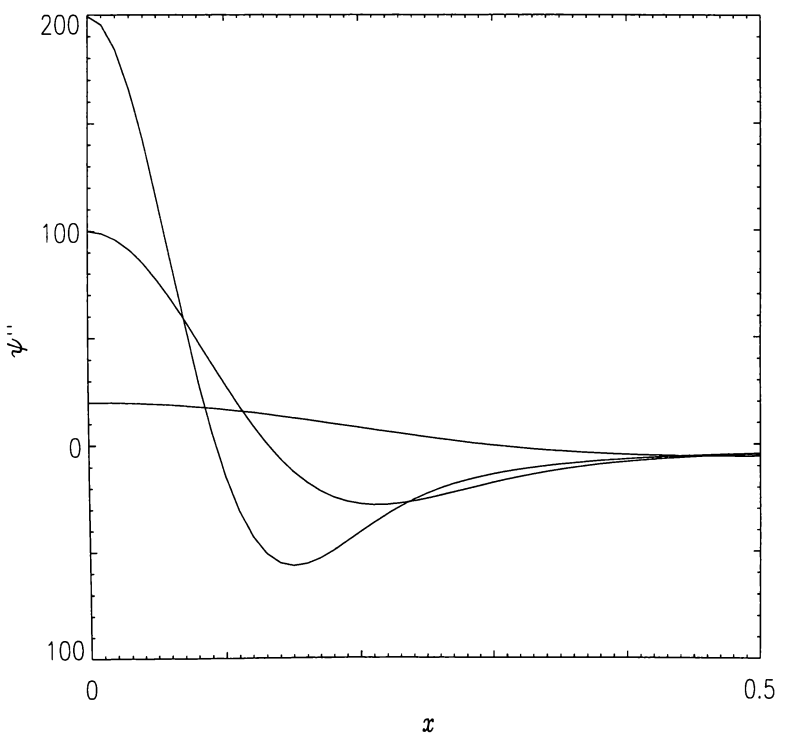


Figure 6.2b. Plot of ψ'' versus x for $E = 1$ and $\eta = 5 \times 10^{-3}, 1 \times 10^{-2}, 5 \times 10^{-2}$ with $\alpha = -1, \gamma = 0$.

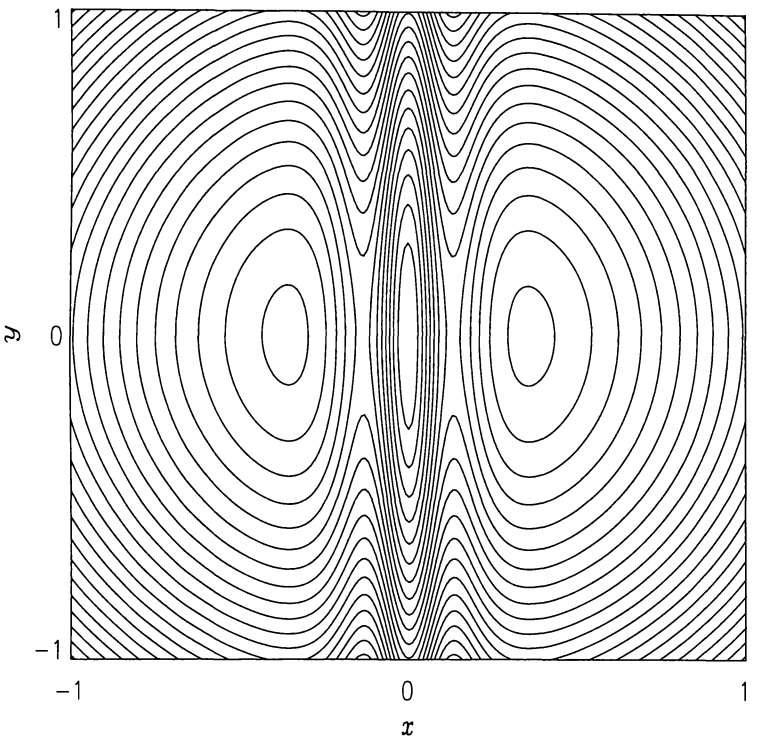


Figure 6.3a. Contour plot of p for $E = 1 \times 10^{-1}, \eta = 1 \times 10^{-2}$ with $\alpha = -1, \gamma = 0$.

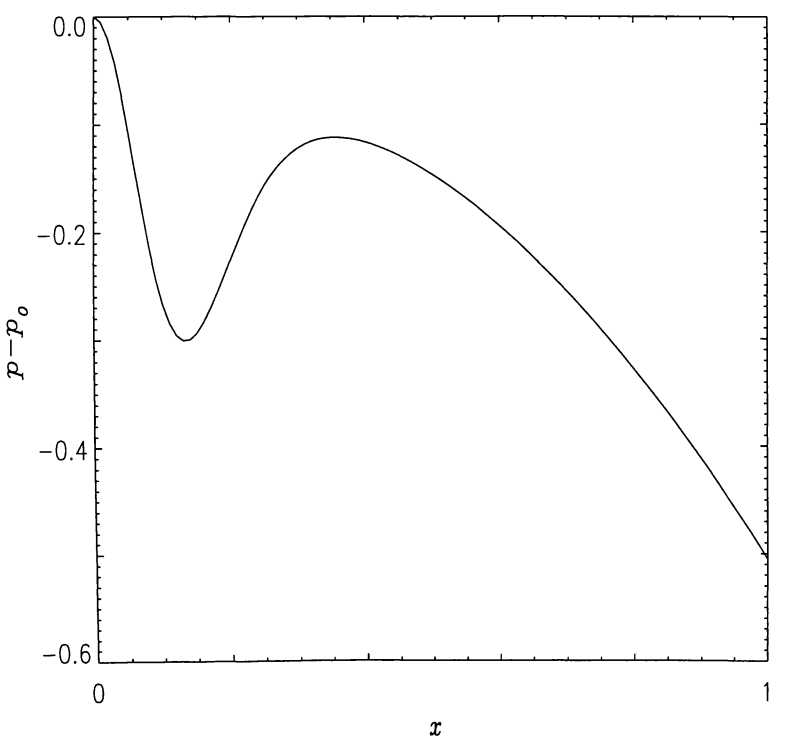


Figure 6.3b. Profile of $p - p_0$ along x-axis for $E = 1 \times 10^{-1}, \eta = 1 \times 10^{-2}$ with $\alpha = -1, \gamma = 0$.

6.2.2 A Particular Solution

In Figure 6.1 we present contour plots of (a) $\phi = \alpha xy + \frac{1}{2}\gamma x^2$ and (b) ψ for $E = 1, \eta = 1 \times 10^{-2}$ with $\alpha = -1, \gamma = 1$. Our sample solution illustrates that flow across $y = 0$ can still maintain the one-dimensionality of the magnetic field.

Figure 6.2 plots the profiles of (a) ψ' versus x and (b) ψ'' versus x for $E = 1$ and $\eta = 5 \times 10^{-3}, 1 \times 10^{-2}, 5 \times 10^{-2}$ with $\alpha = -1, \gamma = 0$. Note the pile-up of the magnetic field and subsequent current trough as η is reduced.

A contour graph of p for $E = 1, \eta = 1 \times 10^{-2}$ is given in Figure 6.3a. We also plot the profile of $p - p_0$ along the x-axis in Figure 6.3b. The large pressure gradient seen here is necessary for balancing the Lorentz forces indicated by Figure 6.2.

6.2.3 Diagnostics

We now evaluate the diagnostics relating to the current sheet that were introduced in Chapter 2. Using the properties of the Dawson function listed above yields

$$l \sim \eta^{1/2},$$

where l denotes the current sheet width.

The length of the current sheet is determined by the dimensions of modelled region. Thus we assign

$$L \sim \eta^0.$$

The value of B_{sheet} can be calculated as

$$B_{\text{sheet}} = B(x = l) \sim \eta^{-1/2}.$$

The current value along the neutral line is

$$J_0 = \frac{E}{\eta} \sim \eta^{-1},$$

which is reflected by the scalings for l and B_{sheet}.

As η is reduced, l decreases and B_{sheet} increases to create what is traditionally referred to as 'magnetic flux pile-up' – see Figure 6.2. Obviously this result contrasts the Sweet-Parker and Petschek assumption (see Chapter 3) that B_{sheet} is independent of η.

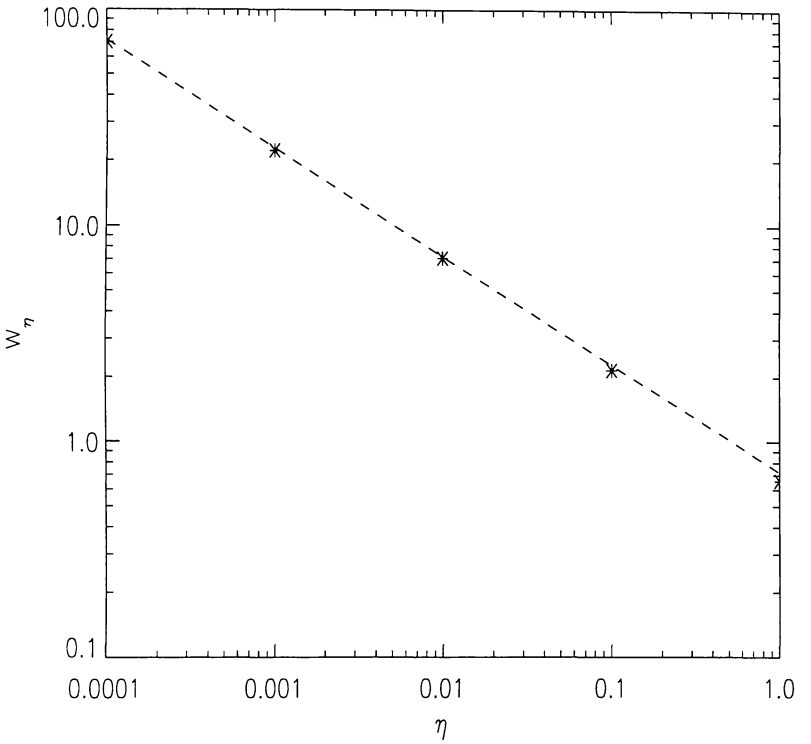


Figure 6.4. Graph of W_η versus η.

6.2.4 Magnetic Reconnection Rates

We now evaluate the rate of energy release. The flux annihilation rate scales as

$$\frac{\partial \psi}{\partial t} = E \sim \eta^0,$$

which is defined to be fast.

The rate of Ohmic dissipation is

$$W_\eta = \eta L \int_{-\infty}^{+\infty} (\psi'')^2 \mathrm{d}x,$$

and a simple approximation gives

$$W_\eta \approx \eta J_0^2 L l \sim \eta^{-1/2},$$

which is classed as ultra-fast. The numerically integrated Ohmic dissipation rate is plotted in Figure 6.4 with a dashed line indicating our approximation. We can conclude from this diagram that our proposed scaling is acceptable.

6.3 Two-Dimensional Solutions

6.3.1 Derivation

We now derive two-dimensional solutions of steady-state magnetic reconnection. First we recall the salient findings of Chapter 5. It was found that

(i) current and vorticity distributions are one-dimensional,

(ii) current sheets are contiguous with vorticity sheets,

(iii) the bracketed terms in the governing equations cannot be zero.

We elect to introduce trial forms for ϕ and ψ with the motivation behind this approach is being two-fold. Firstly the features listed above can be incorporated *a priori* into our solutions. Secondly helpful simplifications of (6.1) and (6.2) can be achieved.

We shall *not* impose the traditional symmetries – see Chapter 2. Instead we simply demand that plasma cannot flow across $x = 0$. It is our view that adopting the traditional symmetries may be too restrictive for solutions of steady-state reconnection. What is more, our one-dimensional analysis demonstrates that breaking these inner conditions still gives acceptable solutions.

Our derivation of two-dimensional solutions begins with (6.1). When either bracket term is zero, for example

$$[\nabla^2\psi, \psi] = 0,$$

we know that two possible solutions are

$$\psi = \psi(x), \qquad\qquad \nabla^2\psi = 0.$$

This result suggests we seek solutions of the form

$$\phi = \alpha h(x, y) + f(x),$$

$$\psi = \beta h(x, y) + g(x),$$

where α and β are parameters, f and g are arbitrary functions, and

$$\nabla^2 h = 0.$$

To generate a current sheet along $x = 0$ we also demand that g is an even function.

Substituting ϕ and ψ into (6.1) gives

$$(\alpha f''' - \beta g''')h_y = 0,$$

and as $h_y \neq 0$ we must have

$$f = \frac{\beta}{\alpha} g + \frac{1}{2}\gamma x^2,$$

where γ is another parameter.

Substituting our form for f into (6.2) gives

$$E + [-\beta\gamma x + \frac{\alpha^2 - \beta^2}{\alpha} g'] h_y = \eta g'',$$

and so

$$h = xy,$$

which gives

$$E - \beta\gamma x^2 + \frac{\alpha^2 - \beta^2}{\alpha} x g' = \eta g''. \tag{6.13}$$

The solution of (6.13) can be written as

$$g(x) = \frac{E}{\eta} \int_0^x P(r)\,\mathrm{d}r \int_0^r (1 - \frac{\beta\gamma\eta}{E} s^2) Q(s)\,\mathrm{d}s, \tag{6.14}$$

with P and Q ($u = \alpha x$) being defined in Section 6.2. Another way to express this result is

$$b(x) = -g'(x) = -\frac{E}{\eta\mu} \mathrm{daw}(\mu x), \qquad \mu^2 = \frac{\beta^2 - \alpha^2}{2\alpha\eta}, \tag{6.15}$$

where b denotes the magnetic field along the x-axis.

As both (6.1) and (6.2) are now satisfied identically, we have succeeded in deriving two-dimensional solutions of the steady-state problem! We emphasise that, until now, no exact solutions of two-dimensional reconnection were known – only the one-dimensional solutions detailed earlier.

In summary, our solutions are

$$\phi = \alpha xy + \frac{1}{2}\gamma x^2 + \frac{\beta}{\alpha} g, \tag{6.16}$$

$$\psi = \beta xy + g, \tag{6.17}$$

where g is given by (6.14). The plasma flow and magnetic field are given by

$$\mathbf{v} = (\alpha x, -\alpha y - \frac{\beta}{\alpha}\frac{E}{\eta\mu} \mathrm{daw}(\mu x) - \gamma x), \tag{6.18}$$

$$\mathbf{B} = (\beta x, -\beta y - \frac{E}{\eta\mu} \mathrm{daw}(\mu x)), \tag{6.19}$$

where the Dawson function earlier.

Substituting (6.18) and (6.19) into (6.11) gives

$$p = p_0 - \frac{1}{2}(u^2 + b^2) + \beta y b, \tag{6.20}$$

where

$$\mathbf{u} = (\alpha x, -\alpha y), \qquad b = -g',$$

and p_0 is a constant background pressure.

Our solutions are specified by the parameters α, β, γ and the electric field E. We first mention that choosing a finite value for γ imposes a uniform vorticity and current upon the MHD system. Here we set $\gamma = 0$ to maintain a localised current distribution.

We require the background components of the magnetic field and plasma flow to be independent of η. This demand implies that α and β must be specified independently of η. The contributions arising from the shearing function g must also be η invariant along the inflow boundary. Hence we must choose E independently of η.

With appropriate parameter choices, our solutions can be related to the earlier steady-state analysis. By choosing $\beta = 0$ we recover our one-dimensional solution with stagnation-point flow in Section 6.2. Also by specifying $f = g = 0$ and $\alpha = 0$, our zeroth-order solution in Chapter 5 is retrieved.

6.3.2 Parameter Choices

Only certain nominations of our parameters α and β will give sensible results. The current distribution, given by (6.13), must be localised so we have

$$\frac{\alpha^2 - \beta^2}{\alpha} \leq 0.$$

The three combinations of α and β that satisfy this condition are now discussed.

(i) $|\alpha| = |\beta|$

Specifying $|\alpha| = |\beta|$ reduces our solutions to

$$\phi = \pm\psi,$$

$$\psi = \alpha x y + \frac{E}{2\eta} x^2,$$

where the sign of ϕ depends on the sign of β. This trivial solution corresponds to a constant current and vorticity distribution where plasma flow is constrained to motion along the magnetic field lines. The $|\alpha| = |\beta|$ case is of little interest.

(*ii*) $\alpha > 0$ and $|\alpha| < |\beta|$

This choice of α does not arise in our one-dimensional solutions in Section 6.2. In particular, as current distributions could not be localised for $\alpha > 0$, this parameter choice had to be excluded. However this restriction upon α can now, apparently, be relaxed so long as the condition $|\alpha| < |\beta|$ is also met.

The shortcoming of this class of solutions is the unrealistic nature of the reconnection process. A significant proportion of the magnetic flux entering the MHD system now *carries in* large currents. The magnetic flux leaving the system has become current-free and so the lost current has been 'deposited' in the sheet. This result implies that our current sheet is effectively being maintained by some external MHD process. We therefore conclude that this reconnection mechanism is unrealistic and Case (*ii*) solutions are discarded.

(*iii*) $\alpha < 0$ and $|\alpha| > |\beta|$

This class of solutions is current-free and vorticity-free in the outer regions – this provides plausible outer boundary conditions. Small perturbations at the outer boundary induce large currents along the neutral line for the expected values of $\eta = O(10^{-12})$. We therefore conclude that only this combination of α and β is acceptable.

6.3.3 A Particular Solution

In Figure 6.5 we present contour plots of (a) ϕ and (b) ψ for $E = 1 \times 10^{-2}, \eta = 2 \times 10^{-3}$ with $\alpha = -1, \beta = 0.75, \gamma = 0$. Clearly ϕ and ψ have a similar topology. Both functions arise from a one-dimensional shear of a stagnation-point solution about the neutral line.

Plots of f'' (dashed line) versus x and g'' (solid line) versus x for $E = 1 \times 10^{-2}, \eta = 2 \times 10^{-3}$ with $\alpha = -1, \beta = 0.75, \gamma = 0$ is given in Figure 6.6. The current sheet extends from the one-dimensional solutions but the overlying vorticity sheet is an important difference.

A contour plot of p for $E = 1 \times 10^{-2}, \eta = 2 \times 10^{-3}$ with $\alpha = -1, \beta = 0.75, \gamma = 0$ is given in Figure 6.7. This diagram further illustrates the sheared nature of our two-dimensional solutions.

6.3.4 Interpretation

We now, with the aid of Figures 6.5 and 6.6, give a qualitative interpretation of our steady-state mechanism. First we observe that the solution tends to a current-free and vorticity-free equilibrium outside the current sheet. Flow of plasma in these outer regions is essentially confined to motion along the magnetic field lines. One could therefore imagine that a small disturbance at the outer boundary took place which led to a new steady-state solution.

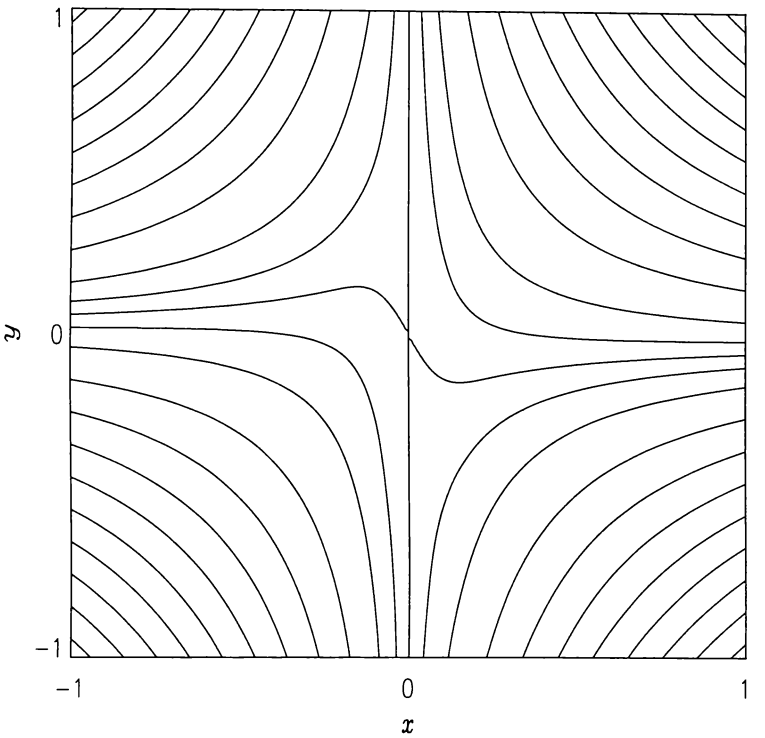


Figure 6.5a. Contour plot of ϕ for $E = 1 \times 10^{-2}, \eta = 2 \times 10^{-3}$ with $\alpha = -1, \beta = 0.75, \gamma = 0$.

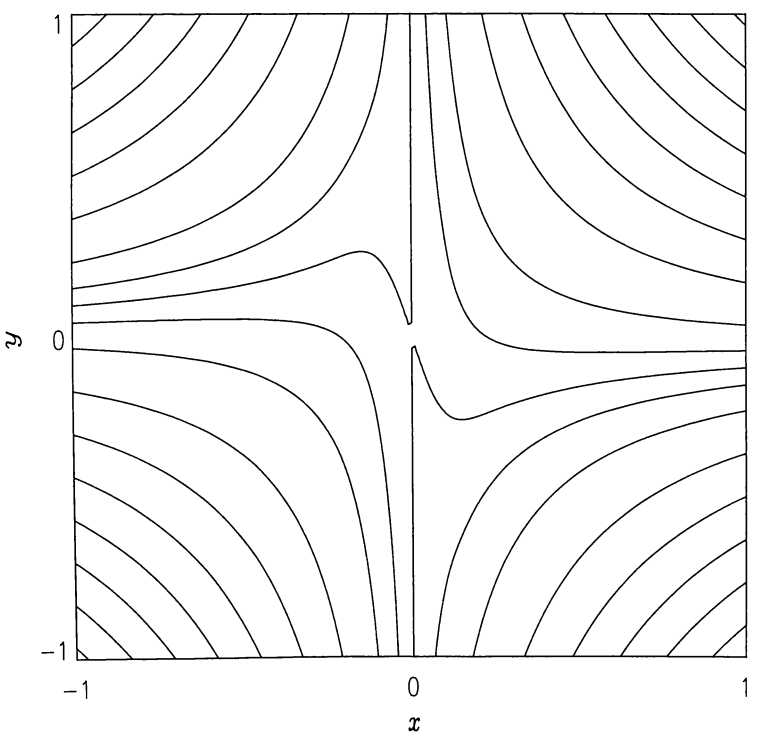


Figure 6.5b. Contour plot of ψ for $E = 1 \times 10^{-2}, \eta = 2 \times 10^{-3}$ with $\alpha = -1, \beta = 0.75, \gamma = 0$.

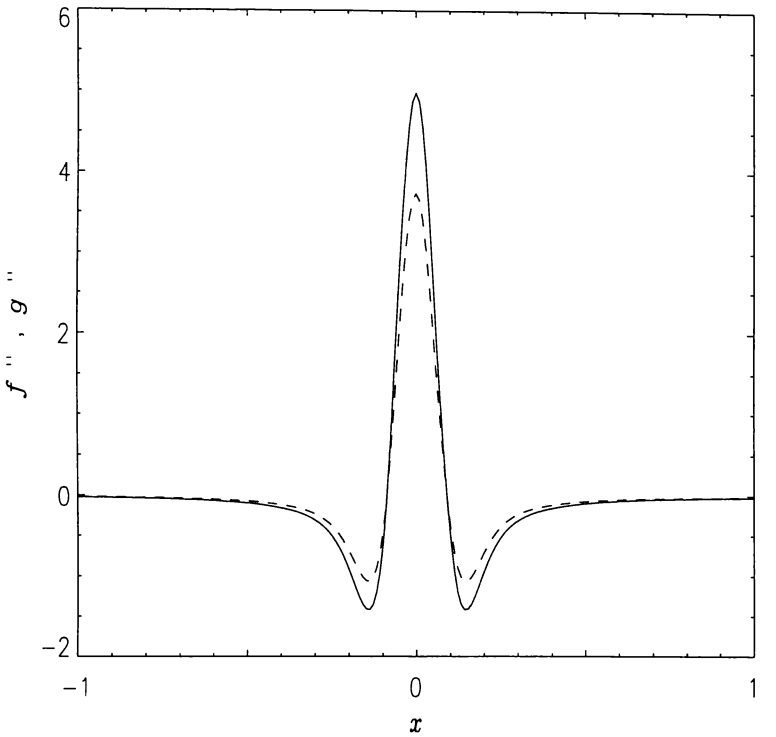


Figure 6.6. Profile of f'' (dashed line) and g'' (solid line) versus x for $E = 1 \times 10^{-2}, \eta = 2 \times 10^{-3}$ with $\alpha = -1, \beta = 0.75, \gamma = 0$.

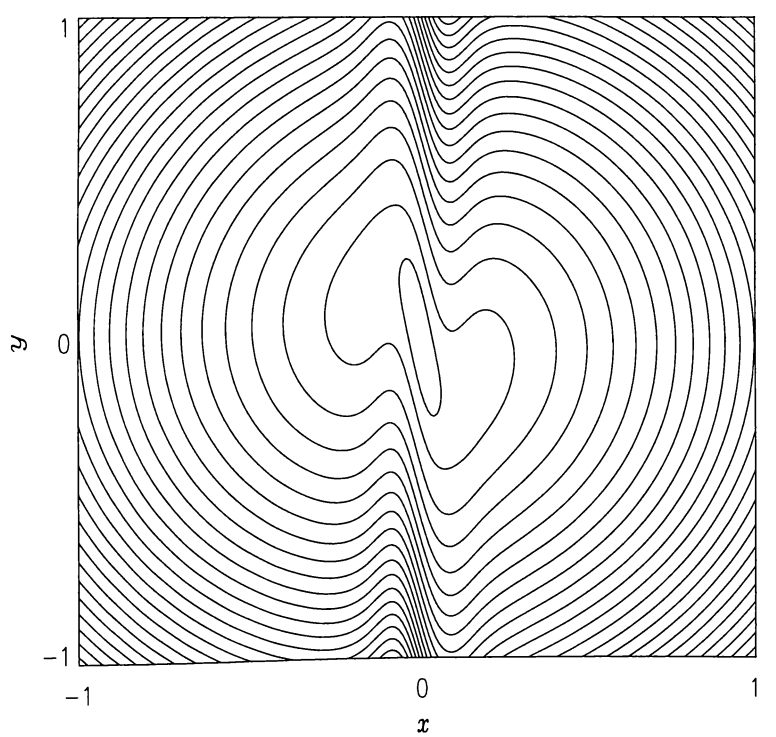


Figure 6.7. Contour plot of p for $E = 1 \times 10^{-2}, \eta = 2 \times 10^{-3}$ with $\alpha = -1, \beta = 0.75, \gamma = 0$.

The external flow drives plasma along the magnetic field lines toward the neutral line at $x = 0$. On nearing this line, both ϕ and ψ begin to shear dramatically. This is clearly illustrated by the warped nature of each horizontal separatrix in Figure 6.5. Furthermore ψ and ϕ are now seen to decouple with the extent of this separation being governed by α and β. As demonstrated shortly, the closer we choose α and β, the less we separate ϕ and ψ.

The flux function ψ initially shears away from the x-axis and a current trough is generated. Eventually tension in the magnetic field lines 'pulls back' ψ and creates the current sheet overlying $x = 0$. We point out that a vorticity layer is generated simultaneously via a similar shearing of ϕ. In fact the contours of ϕ are also being reconnected at the neutral point.

6.3.5 The Separatrices

The separatrices of ϕ and ψ intersect the neutral line at different angles. Under the traditional symmetries (see Chapter 2) the intersection angle is *forced* to be perpendicular for *both* ϕ and ψ separatrices. Obviously this feature of our two-dimensional solutions highlights the restrictive nature of the traditional symmetries.

We can readily evaluate the angle of intersection for each separatrix. For ψ this angle is

$$\theta_\psi = \tan^{-1}(\frac{2\beta\eta}{E}),$$

while for ϕ we have

$$\theta_\phi = \tan^{-1}(\frac{2\alpha^2\eta}{\beta E}).$$

Obviously these angles are not equal and, furthermore, neither separatrix curve can be perpendicular to the neutral line.

Several interesting features emerge from these expressions. We remark that θ_ψ is independent of α while the θ_ϕ varies with respect to both α and β. Thus amplifying α only increases the shearing tendency of ϕ. On the other hand, amplifying β increases the shearing of ψ but decreases the shearing tendency of ϕ.

Both angles of intersection decline as η is reduced. Hence the shearing tendencies of ϕ and ψ have been increased. The current sheet increases in magnitude and further localises on reducing η so this behaviour is sensible.

Meanwhile decreasing E widens the intersection angles. Thus the shearing tendencies of ϕ and ψ have been reduced. We anticipate this outcome since the lowering E also reduces the magnitude of the background flow.

There is a fundamental difference between the magnetic field separatrices of our exact solutions and the separatrices of our approximate solutions in Chapter 5. Both separatrices

in the previous chapter define the contours of peak current. The separatrices of ψ in our exact solutions are *not* equivalent as the sheared separatrix is not contiguous with the contour of maximum current.

6.3.6 Diagnostics

Diagnostics pertaining to the current sheet are now evaluated. The properties of the Dawson function imply that the sheet dimensions scale as

$$l \sim \eta^{1/2}, \qquad L \sim \eta^{0}.$$

We remark that l and L also give the dimensions of the vorticity sheet.

The magnetic field at the current sheet edge scales as

$$B_{\text{sheet}} = b(x = l) \sim \eta^{-1/2},$$

where b is the magnetic field along the x-axis.

The value of the current along the separatrix is

$$J_0 = \frac{E}{\eta} \sim \eta^{-1},$$

which can be discerned from the scalings for l and B_{sheet}.

Our above results reflect the one-dimensional scalings in Section 6.2 and have retained the 'flux pile-up' phenomenon. A pile-up of the magnetic field now appears an intrinsic feature of steady-state reconnection.

6.3.7 Magnetic Reconnection Rates

We now evaluate the rate of energy release. The flux annihilation rate scales as

$$\frac{\partial \psi}{\partial t} = E \sim \eta^{0},$$

and is deemed to be fast.

The rate of Ohmic dissipation is is

$$W_\eta = \eta \int_S (\nabla^2 \psi)^2 \mathrm{d}S = \eta L \int_{-\infty}^{+\infty} (g'')^2 \mathrm{d}x.$$

An approximation gives

$$W_\eta \approx \eta J_0^2 L l \sim \eta^{-1/2},$$

which is classed as ultra-fast. A confirmation of our estimated scaling for W_η already appears in Section 6.2.

6.4 Discussion

The one-dimensional solutions of Section 6.2 result (exclusively) in magnetic annihilation. Thus no *reconnecting* of magnetic field lines can occur. We further point out that this phenomenon applied in Chapter 5. Our two-dimensional solutions clearly overcome this problem and reconnection can be readily observed.

Our trial forms for ϕ and ψ overcame the problems encountered in Chapter 5. Firstly we no longer are required to specify an arbitrary function. Secondly our solutions for ϕ and ψ were determined simultaneously from both MHD equations. Clearly the separable outcome where ψ could be determined uniquely from one of the approximated equations has been avoided.

Our two-dimensional solutions agree favourably with the approximate findings of Chapter 5. The global current sheet and intense vorticity layer have persisted. Once again it appears that current and vorticity are closely related quantities in steady-state reconnection. Our exact solutions also re-iterate that shearing motions are likely features of magnetic reconnection.

The analytical nature of our solutions means that problems over determining suitable boundary conditions have been avoided. Now only the external parameters α, β, γ and E need to be specified. Furthermore the boundaries are open-flow – plasma is simultaneously entering and exiting the modelled region.

It is critical to note that the traditional inner symmetries depress our two-dimensional solutions. This suggests that imposing the traditional symmetries only hampers the development of planar reconnection mechanisms. Hence steady-state reconnection may require a certain lack of symmetry in the magnetic field and plasma flow.

A consequence of our two dimensional solutions, and the one-dimensional solutions for that matter, is the magnitude of the plasma pressure p on the outer boundary. On physical grounds, we must have $p \geq 0$. Equation (6.20) therefore implies that $p_0 = O(\frac{1}{\eta})$ where p_0 is the background pressure. Thus a massive plasma pressure along the outer boundary characterises our exact solutions which seems physically unreasonable.

6.5 Extending to Three Dimensions

An important feature of our two-dimensional solutions is the possibility of extension to three dimensions. One must first appreciate that the two-dimensional X-type neutral point can be naturally extended to three dimensions – see **P** below. In doing so, one separatrix becomes a plane ($x = 0$) whereas the other separatrix becomes a line (x-axis). This clearly highlights the need to consider each separatrix individually in the reconnection problem (see

also Lau & Finn (1990)). Now we show how our two-dimensional solutions, which have *distinctively* different separatrices, can be readily extended to three dimensions.

The incompressible steady-state equations can be expressed as

$$(\mathbf{v}.\nabla)\omega - (\omega.\nabla)\mathbf{v} = (\mathbf{B}.\nabla)\mathbf{J} - (\mathbf{J}.\nabla)\mathbf{B}, \tag{6.21}$$

$$(\mathbf{v}.\nabla)\mathbf{B} - (\mathbf{B}.\nabla)\mathbf{v} = \eta\nabla^2\mathbf{B}, \tag{6.22}$$

where

$$\nabla.\mathbf{B} = 0, \qquad \nabla.\mathbf{v} = 0,$$

and

$$\mathbf{J} = \nabla \times \mathbf{B}, \qquad \omega = \nabla \times \mathbf{v}.$$

Two classes of reconnective solutions appear which are now outlined individually. The first class has a distribution of current that overlies a plane and is therefore labelled a current fan. The second class has a current distribution concentrated about an infinite line which is termed a current spine. We acknowledge that the fan and spine terminology was first proposed by Priest & Titov (1995).

(i) Fan Solutions

In keeping with our two-dimensional analysis, we take

$$\mathbf{v} = \mathbf{P} + \mathbf{q}(x),$$

$$\mathbf{B} = \lambda\mathbf{P} + \mathbf{Q}(x),$$

where the shear components are

$$\mathbf{q} = V(x)\hat{\mathbf{y}} + W(x)\hat{\mathbf{z}},$$

$$\mathbf{Q} = Y(x)\hat{\mathbf{y}} + Z(x)\hat{\mathbf{z}},$$

and

$$\mathbf{P} = \alpha[-x\hat{\mathbf{x}} + \kappa y\hat{\mathbf{y}} + (1-\kappa)z\hat{\mathbf{z}}],$$

is our potential component while λ, α, κ denote parameters. We note that setting $\kappa = 1$ retrieves our two-dimensional solutions.

Substituting these forms into (6.21) and (6.22) gives

$$V(x) = \lambda Y(x) + \gamma_1 x,$$

$$W(x) = \lambda Z(x) + \gamma_2 x,$$

where Y and Z must satisfy

$$\alpha(1-\lambda^2)[\kappa Y + xY'] + \eta Y'' = \alpha\gamma_1\lambda(\kappa+1)x,$$

$$\alpha(1-\lambda^2)[(1-\kappa)Z + xZ'] + \eta Z'' = \alpha\gamma_2\lambda(2-\kappa)x,$$

subject to the conditions

$$\gamma_1(1-\kappa) = 0, \qquad \gamma_2\kappa = 0.$$

Here current is localised in the plane $x = 0$ – a current fan.

(*ii*) Spine Solutions

We now take the trial forms

$$\mathbf{v} = \mathbf{P} + \mathbf{q}(y,z),$$

$$\mathbf{B} = \lambda\mathbf{P} + \mathbf{Q}(y,z),$$

where $\mathbf{P}$ and λ are defined above.

Substituting these forms into (6.21) and (6.22) yields

$$\mathbf{q}(y,z) = \lambda X(y,z)\hat{\mathbf{x}},$$

$$\mathbf{Q}(y,z) = X(y,z)\hat{\mathbf{x}},$$

where X satisfies

$$\alpha(1-\lambda^2)[X + \kappa y X_y + (1-\kappa)X_z] = \eta\nabla^2 X,$$

which has current localised along the x-axis – a current spine.

A detailed analysis of the fan and spine solutions is still being conducted. The latest work can be found in Craig, Fabling, Henton & Rickard (1995) and Craig & Fabling (1996).

6.6 Summary

We have derived exact solutions of magnetic reconnection in two dimensions for an incompressible plasma. This achievement resulted from combining the results from our sub-Alfvènic work in Chapter 5 with the solution for annihilation of anti-parallel magnetic fields. Suitably chosen forms for ϕ and ψ simplified the MHD equations dramatically which enables us to obtain exact solutions.

Our derivation illustrated the apparent need to relax the traditional symmetries for steady-state reconnection. It now appears that the four-fold symmetry between the magnetic field and plasma flow is too restrictive for steady-state reconnection. Our exact solutions also

imply that the separatrices of the magnetic field are not equivalent. Clearly plasma motions across one separatrix induced the formation of a current sheet along the other separatrix.

As with the one-dimensional solutions, a problem arises from the unreasonable nature of the plasma pressure. It was demonstrated that an enormous pressure is required at the outer boundary for typical values of η. This force is necessary to maintain the stagnation-point flow and therefore drive the reconnection. We therefore conclude that the stalling of reconnection seen in Chapter 4 can be attributed to the lack of large hydromagnetic pressures outside the current sheet. The solutions presented here imply that two-dimensional reconnection will stall for coronal values of the plasma pressure.

Our two-dimensional solutions can be readily extended into three dimensions. Here we outlined how reconnective solutions that contain fan and spine distributions of current can be determined. Furthermore the trial forms for the magnetic field and plasma flow can be made time-dependent. The next chapter shows how our steady-state solutions can be extended to include time-dependency.

CHAPTER 7

Exact Time-Dependent Solutions

7.1 Introduction

This chapter returns to the issue of time-dependent magnetic reconnection. However, in contrast to Chapter 4, the problem is now tackled analytically. Here we extend the steady-state analysis in Chapter 6 to incorporate time-dependency by letting the shear components of our trial forms be time-dependent. It will be demonstrated that constructing solutions via this approach is relatively straight forward.

In Section 7.2 we simplify the MHD equations by specifying trial forms for the stream function and magnetic flux function. Sections 7.3 and 7.4 discuss two particular cases which can be dealt with analytically. The general case which is not analytically tractable is addressed in Section 7.5. A discussion of our time-dependent solutions is presented in Section 7.6. In Section 7.7 we detail how our planar solutions can be extended to three dimensions and a summary of this chapter is given in Section 7.8.

7.2 Governing Equations

The steady-state MHD equations for an incompressible plasma were formulated in Chapter 5. Allowing the stream function ϕ and the magnetic flux function ψ to be time-dependent gives

$$\omega_t + [\omega, \phi] = [J, \psi], \tag{7.1}$$

$$\psi_t + [\psi, \phi] = -\eta J, \tag{7.2}$$

where subscripts denote partial derivatives and

$$\omega = -\nabla^2 \phi, \qquad J = -\nabla^2 \psi,$$

are the vorticity and current respectively.

We recall that taking the trial forms

$$\phi(x, y) = \alpha x y + f(x),$$

$$\psi(x,y) = \beta xy + g(x),$$

where α, β are parameters and f, g are (initially) unknown functions led to exact solutions of steady-state reconnection. This outcome naturally suggests that we take

$$\phi(x,y,t) = \alpha xy + f(x,t),$$

$$\psi(x,y,t) = \beta xy + g(x,t),$$

where ϕ and ψ consist of a background component and a time-dependent shear component.

Substitution of ϕ and ψ into (7.1) and (7.2) gives

$$f_t + x(\alpha f_x - \beta g_x) - 2(\alpha f - \beta g) = 0, \tag{7.3}$$

$$g_t + x(\alpha g_x - \beta f_x) = \eta g_{xx}. \tag{7.4}$$

Once again our particular choice for ϕ and ψ has simplified the MHD equations dramatically.

The current distribution is obviously determined by (7.4). By introducing the variable $x = \bar{x}\eta^{1/2}$, we recognise that (7.3) and (7.4) become independent of η. This immediately implies that the current sheet width must scale as

$$l \sim \eta^{1/2},$$

which can be confirmed numerically.

The sheet length is determined by the dimensions of the modelled region. We therefore have

$$L \sim \eta^0.$$

Determining the scaling for J_0 will require more extensive analysis.

We recall from Chapter 2 that

$$\frac{\partial \mathbf{v}}{\partial t} + \mathbf{v}.\nabla\mathbf{v} = (\nabla \times \mathbf{B}) \times \mathbf{B} - \nabla p,$$

where p is the plasma pressure and remembering that $\rho = 1$.

Substitution of ϕ and ψ into this expression and then integrating gives

$$p(x,y,t) = p_0(t) - \frac{1}{2}(u^2 + b^2) + \beta y b, \tag{7.5}$$

where

$$\mathbf{u} = (\alpha x, -\alpha y), \qquad b = -g_x,$$

and p_0 is the background pressure.

7.3 The $\beta = 0$ Case

7.3.1 Derivation

We now focus out attention on the degenerate case of $\beta = 0$. This choice corresponds to anti-parallel magnetic fields being annihilated along a neutral line. Equations (7.3) and (7.4) become

$$f_t + x\alpha f_x = 2\alpha f, \tag{7.6}$$

$$g_t + x\alpha g_x = \eta g_{xx}, \tag{7.7}$$

which are clearly decoupled.

The solution of (7.6) can be determined by the method of characteristics. We find

$$f(x,t) = f_0(x\ \mathrm{e}^{-\alpha t})\ \mathrm{e}^{2\alpha t},$$

where f_0 represents the initial distribution for f.

A formal solution for g over the unbounded interval $(-\infty < x < +\infty)$ can be established by the Fourier transform method detailed in Clark (1964). First we differentiate (7.7) with respect to x and obtain

$$b_t + \alpha(xb)_x = \eta b_{xx}.$$

Next we take the Fourier transform to find

$$\frac{\partial \bar{b}}{\partial t} - \alpha k \frac{\partial \bar{b}}{\partial k} = -\eta k^2 \bar{b}, \tag{7.8}$$

where

$$\bar{b}(k,t) = \int_{-\infty}^{+\infty} b(x,t)\mathrm{e}^{ikx}\mathrm{d}x.$$

Note that, as (7.8) is a linear equation, the constant multiplier preceding the integral in $\bar{b}$ has been neglected.

The solution of (7.8) can be evaluated by the method of characteristics. This gives

$$\bar{b} = \bar{b}_0(k\mathrm{e}^{\alpha t})\exp(\frac{\sigma k^2 \mathrm{e}^{2\alpha t}}{2}),$$

where

$$\sigma = \frac{\eta}{\alpha}(\mathrm{e}^{-2\alpha t} - 1),$$

and $\bar{b}_0$ is given by the initial conditions. This expression can be inverted to obtain

$$b = -g_x = \frac{\mathrm{e}^{\alpha t}}{\sqrt{\sigma}} \int_{-\infty}^{+\infty} b_0(k)\ \exp\left(-\frac{(k - \mathrm{e}^{\alpha t}x)^2}{2\sigma}\right) \mathrm{d}k, \tag{7.9}$$

where b_0 denotes the initial distribution of b.

We must specify $\alpha < 0$ on physical grounds. This corresponds to magnetic field lines being carried into a current sheet overlying $x = 0$. Solutions with $\alpha > 0$ describe field lines being carried away from $x = 0$ and current 'banking up' against the outer boundary. Obviously this current structure is unrealistic so solutions for $\alpha > 0$ are rejected.

7.3.2 A Particular Solution

The general solution of b given in (7.9) gives little information about the energy release process. Let us now investigate a particular solution. The subsequent scalings should extend to other $\beta = 0$ solutions and this claim can be confirmed by a series of computer simulations.

Again we follow Clark (1964) and analyse the solution

$$f = 0, \qquad g = r(t)\mathrm{e}^{-x^2 s(t)},$$

and substitution into (7.7) yields

$$r(t) = \frac{C}{(1 + \eta D\mathrm{e}^{-2\alpha t})^{1/2}},$$

$$s(t) = -\frac{\alpha D\mathrm{e}^{-2\alpha t}}{2(1 + \eta D\mathrm{e}^{-2\alpha t})},$$

where C, D are constants. The initial distribution of g must be independent of η so

$$C = \sqrt{\frac{\alpha + 2\eta}{\alpha}}, \qquad D = -\frac{2}{\alpha + 2\eta}.$$

Thus both the constants have a negligible dependence on η for coronal values.

The motivations behind of our particular choice of g are

(i) this is a simple flux distribution that decays at large distances,

(ii) the neutral line is the only null in the magnetic field,

(iii) diagnostics can be evaluated analytically.

We now examine the evolution of g with the aid of Figure 7.1 and calculate diagnostics relating to the current sheet. The primary aim of Figure 7.1 is to illustrate the localisation of the magnetic field.

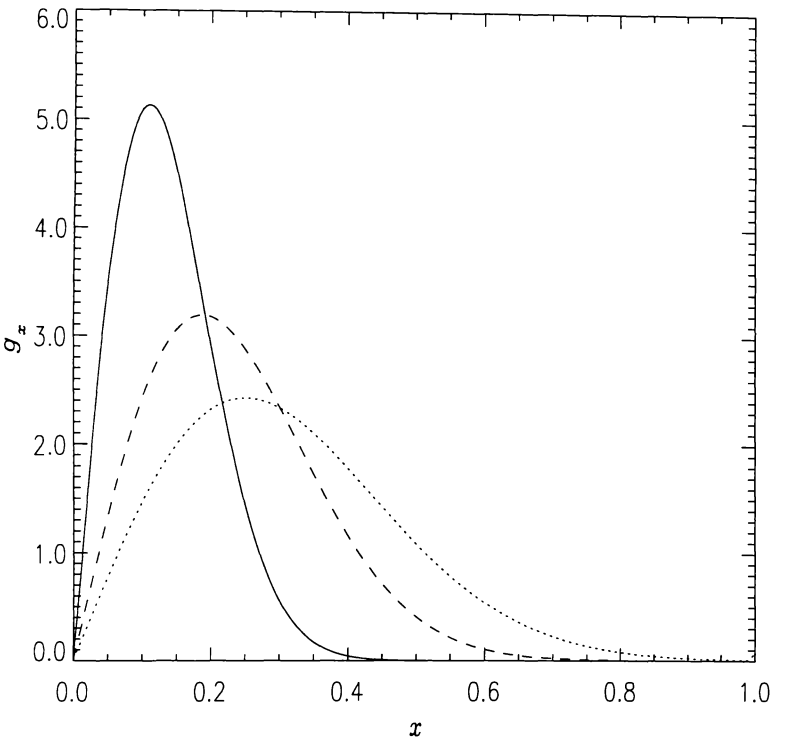


Figure 7.1. Evolution of g_x profile.

(i) The magnetic field is characterised by a single peak given by

$$B_{\rm pk}(t) = -r(t)\sqrt{2s(t)\mathrm{e}},$$

where e = 2.718... and this peak is located at

$$x = \sqrt{\frac{1}{2s(t)}}\,.$$

This peak travels towards $x = 0$ and grows in magnitude – see Figure 7.1. The peak eventually reaches the dynamical maximum

$$B_{\rm sheet} = \sqrt{\frac{\alpha \mathrm{e}}{4\eta}},$$

when

$$x = l = \sqrt{\frac{2\eta}{\alpha}}, \qquad t = \frac{1}{2\alpha}\ln(\eta D).$$

(ii) The current along the neutral line is

$$J(x = 0, t) = -2r(t)s(t),$$

which reaches the maximal value

$$J_0 = -(\frac{2\alpha}{\eta})3^{-3/2},$$

when

$$t = \frac{1}{2\alpha}\ln(\frac{\eta D}{2}).$$

(*iii*) The magnetic energy is given by

$$E_{\mathrm{mag}}(t) = \frac{1}{2}\int_{-\infty}^{+\infty}(g_x)^2 \mathrm{d}x = \sqrt{\frac{\pi}{8}}r(t)^2 s(t)^{1/2},$$

which peaks at the value

$$E_{\mathrm{mag}} = \frac{3}{8}\sqrt{\frac{\pi\alpha}{3\eta}},$$

when

$$t = \frac{1}{2\alpha}\ln(2\eta D).$$

We now turn our attention to the two measures of energy release. The rate of flux annihilation is

$$\frac{\partial\psi}{\partial t} = \eta g_{xx} = -2\eta r(t)s(t),$$

and reaches a maximum

$$\frac{\partial\psi}{\partial t} = -2\alpha 3^{-3/2} \sim \eta^0,$$

when

$$t = \frac{1}{2\alpha}\ln(\frac{\eta D}{2}),$$

and is deemed to be fast.

The rate of Ohmic dissipation can be written as

$$W_\eta(t) = L\eta\int_{-\infty}^{+\infty}(g_{xx})^2 \mathrm{d}x = L\eta\sqrt{\frac{9\pi}{2}}r(t)^2 s(t)^{3/2},$$

which attains a peak value

$$W_\eta = L\sqrt{\frac{18\pi}{25\eta}}(\frac{3\alpha}{10})^{3/2} \sim \eta^{-1/2},$$

when

$$t = \frac{1}{2\alpha}\ln(\frac{2\eta D}{3}),$$

and is classed as ultra-fast.

7.3.3 Discussion

We have demonstrated that, for sufficiently small values of η, the time of maximum current ($t_{\max}$ say) is of great significance. Here the build-up of magnetic flux B_{sheet} and magnetic energy E_{mag} peak and both our energy release measures attain a maximum value. Since J_0 occurs at a known location, namely the neutral point, examining the energy release at $t_{\max}$ appears a sensible choice.

The qualitative nature of our $\beta = 0$ solutions is relatively simple. A converging flow of plasma carries a magnetic pulse toward the neutral line. The flow increases the magnetic energy in the pulse by 'stretching' the field lines. Eventually the incoming field lines are resistively annihilated along $x = 0$ and a current sheet forms. We have shown that the bulk of magnetic energy is released via Ohmic heating of the plasma.

A leading criticism of one-dimensional solutions results from the lack of two-dimensionality in the magnetic field. Here the energy release is entirely due to the *annihilation* of magnetic flux along the neutral line – no reconnection takes place. Obviously one-dimensional solutions of (7.3) and (7.4) cannot provide a plausible flare model.

Another shortcoming of one-dimensional solutions is the 'death' of the magnetic field. All magnetic field lines are annihilated as $t \to \infty$. This result seems unacceptable on physical grounds since we expect to have a residual magnetic field. Therefore two-dimensional solutions of (7.3) and (7.4) that retain a finite magnetic field as $t \to \infty$ would be more realistic.

The concern over plasma pressure in our steady-state solutions still stands. As we must have $p > 0$, equation (7.5) implies that $p_0 = O(\frac{1}{\eta})$. Thus a massive pressure at the outer boundary is an inherent property of these one-dimensional solutions.

7.4 The $|\alpha| = |\beta|$ Case

7.4.1 The Outer Solution

We now derive an outer solution for the $|\alpha| = |\beta|$ case. Unlike our steady-state solutions in Chapter 6, this choice of parameters is acceptable. The following analysis is for $\alpha = \beta$.

The outer region of the MHD system can be regarded as current-free for sufficiently small values of η. Hence the resistive term is negligible so (7.3) and (7.4) can be approximated as

$$f_t + x\alpha(f_x - g_x) - 2\alpha(f - g) = 0, \tag{7.10}$$

$$g_t + x\alpha(g_x - f_x) = 0. \tag{7.11}$$

These equations can be reformulated as

$$h_t + 2x\alpha h_x - 2\alpha h = 0, \tag{7.12}$$

$$k_t - 2\alpha h = 0, \tag{7.13}$$

where we have defined

$$h = f - g, \qquad k = f + g.$$

Equation (7.12) and then (7.13) can be solved to obtain

$$h = 2[H(\theta) - \theta H'(\theta)]\mathrm{e}^{2\alpha t},$$

$$k = 2H(\theta)\mathrm{e}^{2\alpha t} + 2K(x),$$

where

$$\theta = x\mathrm{e}^{-2\alpha t},$$

and H, K are functions determined by the initial conditions.

We therefore have

$$f(x,t) = [2H(\theta) - \theta H'(\theta)]\mathrm{e}^{2\alpha t} + K(x),$$

$$g(x,t) = [\theta H'(\theta)]\mathrm{e}^{2\alpha t} + K(x),$$

as the outer solution.

Both f and g split up into a stationary component (the term involving K) and a localising component (the term involving H). The localisation of the incoming component will induce a build-up in current along the neutral line. We now investigate the subsequent energy release.

7.4.2 Diagnostics

Our solution for the outer region will not be valid near $x = 0$. The breakdown arises as the current along the neutral line grows dramatically and so the resistive term can no longer be neglected. However estimates for $t_{\max}$ can be determined from the outer solution which then provide an approximate scaling for J_0.

With $\eta = 0$ the outer solution would hold everywhere and the current at $x = 0$ would grow indefinitely. However the current build-up can be estimated to stop when

$$g_t \approx \eta g_{xx},$$

along the neutral line.

Substituting the localising component of g from our outer solution into this expression gives

$$t_{\max} \approx \frac{1}{4\alpha}\ln(\eta),$$

and the current at $t_{\max}$ scales as

$$J_0 \sim \eta^{-1/2},$$

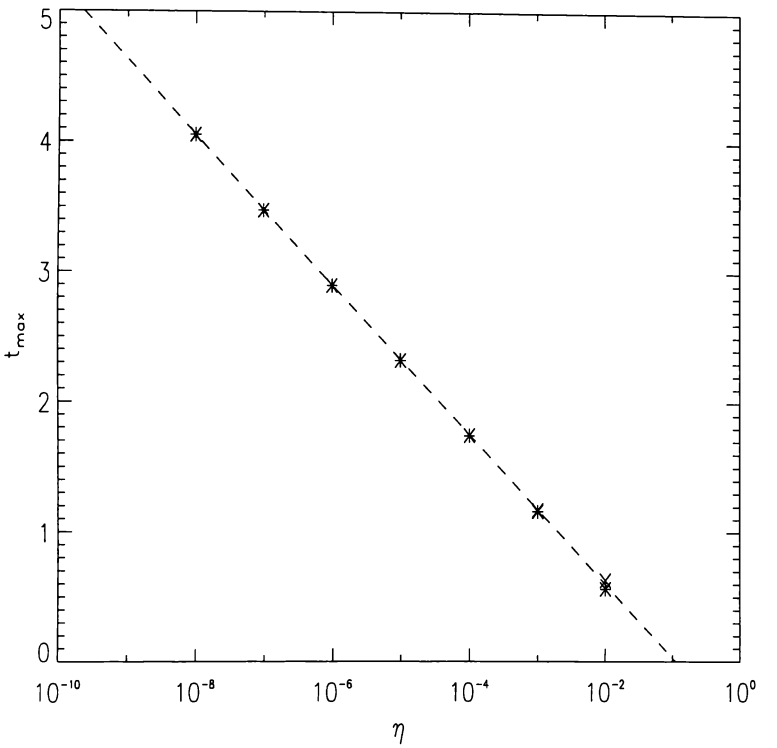


Figure 7.2a. Graph of $t_{\max}$ versus η with $\beta = 1.0$ for two initial conditions.

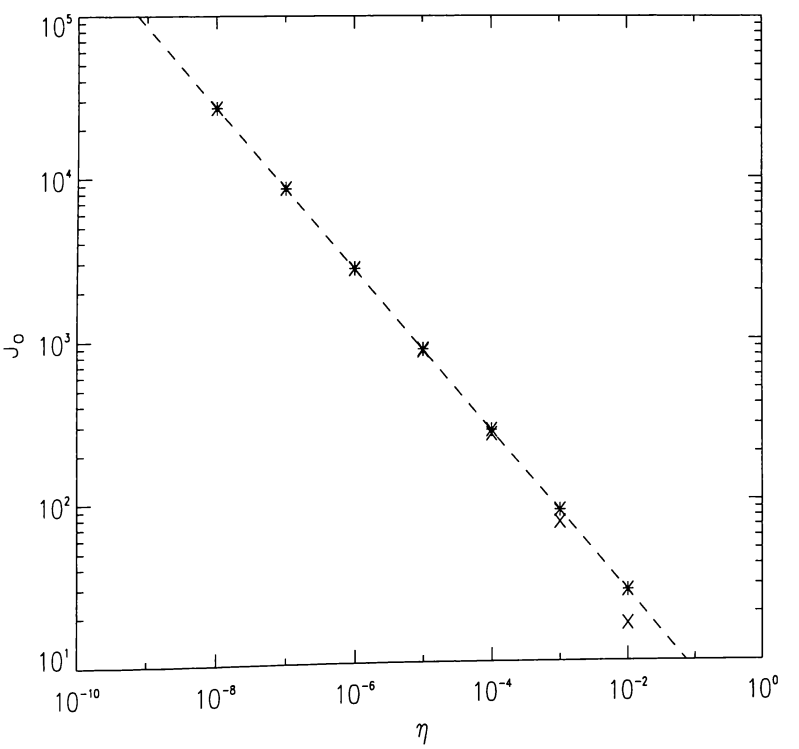


Figure 7.2b. Graph of J_0 versus η with $\beta = 1.0$ for two initial conditions.

while the scaling of l implies

$$B_{\text{sheet}} \sim \eta^0.$$

Figure 7.2 plots (a) $t_{\max}$ versus η and (b) J_0 versus η from a systematic series of numerical simulations – the details of the code are given in the next section. Obviously the scalings estimated above are in excellent agreement.

Consider now the plasma pressure. As $p > 0$ it follows from (7.5) that $p_0 = O(1)$. Hence solutions with $|\alpha| = |\beta|$ have a realistic pressure on the outer boundary. This contrasts the previous $\beta = 0$ solutions where $p_0 = O(\frac{1}{\eta})$.

7.4.3 Magnetic Reconnection Rates

Our measure of energy release can now be calculated. The rate of flux annihilation at the neutral point scales as

$$\frac{\partial \psi}{\partial t} = \eta J_0 \sim \eta^{1/2},$$

and Ohmic dissipation rate scales as

$$W_\eta \approx \eta J_0^2 L l \sim \eta^{1/2},$$

which both indicate slow energy releases.

7.5 The $|\alpha| \neq |\beta|$ Case

7.5.1 The Outer Solution

We now establish an outer solution for the $|\alpha| \neq |\beta|$ case. Neglecting the resistive term gives

$$f_t + x(\alpha f_x - \beta g_x) - 2(\alpha f - \beta g) = 0, \tag{7.14}$$

$$g_t + x(\alpha g_x - \beta f_x) = 0, \tag{7.15}$$

where α and β are both finite.

We differentiate both equations with respect to x to obtain

$$u_t + x(\alpha u_x - \beta b_x) - \alpha u + \beta b = 0,$$

$$b_t + x(\alpha b_x - \beta u_x) + \alpha b - \beta u = 0,$$

where

$$u = -f_x, \qquad b = -g_x.$$

Introduction of the co-ordinates

$$\tau = t, \qquad \xi = \ln(x) - \alpha t,$$

gives

$$u_\tau - \beta b_\xi - \alpha u + \beta b = 0,$$

$$b_\tau - \beta u_\xi + \alpha b - \beta u = 0.$$

One can eliminate either dependent variable, say u, to obtain

$$b_{\tau\tau} = \beta^2 b_{\xi\xi} + (\alpha^2 - \beta^2) b, \tag{7.16}$$

which is an example of the Klein-Gordon equation and also holds for u.

Our two special cases are readily apparent from (7.16). If $\beta = 0$ then solutions take the form

$$b = A(\xi)\mathrm{e}^{-\alpha\tau} + B(\xi)\mathrm{e}^{+\alpha\tau} = A^*(x\mathrm{e}^{-\alpha t})\mathrm{e}^{-\alpha t} + B^*(x\mathrm{e}^{-\alpha t})\mathrm{e}^{+\alpha t},$$

where A, A^*, B, B^* are arbitrary functions. If $|\alpha| = |\beta|$ then we have

$$b = C(\xi - \alpha\tau) + D(\xi + \alpha\tau) = C^*(x\mathrm{e}^{-2\alpha t}) + D^*(x),$$

with C, C^*, D, D^* being arbitrary functions. Both these solutions can be easily deduced from our analysis in the previous sections.

Let us take the Fourier transform of (7.16) which gives

$$\bar{b}_{\tau\tau} = [\alpha^2 - \beta^2(1 + k^2)]\bar{b}, \tag{7.17}$$

where

$$\bar{b}(k, \tau) = \int_{-\infty}^{+\infty} b(\xi, \tau)\mathrm{e}^{ik\xi}\mathrm{d}\xi.$$

The solution of (7.17) is

$$\bar{b} = F(k)\mathrm{e}^{+\mu(k)\tau} + G(k)\mathrm{e}^{-\mu(k)\tau}, \tag{7.18}$$

where

$$\mu(k) = \sqrt{\alpha^2 - \beta^2(1 + k^2)},$$

while F and G are functions given by the initial conditions. As $\mu^2 \geq 0$ we also have the condition $|\alpha| \geq |\beta|$.

Inverting (7.18) finally gives

$$b(\xi, \tau) = \int_{-\infty}^{+\infty} [A(k)\mathrm{e}^{+\mu(k)\tau} + B(k)\mathrm{e}^{-\mu(k)\tau}]\mathrm{e}^{-ik\xi}\mathrm{d}k, \tag{7.19}$$

as our general solution.

Our solution for b in (7.19) provides little information about the energy release. Analytical solutions cannot be determined for $|\alpha| \neq |\beta|$ so a more elaborate technique for establishing scalings for $t_{\max}$ and J_0 is required. Thus we give an approximate analysis then use numerical simulations to verify our proposed scalings.

7.5.2 A Numerical Approach

We now outline our numerical approach for justifying the approximate analysis in the following section. A finite-difference code was developed to model (7.3) and (7.4). In particular we employ a predictor-corrector method to simultaneously update both f and g. We further remark that a uniformly spaced grid was found to be sufficient.

We shall initiate our simulations with two extreme initial conditions. Namely we take

$$f(x,0) = 0, \qquad g(x,0) = \mathrm{e}^{-x^2},$$

which corresponds to a magnetic field perturbation and

$$f(x,0) = \mathrm{e}^{-x^2}, \qquad g(x,0) = 0,$$

which corresponds to a flow perturbation.

An exponential profile is chosen so comparisons with our $\beta = 0$ solution in Section 7.3 can be drawn. The outer boundary was then chosen so that setting $f = 0$ and $g = 0$ would not introduce spurious boundary effects. We also mention that $\alpha = -1$ for all simulations.

Our goal here is to establish how β influences the rate of energy release. Therefore we vary β and study how $t_{\max}$ and J_0 change as $\eta \to 0$. In practise the resolution for a given value of β and η was systematically lowered until $t_{\max}$ and J_0 were accurate to three significant figures. Obviously the accuracy of our numerical results is satisfactory.

7.5.3 Diagnostics

Our aim here is to construct an approximate theory that gives scalings for $t_{\max}$ and J_0 so the energy release can be calculated. We shall then confirm these scalings with a series of computer simulations using the method detailed above.

We first introduce the new variable h defined by

$$f = \frac{\beta}{\alpha} g + h, \tag{7.20}$$

and rewrite the ideal ($\eta = 0$) equations as

$$h_t + x\left(\frac{\alpha^2 + \beta^2}{\alpha}\right) h_x - 2\alpha h = \frac{\beta}{\alpha^2}(\alpha^2 - \beta^2) g_x, \tag{7.21}$$

$$g_t + x(\frac{\alpha^2 - \beta^2}{\alpha})g_x = \beta x h_x. \tag{7.22}$$

The form of (7.21) and (7.22) indicate that the profiles of h and g propagate inwards at different speeds. The first current peak results from the localisation of h while the second results from the localisation of g. This naturally implies that two current maximums will occur.

It is readily apparent that $\beta = 0$ and $|\alpha| = |\beta|$ define the two extreme choices of β. In either instance, the term on the right-hand side of (7.21) becomes zero and outer solutions for h and then g can be readily determined. This fact suggests that approximate scalings may be obtained by neglecting this term.

We now determine approximate theories for $|\beta| \ll |\alpha|$ and $|\beta| \approx |\alpha|$ individually.

(i) $|\beta| \ll |\alpha|$

This choice of parameters corresponds to the second current peak. We first recognise that the term on the right-hand side of (7.22) can be neglected. Thus we obtain

$$g_t + x(\frac{\alpha^2 - \beta^2}{\alpha})g_x = 0,$$

which can be solved by the method of characteristics to give

$$g = g_0(x\mathrm{e}^{-\frac{(\alpha^2-\beta^2)}{\alpha}t}), \tag{7.23}$$

where g_0 is the initial distribution of g. Obviously (7.23) holds until the incoming profile of g reaches the neutral line.

We can now determine diagnostic scalings for $t_{\max}$ and J_0. The build-up of current will be arrested when

$$g_t \approx \eta g_{xx}, \tag{7.24}$$

along the neutral line.

After substitution of (7.23), we find that (7.24) is satisfied when

$$t_{\max} \sim \frac{\alpha}{2(\alpha^2 - \beta^2)} \ln(\eta),$$

and back-substituting this approximation into (7.24) yields

$$J_0 \sim \eta^{-1},$$

where J_0 is the second current maximum.

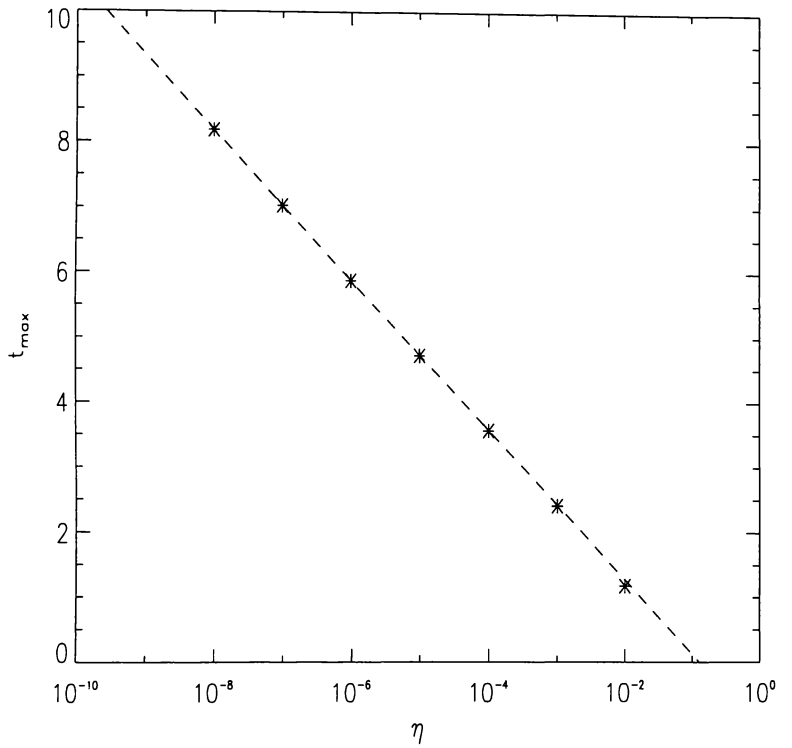


Figure 7.3a. Graph of $t_{\max}$ versus η with $\beta = 0$.

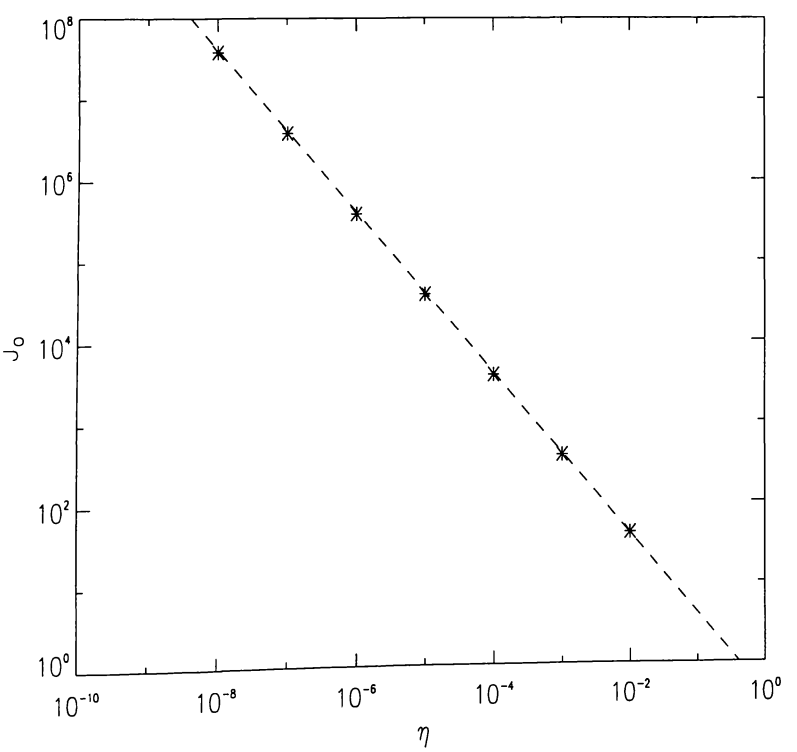


Figure 7.3b. Graph of J_0 versus η with $\beta = 0$.

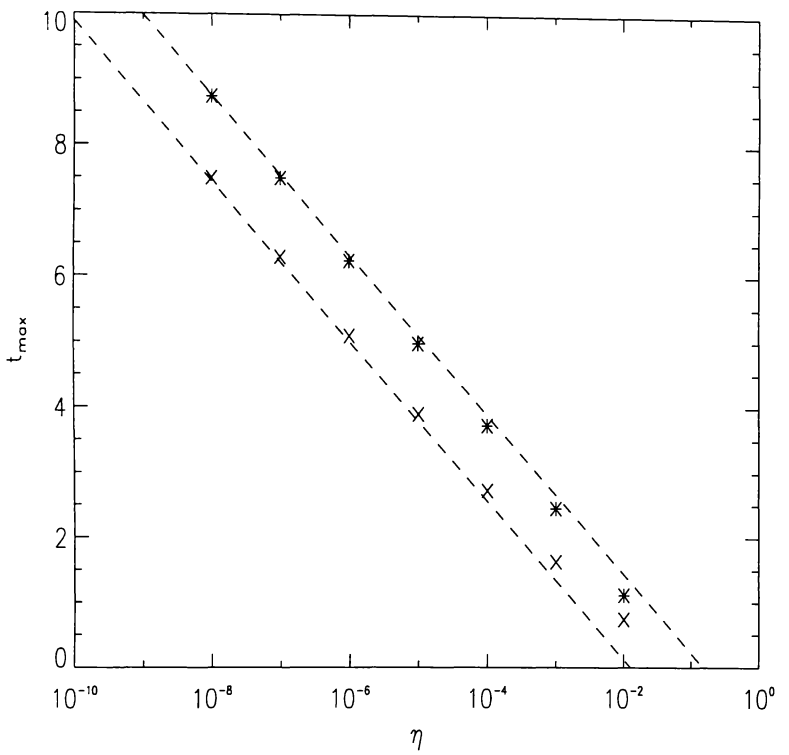


Figure 7.4a. Graph of $t_{\mathbf{max}}$ versus η for second current peak with $\beta = 0.25$ for two initial conditions.

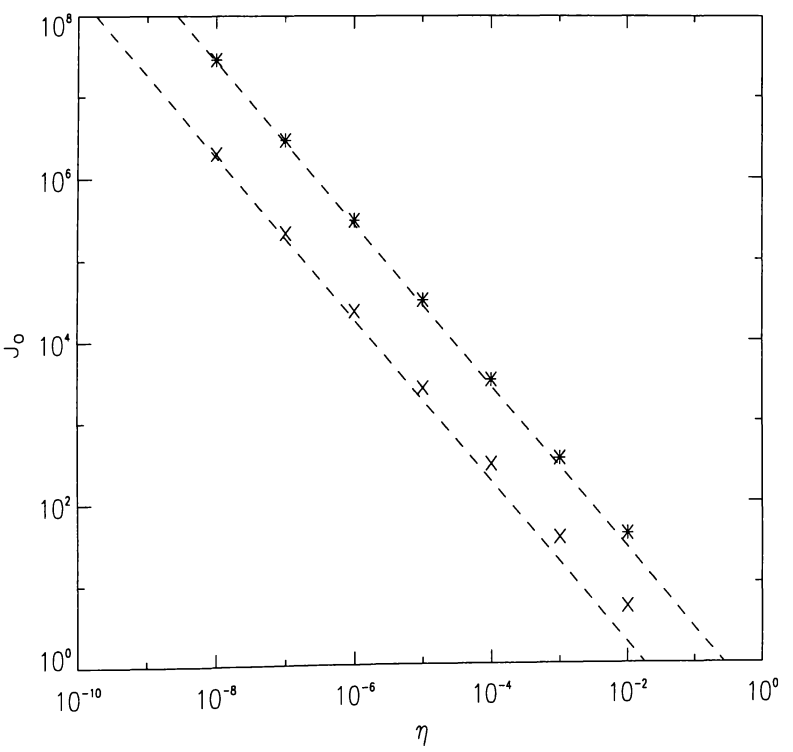


Figure 7.4b. Graph of J_0 versus η for second current peak with $\beta = 0.25$ for two initial conditions.

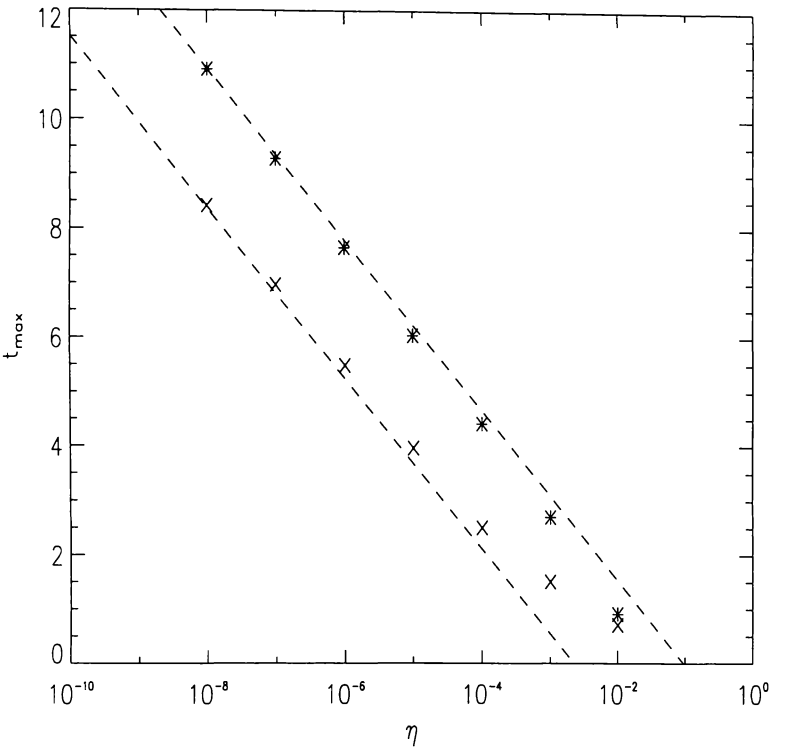


Figure 7.5a. Graph of t_{max} versus η for second current peak with $\beta = 0.5$ for two initial conditions.

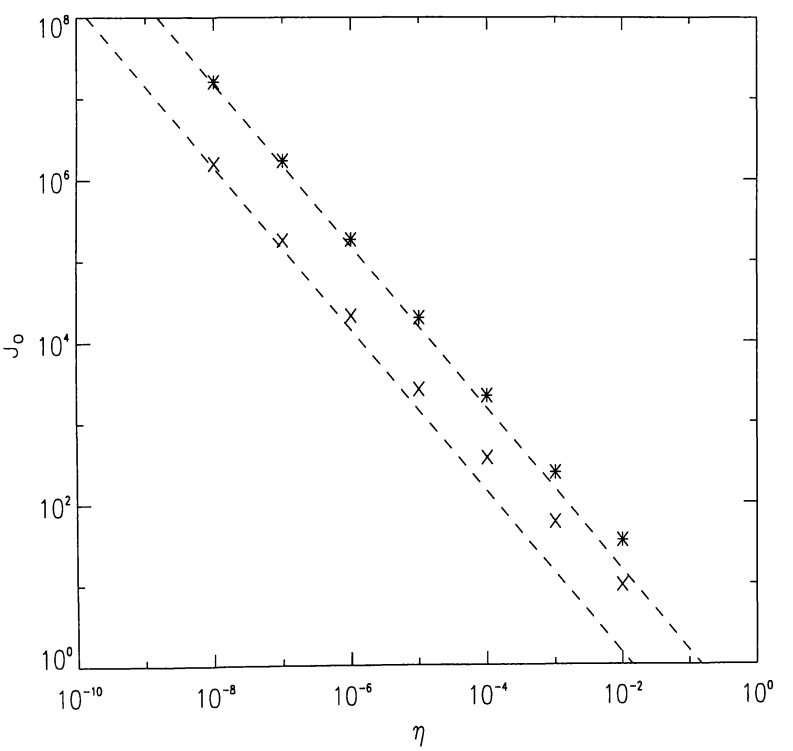


Figure 7.5b. Graph of J_0 versus η for second current peak with $\beta = 0.5$ for two initial conditions.

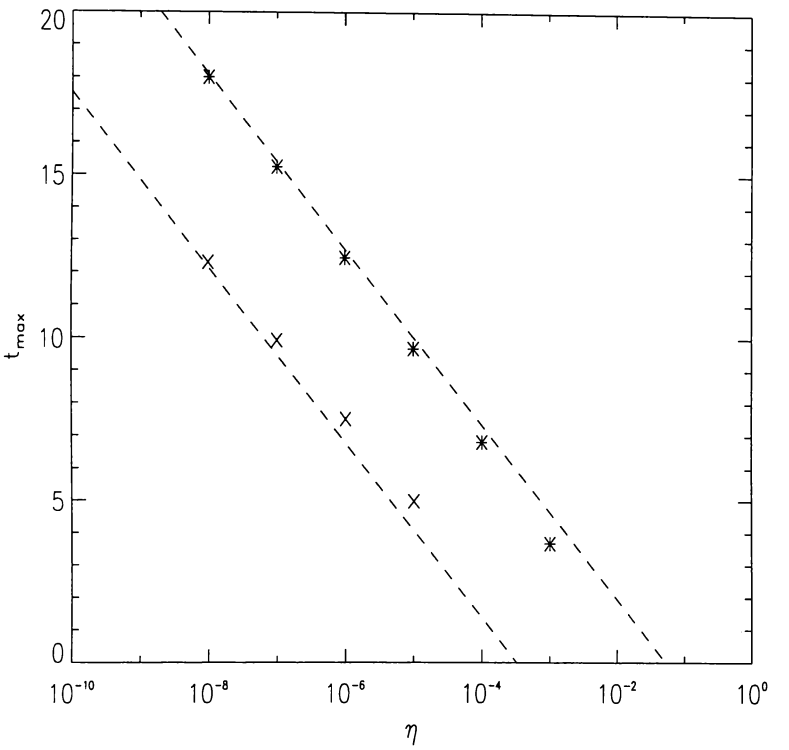


Figure 7.6a. Graph of t_{max} versus η for second current peak with $\beta = 0.75$ for two initial conditions.

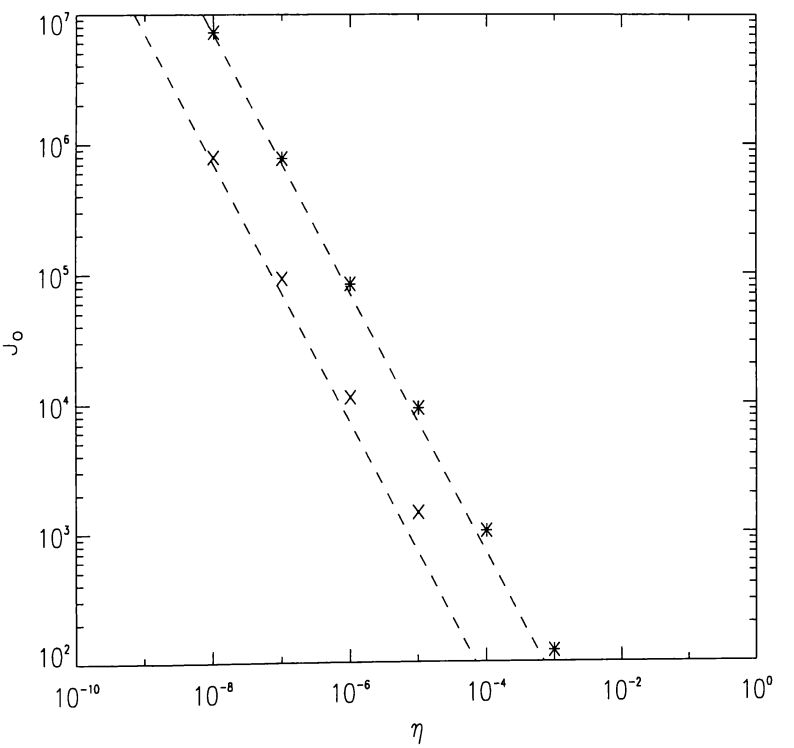


Figure 7.6b. Graph of J_0 versus η for second current peak with $\beta = 0.75$ for two initial conditions.

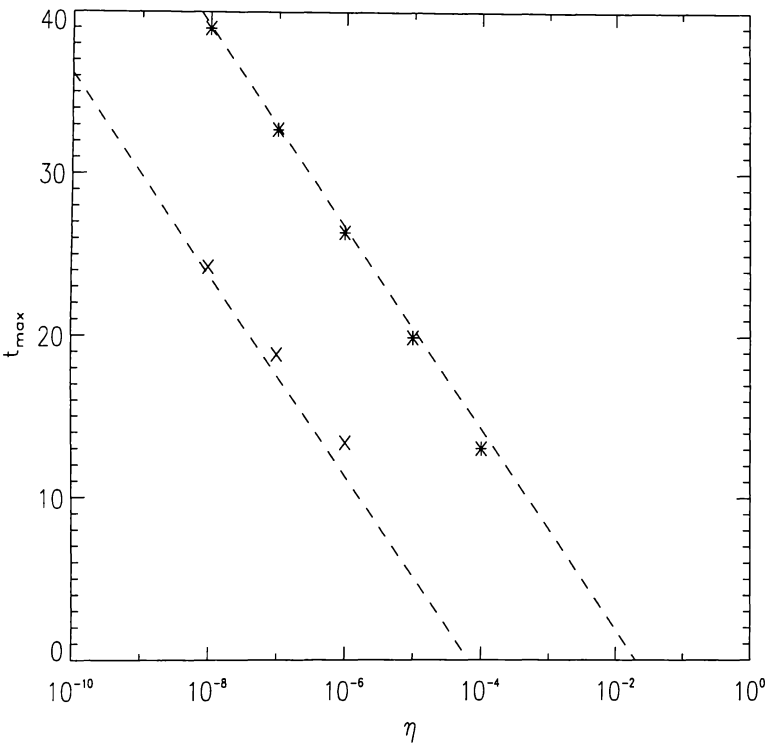


Figure 7.7a. Graph of t_{max} versus η for second current peak with $\beta = 0.9$ for two initial conditions.

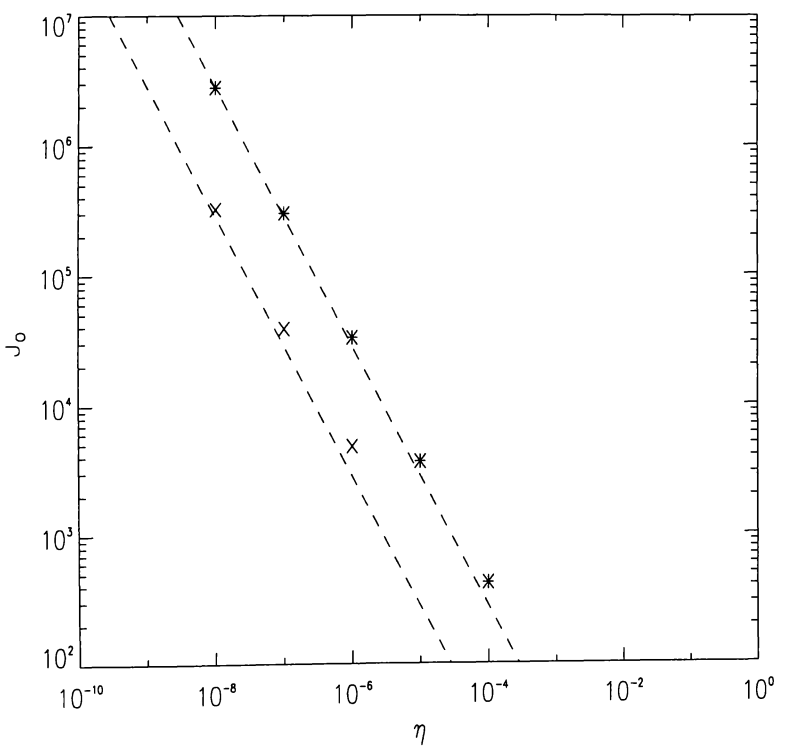


Figure 7.7b. Graph of J_0 versus η for second current peak with $\beta = 0.9$ for two initial conditions.

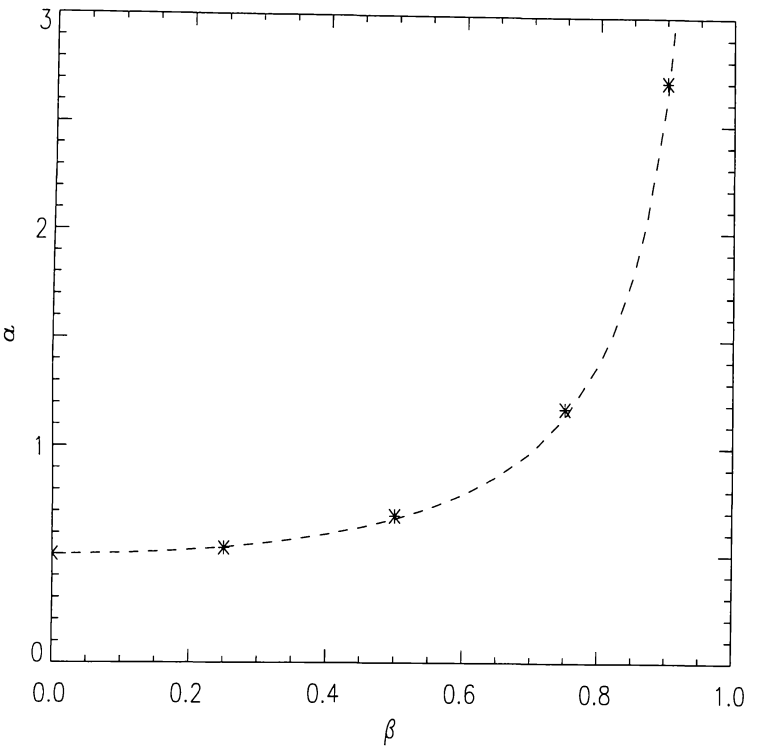


Figure 7.8. Graph of a versus β for second current peak.

Figures 7.3 to 7.7 plot (a) $t_{\max}$ versus η and (b) J_0 versus η for $\beta = 0, 0.25, 0.5, 0.75, 0.9$ for the second peak. Here * signifies a result from our first set of initial conditions while $\times$ denotes a result from our second set of initial conditions. We point out that missing symbols are due to the first current maximum overwhelming this current maximum.

Our approximate scalings for $t_{\max}$ and J_0 are indicated by the dashed lines in Figures 7.2 to 7.7. The dashed lines in the top panels depict the lines

$$t_{\max} = a \ln(\eta) + b,$$

where a and b are adjusted to give an optimal fit in the limit of small η – note that the β dependency has not been taken into account yet. These diagrams confirm the $\ln(\eta)$ dependence for $t_{\max}$.

The dashed lines in the bottom panels depict the lines

$$J_0 = c\eta^{-1} + d,$$

where c and d are adjusted to give an optimal fit in the limit of small η. Clearly our approximate theory gives reliable scalings – even for relatively large values of β.

In Figure 7.8 we plot a versus β. Our approximate theory implies

$$a = \frac{\alpha}{2(\alpha^2 - \beta^2)},$$

which has been signified by a dashed line. Again we have an excellent agreement with our numerical results.

For completeness we remark that

$$B_{\text{sheet}} \sim \eta^{-1/2},$$

by applying the scaling of l determined earlier.

The plasma pressure p must be positive so (7.5) implies

$$p_0 = O(\eta^{-1}),$$

which does seem physically unreasonable – we discuss this feature later.

(ii) $|\beta| \approx |\alpha|$

The localisation of h will induce an earlier current maximum. On neglecting the right-hand side of (7.21) we have

$$h_t + x(\frac{\alpha^2 + \beta^2}{\alpha})h_x - 2\alpha h = 0,$$

which can be solved by the method of characteristics to give

$$h = h_0(x\mathrm{e}^{-\frac{(\alpha^2+\beta^2)}{\alpha}t})\mathrm{e}^{2\alpha t},$$

where h_0 denotes the initial distribution of h.

When the localisation of h reaches the neutral line we have

$$g_{xx} \approx -\frac{\alpha}{\beta}h_{xx}, \tag{7.25}$$

from (7.20).

Equation (7.22) indicates that the build-up of current will be arrested when

$$\eta g_{xx} \approx \beta x h_x, \tag{7.26}$$

along the neutral line.

Substituting (7.25) into (7.26) gives

$$t_{\max} \approx \frac{\alpha}{2(\alpha^2 + \beta^2)}\ln(\eta),$$

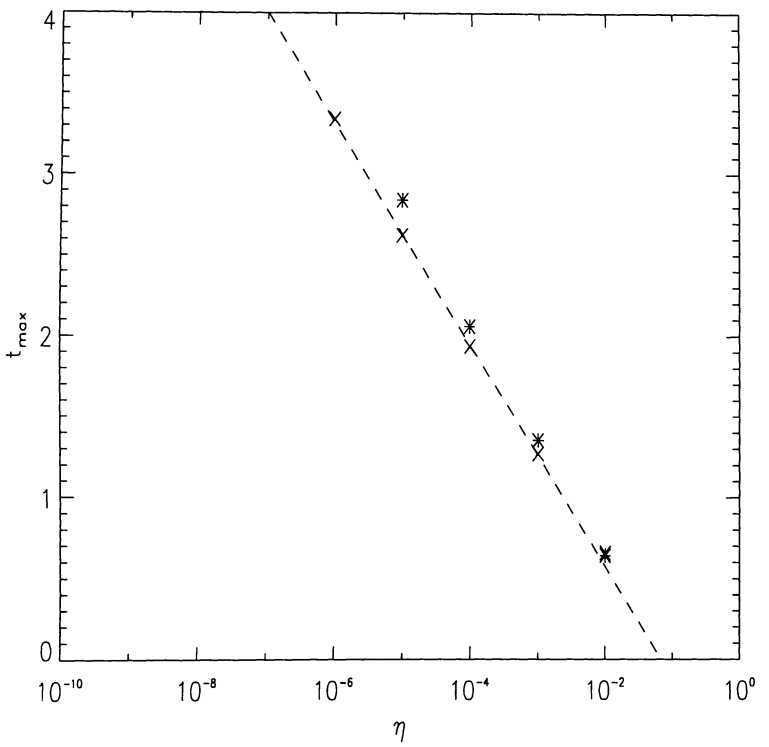


Figure 7.9a. Graph of t_{max} versus η for first current peak with $\beta = 0.85$ with two initial conditions.

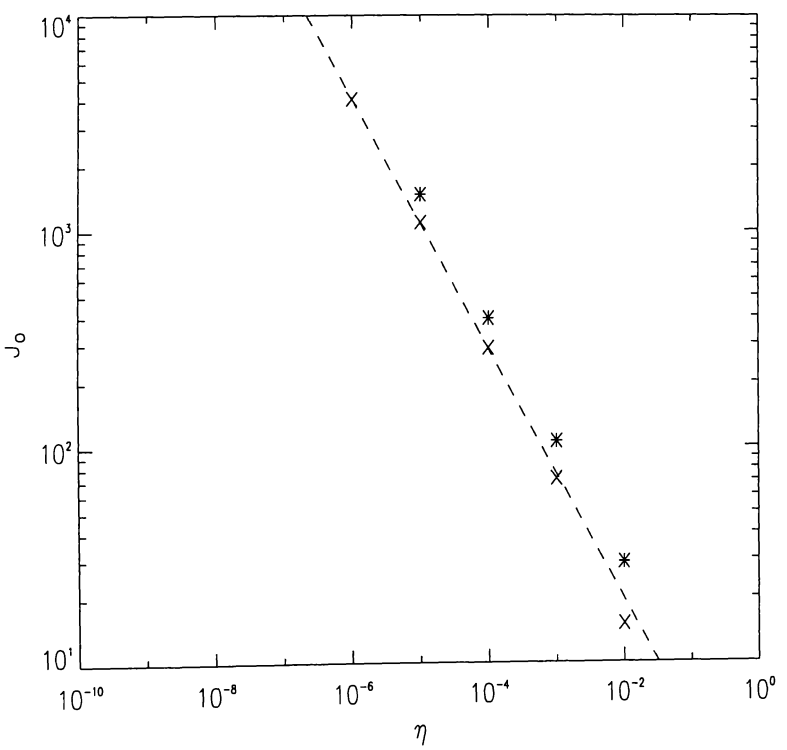


Figure 7.9b. Graph of J_0 versus η for first current peak with $\beta = 0.85$ with two initial conditions.

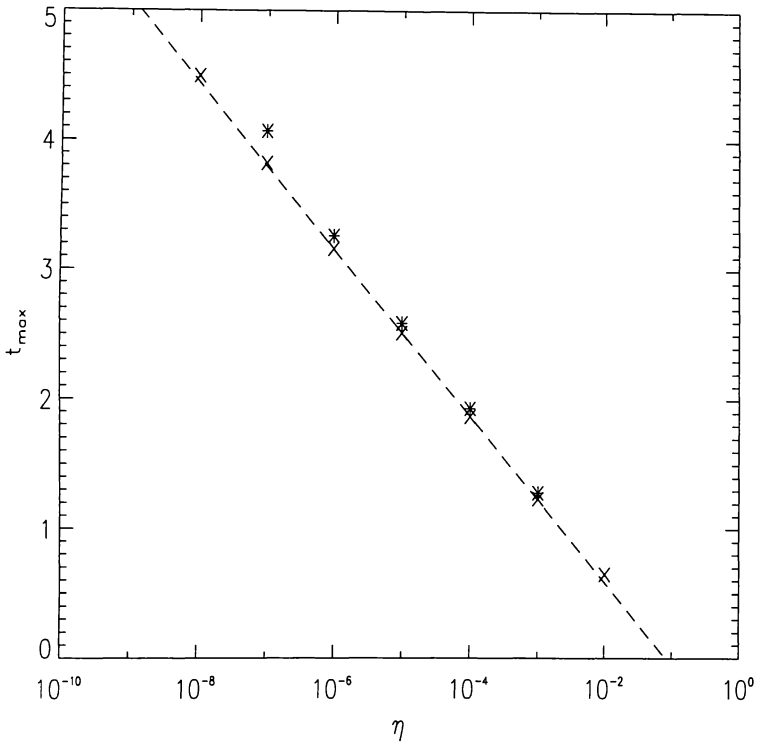


Figure 7.10a. Graph of $t_{\mathbf{max}}$ versus η for first current peak with $\beta = 0.90$ for two initial conditions.

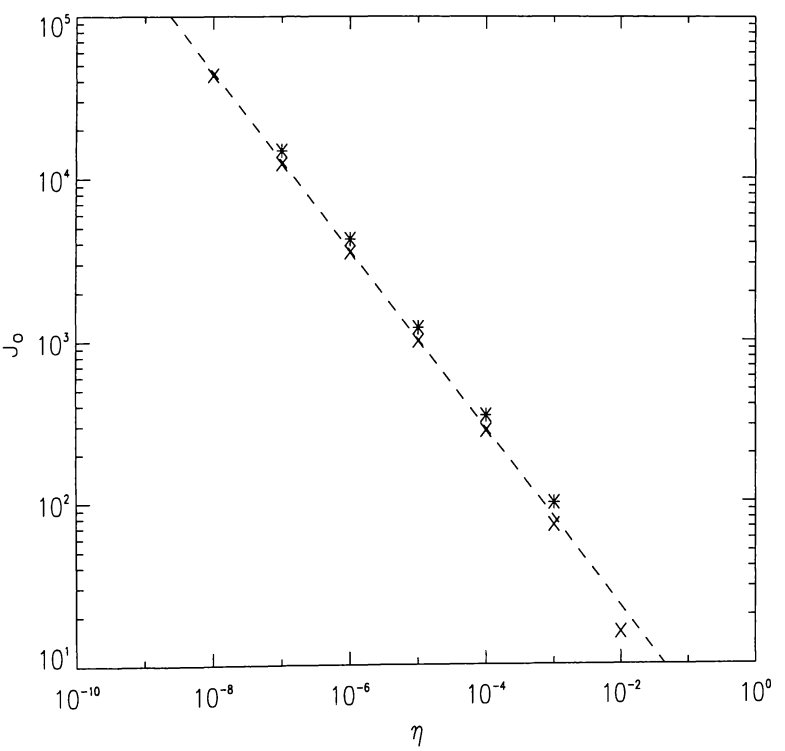


Figure 7.10b. Graph of J_0 versus η for first current peak with $\beta = 0.90$ for two initial conditions.

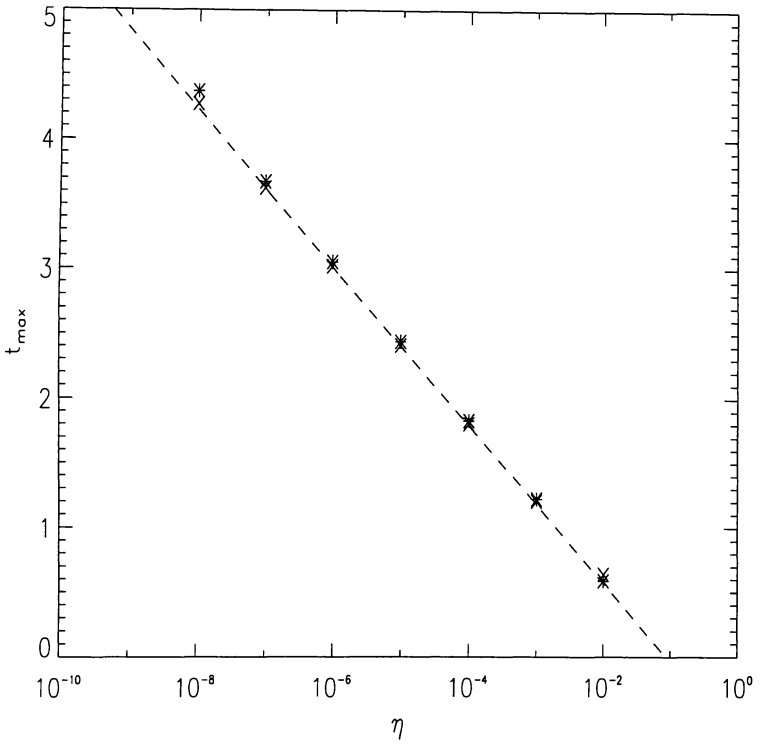


Figure 7.11a. Graph of $t_{\max}$ versus η for first current peak with $\beta = 0.95$ for two initial conditions.

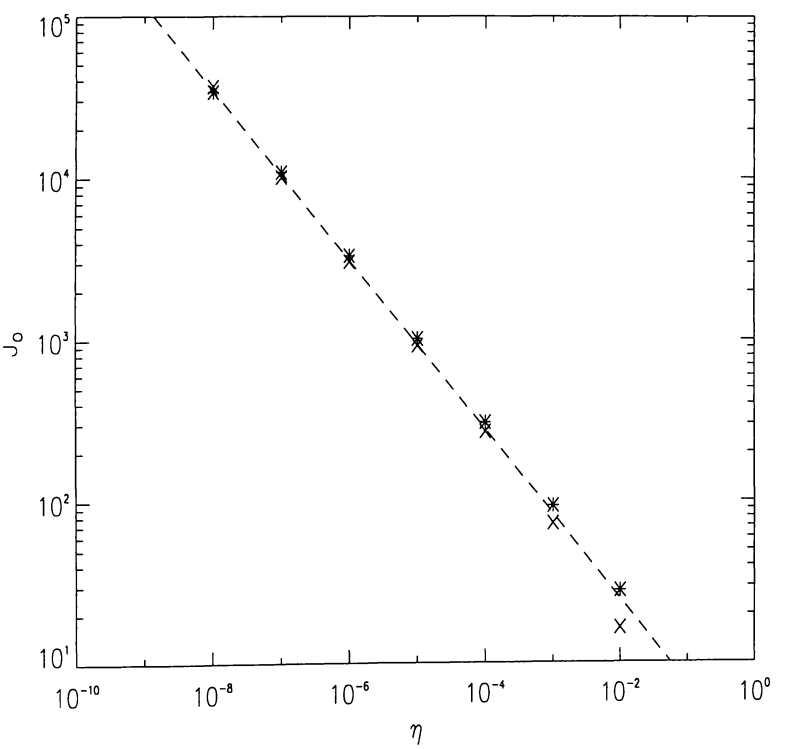


Figure 7.11b. Graph of J_0 versus η for first current peak with $\beta = 0.95$ for two initial conditions.

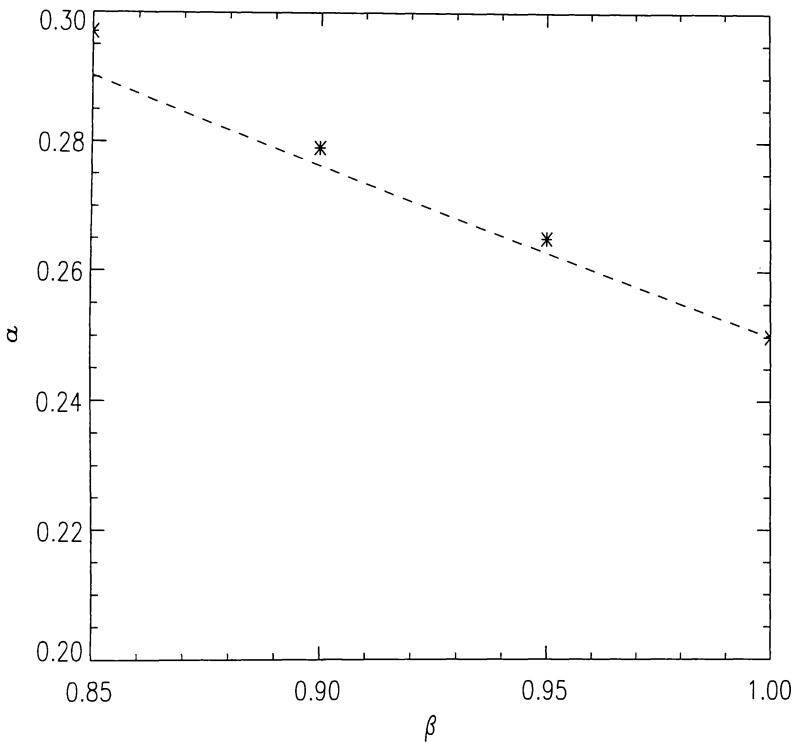


Figure 7.12a. Graph of a versus β for first current peak.

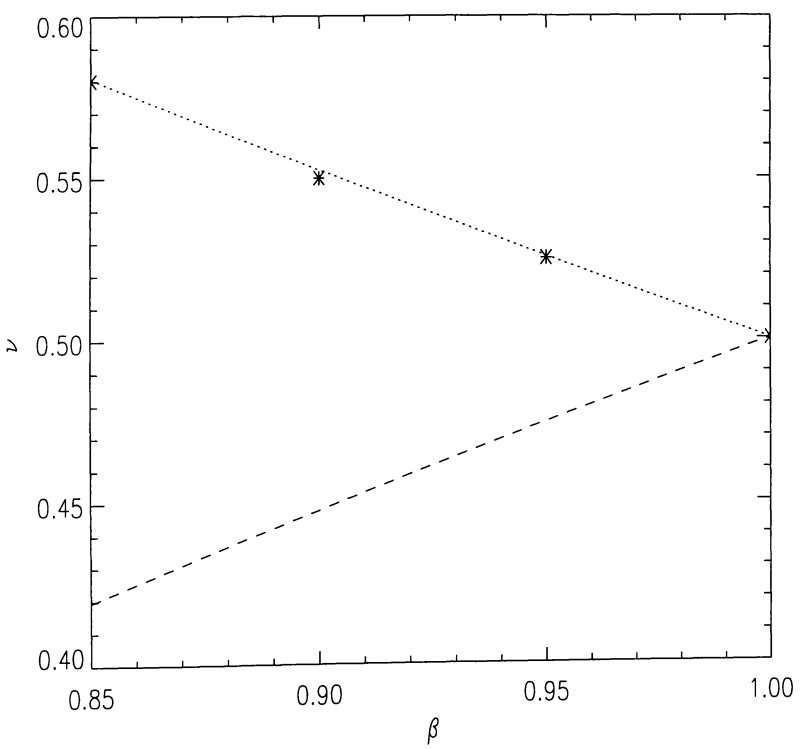


Figure 7.12b. Graph of ν versus β for first current peak.

and back-substitution into (7.26) then implies

$$J_0 \sim \eta^{-\frac{\beta^2}{\alpha^2+\beta^2}},$$

where J_0 is the first current maximum.

Figures 7.9 to 7.11 plot (a) $t_{\max}$ versus η and (b) J_0 versus η for $\beta = 0.85, 0.90, 0.95$ for the first peak. The * and $\times$ notations are defined as above. It is noted that scalings are less certain here as the second peak swamps the first peak as η approaches realistic values. This subsequently gives a very restricted range of β data points for the first peak. Note that missing symbols result from the second current maximum overwhelming the first current maximum.

Again the dashed lines in the top panels are

$$t_{\max} = a\ln(\eta) + b,$$

where a and b are adjusted to give an optimal fit. This diagram readily illustrates the $\ln(\eta)$ dependence as $\eta \to 0$.

Meanwhile the dashed lines in the bottom panels are

$$J_0 = c\eta^{-\nu} + d,$$

where we vary c, d and ν to optimise the fit. Clearly this power-law dependence gives an excellent fit for small values of η.

The values of a from our best-fit lines are plotted in Figure 7.12a. Our approximate theory has

$$a = \frac{\alpha}{2(\alpha^2+\beta^2)},$$

which indicated by the dashed line. This diagram shows that our approximate scaling is reasonable.

Values of ν from our best-fit lines are presented in Figure 7.12b. Our approximate theory implies

$$\nu \approx -\frac{\beta^2}{\alpha^2+\beta^2},$$

which has been denoted by a dashed line. Here we find that our best-fit ν values give a poor result. As a point of interest we have also shown

$$\nu \approx -\frac{\alpha^2}{\alpha^2+\beta^2},$$

with a dotted line as this scaling seems to give a satisfactory fit.

The reasoning behind our inaccurate approximation for J_0 must be due to discarding the term on the right-hand side of (7.21). This component must no longer be negligible at the time of current maximum if $|\alpha| \approx |\beta|$. However we will shortly demonstrate that this current maximum gives a slow energy release. Furthermore the second current peak 'swamps' the first current peak as $\eta \to 0$. Hence we need not be overly concerned with our poor estimation for J_0 as the other current maximum seems more important.

The scaling of the magnetic field entering the sheet is

$$B_{\text{sheet}} \sim \eta^{\frac{\alpha^2-\beta^2}{2(\alpha^2+\beta^2)}},$$

where we have used the scaling of l calculated earlier.

Plasma pressure p cannot be negative so (7.5) implies

$$p_0 = O(\eta^{\frac{\alpha^2-\beta^2}{\alpha^2+\beta^2}}).$$

This gives a positive power on η for any finite β which seems physically unreasonable.

7.5.4 Magnetic Reconnection Rates

Now our two measures of energy release can be determined. For the first current peak we have

$$\frac{\partial \psi}{\partial t} = \eta J_0 \sim \eta^{\frac{\alpha^2}{\alpha^2+\beta^2}},$$

and

$$W_\eta \approx \eta J_0^2 L l \sim \eta^{\frac{3\alpha^2-\beta^2}{2(\alpha^2+\beta^2)}},$$

which are both slow for finite values of β.

For the second current peak we have

$$\frac{\partial \psi}{\partial t} = \eta J_0 \sim \eta^0,$$

which is fast and

$$W_\eta \approx \eta J_0^2 L l \sim \eta^{-1/2},$$

which is ultra-fast.

7.6 Discussion

The analytical nature of our solutions means that problems over determining suitable boundary conditions have been alleviated. Only the external parameters α, β need to be specified. What is more, the outer boundaries are open-flow. It is clear that plasma is continuously entering and exiting the modelled system.

We emphasise that adopting the traditional inner symmetries depress these exact solutions. This seemingly implies that the traditional symmetries only handicap the derivation of two dimensional reconnection solutions. Hence magnetic reconnection may need a certain lack of symmetry in the magnetic field and plasma flow.

Our dynamic solutions comprise an equilibrium component and a time-dependent shear component. The presence of η means that the initial shear components are eventually lost via an energy release along the neutral line. We now summarise the energy release and nature of the background plasma pressure for each case.

The case of $\beta = 0$ has both components moving together as a single pulse. This collective pulse is annihilated along the neutral line and it was demonstrated that the resulting energy release is fast. We also showed that the background plasma pressure needed to be exceedingly large *i.e.* $p_0 = O(\frac{1}{\eta})$.

The case $|\alpha| = |\beta|$ has one pulse moving inward while the other remains stationary. The incoming pulse drives a reconnective process at the neutral point and we showed that the energy release is slow. Meanwhile the remaining pulse experiences static diffusion which produces an extremely slow energy release for coronal values of η. The background plasma pressure was $p_0 = O(1)$.

The general case $|\alpha| \neq |\beta|$ has two inwardly travelling pulses which each give rise to a current maximum. We demonstrated that only the second current maximum gives a fast rate of energy release. Again the background plasma pressure was found to be extremely large *i.e.* $p_0 = O(\frac{1}{\eta})$.

7.7 Extending to Three Dimensions

As with the steady-state analysis, our two-dimensional solutions can be extended to three dimensions. The incompressible MHD equations can be expressed in three dimensions as

$$\omega_t + (\mathbf{v}.\nabla)\omega - (\omega.\nabla)\mathbf{v} = (\mathbf{B}.\nabla)\mathbf{J} - (\mathbf{J}.\nabla)\mathbf{B}, \tag{7.27}$$

$$\mathbf{B}_t + (\mathbf{v}.\nabla)\mathbf{B} - (\mathbf{B}.\nabla)\mathbf{v} = \eta\nabla^2\mathbf{B}, \tag{7.28}$$

where

$$\nabla.\mathbf{B} = 0, \qquad \nabla.\mathbf{v} = 0,$$

and

$$\mathbf{J} = \nabla \times \mathbf{B}, \qquad \omega = \nabla \times \mathbf{v}.$$

Once again solutions with fan and spine current distributions can be derived. These are natural extensions of the steady-state solutions of fan and spine reconnection already outlined in Chapter 6.

(i) Fan Solutions

In keeping with our two-dimensional analysis we take

$$\mathbf{v} = \mathbf{P} + \mathbf{q}(x,t),$$

$$\mathbf{B} = \lambda\mathbf{P} + \mathbf{Q}(x,t),$$

where the shear components are

$$\mathbf{q} = V(x,t)\hat{\mathbf{y}} + W(x,t)\hat{\mathbf{z}},$$

$$\mathbf{Q} = Y(x,t)\hat{\mathbf{y}} + Z(x,t)\hat{\mathbf{z}},$$

and

$$\mathbf{P} = \alpha[-x\hat{\mathbf{x}} + \kappa y\hat{\mathbf{y}} + (1-\kappa)z\hat{\mathbf{z}}],$$

is our potential component. Here λ, α, κ denote arbitrary constants and our two-dimensional solutions correspond to setting $\kappa = 1$.

Substituting these forms into (7.27) and (7.28) gives

$$V_t - \alpha x V_x + \alpha\kappa V = -\alpha\lambda x Y_x + \alpha\lambda\kappa Y,$$

$$W_t - \alpha x W_x + \alpha(1-\kappa)W = -\alpha\lambda x Z_x + \alpha\lambda(1-\kappa)Z,$$

and

$$Y_t - \alpha x[Y - \lambda V]_x - \alpha\kappa[Y - \lambda V] = \eta Y_{xx},$$

$$Z_t - \alpha x[Z - \lambda W]_x - \alpha(1-\kappa)[Z - \lambda W] = \eta Z_{xx}.$$

Thus a current sheet develops then decays away in the plane $x = 0$ – a current fan.

(ii) Spine Solutions

We now take the trial forms

$$\mathbf{v} = \mathbf{P} + q(y,z,t)\hat{\mathbf{x}},$$

$$\mathbf{B} = \lambda\mathbf{P} + Q(y,z,t)\hat{\mathbf{x}},$$

where $\mathbf{P}$ and λ are defined above.

Substituting these into (7.27) and (7.28) yields

$$q_t - \alpha[q - \lambda Q] + \alpha\kappa y[q - \lambda Q]_y + \alpha(1-\kappa)z[q - \lambda Q]_z = 0,$$

$$Q_t + \alpha[Q - \lambda q] + \alpha\kappa y[Q - \lambda q]_y + \alpha(1-\kappa)z[Q - \lambda q]_z = \eta\nabla^2 Q.$$

This family of solutions describe an evolution of current along the x-axis – a current spine.

We have detailed a systematic method for obtaining fan and spine solutions. Both approaches to deriving time-dependent reconnection are under investigation.

7.8 Summary

This chapter has extended our steady-state solutions of Chapter 6 to incorporate time-dependency. We emphasise that *no* analytical solutions of dynamical magnetic reconnection have been discovered previously. Here we simply allowed the shear components of our earlier steady-state solutions to be time-dependent. Again the governing equations simplified dramatically and analytical solutions were readily attained.

The traditional inner symmetries of the magnetic field and plasma flow have again been broken. This naturally results in a fundamental difference between the two separatrices of the magnetic field. Plasma motions across one separatrix induce the formation of a current sheet along the other separatrix. Both our steady-state and time-dependent solutions of reconnection imply that separatrices should not be regarded as equivalent.

A concern with these time-dependent solutions is due to the unreasonable nature of the plasma pressure. The background pressure is exceptionally large for typical values of η – unless $|\alpha| = |\beta|$. This force is required to maintain the stagnation-point flow and thus drive the reconnection mechanism. It has already been stressed that the corona is considered a low-β plasma.

CHAPTER 8

Conclusions

8.1 Opening Remarks

The widely held belief amongst the scientific community is that solar flares are caused by magnetic reconnection. In particular it is the reconnection of magnetic field lines within the outermost layer of the solar atmosphere, namely the corona, that generates the energy release. The key objective of this thesis was to develop a reconnection model, based upon the magnetohydrodynamic (MHD) equations, that can demonstrate the characteristic features of this energy release.

The goal of understanding how magnetic reconnection 'works' is far from being achieved. Existing model are often based on approximations and simplifications which are not rigorously justified. A systematic review of existing reconnection models is given in Chapter 3. Although these models are highly idealised, they still provide valuable insight into the reconnection mechanism and pin-points areas for further study.

8.2 Discussion of Presented Work

We now review the models of magnetic reconnection presented in this thesis. Results from computer simulations of two compressible models were presented in Chapter 4. Our numerical findings imply that an analytical approach is needed for gaining a better understanding of reconnection. Thus Chapters 5 to 7 concentrated on developing *analytical* solutions of the MHD equations.

The analytical nature of our approximate solutions in Chapter 5 and exact solutions in Chapters 6 and 7 meant that problems over determining suitable boundary conditions were alleviated. A set of external parameters need only be specified *after* solutions have been constructed. Another important advantage of these analytical solutions is the open-flow nature of the boundaries. Unlike our numerical models in Chapter 4, plasma is continuously entering and exiting the reconnective system.

Chapter 4

Our original work began with simulations of two models of time-dependent reconnection. The first model had been previously outlined in DeLuca & Craig (1992) with the second model being a two-dimensional variant of the first. The periodicity of both models made it possible to avoid setting boundary conditions and reduce the modelled domain considerably. This reduction subsequently allowed for greater levels of resolution and so much smaller values of plasma resistivity could be simulated.

We subsequently discovered that reconnection stalled in our two models for coronal values of plasma resistivity. This confirmed the hint of stalling observed, but not confirmed, by DeLuca & Craig (1992) and the prediction of a stalling phenomenon by Biskamp & Welter (1980). Our findings implied that the rate of energy release was too slow for explaining a solar flare. It must be stressed that previous studies have not managed to illustrate that reconnection stalls. In particular, resolution restraints prevented the simulation of sufficiently small resistivities.

Our results showed that a build-up in density at the neutral point created a strong plasma pressure force that acted against the localisation of the magnetic field. We also found that the build-up of the magnetic field entering the sheet saturated at the level of the background magnetic field. This led to stalling as the Lorentz force driving the reconnection could not counter the back-pressure inside the sheet as resistivity declined.

Chapter 5

We next derived approximate solutions from the steady-state MHD equations for an incompressible plasma. Here we follow the approach of Priest & Forbes (1986) and, in particular, Craig & Rickard (1994) by making the opening assumption that plasma velocities were sub-Alfvénic but chose *not* to linearise the resulting equations. An interesting consequence of the sub-Alfvénic approximation was the presence of an arbitrary function in the governing equations. By making a suitable choice of this function, we constructed solutions with fast energy releases. Another outcome was that, under the traditional inner symmetries, outer boundary conditions for the plasma flow were not required.

Several important properties of our sub-Alfvénic solutions were identified. We demonstrated from our analysis that (*i*) the current sheet extends from the neutral point to the outer boundary, (*ii*) the current sheet is strongly one-dimensional, and (*iii*) a vorticity layer overlies the current sheet. Hence shearing motions about the neutral point were an integral feature of our sub-Alfvénic solutions. All these properties are in contrast with the traditional views of two-dimensional reconnection – see Chapters 2 and 3.

One important result of our analysis was that steady-state reconnection cannot occur under the sub-Alfvénic approximation. An intrinsic property of our sub-Alfvénic solutions is that current is uniform along the magnetic field lines. Thus field lines are only, strictly speaking, annihilated along the separatrices of the magnetic field. This result obviously implies that sub-Alfvénic findings are of limited value. Therefore we consider this chapter as a stepping stone for deriving exact solutions of reconnection.

Chapter 6

Exact solutions for steady-state reconnection were derived in this chapter. It must be reiterated that these are the only *exact* solutions of magnetic reconnection. First we considered our sub-Alfvénic findings from Chapter 5 and the solution for annihilation of anti-parallel magnetic fields. Then, by taking suitable trial forms for the magnetic field and plasma flow, the MHD equations were simplified dramatically. Each equation reduced to a one-dimensional equation that could be solved analytically.

The crucial point of our exact reconnection solutions was breaking the traditional four-fold symmetry in the magnetic field and plasma flow – see Chapter 2. In fact considerable progress was attained by not adopting the traditional inner symmetries. It follows from our analysis that a certain lack of symmetry between the magnetic field and plasma flow is likely to be a necessary condition for steady-state reconnection.

Breaking the traditional symmetries resulted in the separatrices of the magnetic field having different properties. Here plasma motions across one separatrix induced the formation of a current sheet along the other separatrix. This naturally suggests that the separatrices of the magnetic field are not necessarily equivalent which contrasts the traditional picture of reconnection.

Our exact solutions incorporated the sub-Alfvénic properties detailed in Chapter 5. The current distribution was one-dimensional and extended from the neutral point to the outer boundary. A vorticity layer overlying the current sheet is another (in-built) feature of our two-dimensional solutions. These findings reaffirm our view that shear flows and global currents are inherent properties of reconnection in steady-state.

Chapter 7

Our steady-state solutions in Chapter 6 were then generalised to include time-dependency. Here we simply allowed the shear components of our trial solutions for the magnetic field and plasma flow to be time-dependent. Again the governing MHD equations reduced to one-dimensional expressions that could be solved semi-analytically. Our time-dependent solutions were qualitatively similar to our previous steady-state solutions.

An initial shear component of the equilibrium solution split into two imploding pulses. Each pulse resulted in the formation of a separate current sheet along the neutral line – thus two current maximums. We then evaluated the reconnection rate for each current maximum. It was found that the first current maximum resulted in a slow energy release while the second current maximum produced a fast energy release. Again each current sheet was one-dimensional and also coincided with a vorticity layer.

One area of concern with our solutions in Chapters 6 and 7 must be noted. It is obvious on physical grounds that the plasma pressure can never be negative. To meet this demand, the background pressure in both our steady-state and time-dependent solutions must be extremely large. This appears physically unrealistic as the $\beta-$value for a typical coronal plasma is expected to be significantly less than unity.

An obvious question that must be answered is – how do the time-dependent simulations in Chapter 4 relate to the time-dependent solutions in Chapter 7. The key difference lies with the background component of the plasma flow. It can be easily verified that the plasma motions will eventually cease in our numerical models. In contrast however, our analytical solutions have a residual flow as time tends to infinity. Here this flow is maintained via the large plasma pressure along the outer boundary.

We can therefore say that the stalling phenomenon in our simulations resulted from lack of large hydromagnetic pressures outside the current sheet. This outcome implies that two-dimensional reconnection will stall for coronal values of the plasma pressure. It now appears that a suitable flare mechanism will stall but only at a level that can account for the observed energy release. Further discussion of this salient issue can be found in Watson & Craig (1996).

8.3 Suggestions for Further Work

The findings presented in this thesis indicate further areas of research. Although our treatment of the reconnection problem concentrated on two dimensions, a three-dimensional mechanism is more realistic. In Chapters 6 and 7 we clearly illustrated how our planar solutions can be easily extended to three dimensions – these solutions are currently being investigated (Craig *et.al.* 1995, Craig & Fabling 1996). However we must emphasise that these three-dimensional solutions were a direct consequence of our two-dimensional findings.

The analytical solutions in Chapters 5, 6 and 7 were all derived for an incompressible plasma. Meanwhile the simulations in Chapter 4 convincingly showed that compressibility plays an important role in the reconnection process. Hence extending our incompressible solutions to an compressible plasma is a desirable next step. Preliminary attempts show that this task is exceedingly difficult - even steady-state solutions.

It must be mentioned that other factors could play a significant role in the solar flare puzzle. Firstly viscous forces may seriously alter the nature of the reconnection mechanism. Secondly non-classical effects due to relativistic velocities or excessively small length-scales may lead to the MHD approximation breaking down. However the stance taken here is that magnetic reconnection under the classical MHD framework must be understood first. Only then should more complicated ingredients be introduced.

REFERENCES

Besser B. P., Biernat H. K. and Rijnbeek R. P. 1990, *Planet. Space Sci.* bf 38, 411.

Besser B. P., Biernat H. K. and Rijnbeek R. P. 1991, *J. Atm. Terr. Phys.* **53**, 1081.

Biskamp D. 1986, *Phys. Fluids* **89**, 1520.

Biskamp D. 1994, *Phys. Rep.* **4**, 237.

Biskamp D. and Welter H. 1980, *Phys. Rev. L.* **44**, 1069.

Clark A. C. 1964, *Phys. Fluids* **7**, 1299.

Cowling T. G. 1957, *Magnetohydrodynamics*, Interscience Publishers Inc.

Craig I. J. D. and Fabling R. B. 1996, *Ap. J.* **462**, 969.

Craig I. J. D., Fabling R. B., Henton S. M. and Rickard G. J. 1995, *Ap. J. L.* **455**, L197.

Craig I. J. D. and Henton S. M. 1994, *Ap. J.* **434**, 192.

Craig I. J. D. and Henton S. M. 1995, *Ap. J.* **450**, 280.

Craig I. J. D. and Henton S. M. and Rickard G. J. 1993, *Astron. Astro.* **267**, L39.

Craig I. J. D. and McClymont A. N. 1991, *Ap. J. L.* **371**, L41.

Craig I. J. D. and McClymont A. N. 1993, *Ap. J.* **405**, 207.

Craig I. J. D. and Rickard G. J. 1994, *Astron. Astro.* **287**, 261.

Craig I. J. D. and Watson P. G. 1992, *Ap. J.* **393**, 385.

Culhane J. L. and Jordan C. 1991, *The Physics of Solar Flares*, Cambridge University Press.

DeLuca E. E. and Craig I. J. D. 1992, *Ap. J.* **390**, 679.

Dungey O. 1953, *Phil. Mag.* **44**, 725.

Forbes T. G. and Priest E. R. 1987, *Rev. Geophys.* **35**, 1583.

Hassam, A. B. 1992, *Ap. J.*, **399**, 156.

Henton S.M. 1993, *Saturation of Fast Dynamic Magnetic Reconnection*, M.Sc. Thesis, University of Waikato.

Gratton F. T. and Gnavi G. 1990, *J. Geophys. Res.* **95**, 261.

Gratton F. T., Heyn M. F., Biernat H. K., Rijnbeek R. P. and Gnavi G. 1988, *J. Geophys. Res. 93*, 7318.

Jardine M., Allen H. R., Grundy R. E. and Priest E. R. 1992, *J. Geophys. Res.* **97**, 4199.

Lau Y. T. and Finn J. M. 1990, *Ap. J.* **350**, 672.

Parker E. N. 1957, *J. Geophys. Res.* **79**, 1558.

Parker E. N. 1963, *Ap. J. S.* **77**, 8.

Parker E. N. 1979, *Cosmical Magnetic Fields*, Oxford University Press.

Petschek H. E. 1964, *AAS-NASA Symposium on the Physics of Solar Flares, NASA Spec. Publ. SP-50*, edited by W. N. Hess, 425.

Phan T. D. and Sonnerup B. U. O. 1990, *J. Plasma Phy.* **44**, 525.

Priest E. R. 1981, *Solar Flare Magnetohydrodynamics*, Gordon and Breach.

Priest E. R. and Forbes T. G. 1986, *J. Geophys. Res.* **91**, 5579.

Priest E. R. and Titov V. S. 1995, *Phil. Trans. Roy. Soc. London.*, in press.

Rickard G. J. and Craig I. J. D. 1993, *Phys. Fluids B.* **5**, 596.

Smith G. D. 1978, *Numerical Solutions of Partial Differential Equations : Finite Difference Methods*, Second Edition, Oxford University Press.

Sonnerup B. U. O. 1970, *J. Plasma Phys.* **14**, 283.

Sonnerup B. U. O. and Phan T. D. 1990, *J. Geophy. Res. 95*, 259.

Sonnerup B. U. O. and Priest E. R. 1975, *J. Plasma Phys.* **14**, 283.

Spanier J. and Oldham K. B. 1987, *An Atlas of Functions*, New York : Hemisphere.

Spitzer L. W. 1962, *The Physics of Fully Ionised Gases*, Interscience Publishers.

Strauss H. R. 1990, *J. Geophys. Res.* **95**, 17145.

Sturrock P. A. 1980, *Proc. of the Skylab Workshop on Solar Flares*, Colo. Ass. Univ. Press.

Svesta Z. 1976, *Solar Flares*, Reidel Publishing Company.

Sweet P. A. 1958, *IAU Symposium 6, Electromagnetic Phenomena in Cosmic Physics*, edited by B. Lehnert, Cambridge University Press, 123.

Vasyliunas V. M. 1975, *Rev. Geophys. Space Phys.* **13**, 303.

Watson P. G. and Craig I. J. D. 1996, submitted to *Phys. Plas.*

Yeh T. and Axford W. I. 1970, *J. Plasma Phys.* **4**, 207.

Zirin H. 1966, *The Solar Atmosphere*, Blaisdell Publishing Company.

Magnetic Reconnection in Astrophysical Plasmas
Erratum

(i) The following corrections should be added (p.=page number , l.=line number).

p.5 Equation (2.3) : delete `c'.
p.5 l.+19 : delete `c'.
p.5 l.+20 : `$\eta=c/(\mu\sigma)$' should read `$\eta=1/(\mu\sigma)$'.
p.8 l.+12 : `incompressible' should read `compressible'.
p.16 l.+7 : `capability' should read `capabilities'.
p.19 l.-8 : delete `a'.
p.21 : partial derivatives of P_1 and P_2 in (3.5), (3.7), (3.8) and (3.9) should be ordinary derivatives.
p.22 l.-6 : `been' should read `be'.
p.22 l.-5 : delete `be'.
p.23 l.+15 : insert `a' in `is wave equation'.
p.24 l.+9 : delete repeated `the'.
p.40 l.-4 : replace `typical' with `coronal'.
p.41 l.-7 : insert `for small values of η' before 'which is the same value quoted by DC'.
p.56 Figure 4.10a : delete 'Positive values imply that the force is directed to the right' from caption.
p.56 Figure 4.10b : delete 'Positive values imply that the force is directed to the right' from caption.
p.59 l.+10 : replace `$(\psi_y,-\psi_x)$' with `$(\psi_y,-\psi_x,0)$'.
p.59 l.+14 : replace `$(\varphi_y,-\varphi_x)$' with `$(\varphi_y,-\varphi_x,0)$'.
p.64 l.-7 : `(a) $\varphi_1$ and (b) $\psi_0+\psi_1$' should read `(a) $\psi_0+\psi_1$ and (b) φ_1'.
p.75 l.+2 : `momentmum' should read `momentum'.
p.78 l.+3 : delete 'Each solution for φ can be approximated by (6.5) in the vicinity of the neutral line'.
p.78 l.+9 : `$\mu z$' should read `z'.
p.78 l.+10 : `$-1/(2\mu z)$' should read `$-1/(2z)$'.
p.100 Figure 7.1 : insert `Selected plots illustrate the localisation of the g_x profile' into caption.
p.114 Figure 7.8 : the a-axis should have negative values.
p.115 l.-3 : replace `along' with `near'.
p.119 Figure 7.12a : the a-axis should have negative values.
p.119 Figure 7.12b : the ν-axis should have negative values.
p.121 l.+12 : `unreasonable' should read `reasonable'.

(ii) The bracket notation introduced in Chapter 5, namely $[f,g]=f_xg_y-f_yg_x$, is known as the Poisson bracket. These brackets are widely used in classical mechanics (e.g. Goldstein 1980).

(iii) The sign of the electric field is incorrect in Section 3.2.3, from (5.7) onward in Chapter 5, and throughout Chapter 6 - in each instance $E/E_0/E_1/E_2$ should be replaced by $-E/-E_0/-E_1/-E_2$. This error does not effect the analysis as the electric field is a arbitrary parameter.

(iv) Let us consider the special case $\alpha=0$ for the time-dependent analysis of Chapter 7. This parameter choice corresponds to strictly antiparallel flows about the neutral line at x=0 and is dealt with by Bulanov et. al. (1990). With $\alpha=0$ our governing equations become

$$f_t - \beta x g_x = -2\beta g,$$
$$g_t - \beta x f_x = \eta g_{xx},$$

which can be combined to give

$g_{tt} + \beta^2 x g_x - \beta^2 x^2 g_{xx} = \eta g_{xxt}$,

To solve this equation we follow Bulanov et. al. (1990) and differentiate with respect to x to yield

$b_{tt} + \beta^2 b - \beta^2 x b_x - \beta^2 x^2 b_{xx} = \eta b_{xxt}$,

where

$b = -g_x$.

We now take the Fourier transform of this equation which gives

$(\eta s + \beta^2 x^2) B_{xx} + \beta^2 x B_x - (s^2 + \beta^2) B = 0$,

where

$B(x,s) = \int e^{-st} b(x,t)\, dt$.

The solution of our transformed equation can be written as

$B(x,s) = C_1(s)[(\eta s + \beta^2 x^2)^{1/2} + \beta^2 x]^{+\lambda} + C_2(s)[(\eta s + \beta^2 x^2)^{1/2} - \beta^2 x]^{-\lambda}$, $\qquad \lambda=(s^2 + \beta^2)^{1/2}$.

Thus our solution will be the inverse Fourier transform

$b(x,t) = \int e^{+st} B(x,s)\, ds$.

From this analysis it can be shown that

$l \sim \eta^{1/2}$,
$J_0 \sim \eta^{-1/2}$,

and so

$\partial\psi/\partial t = \eta J_0 \sim \eta^{1/2}$,
$W_\eta \approx \eta\, J_0^2 L l \sim \eta^{1/2}$,

which both indicate slow rates of energy release for coronal values of plasma resistivity.

(v) The following two paragraphs should be inserted into Chapter 8 at the end of Section 8.2:

We now discuss the implications of our exact solutions of magnetic reconnection to solar flares. Both the steady-state (Chapter 6) and time-dependent (Chapter 7) solutions have the Ohmic dissipation rate scaling as $W_\eta \sim \eta^{-1/2}$ and the flux annihilation rate scaling as $\partial\psi/\partial t \sim \eta^0$ where η is the plasma resistivity. Coronal values of $\eta = O(10^{-12})$ imply that energy stored in the magnetic field is primarily transferred into localised heating of the plasma. Therefore our reconnection solutions suggest that plasma heating will be more apparant outcome of a solar flare than the kinetic energy of plamsa motions.

A necessary requirement for achieving `fast' energy release from our exact solutions is a large background pressure. This external pressure drives a background plasma flow which maintains the pile-up of the magnetic field at the onset of the current sheet. Without this pile-up phenomenon the

reconnection rates have been shown to stall dramatically - see Chapter 4. This result suggests that the photosphere, the atmospheric layer below the corona, should now need to be considered. Here the magnetc field ($O(10^4)$ Gauss) is much greater than the magnetic field in the corona. Hence the external region of our reconnection solutions could be thought of as being coupled to the photosphere which is one way to account for the exceedingly large pressures.

(vi) The following lines should be inserted into the References:

Goldstein H. 1980, Classical Mechanics - reprint, Adison Wesley.
Bulanov S. V. and Shasharina S. G. 1990, Plas. Phy. Contolled Fusion, **32**, 377-389.